Development of Novel Optical Fiber Interferometric Sensors with High Sensitivity for Acoustic Emission Detection

Jiangdong Deng

Dissertation submitted to the Faculty of
Virginia Polytechnic Institute and State University
in partial fulfillment of the requirements for the degree of

Doctor of Philosophy
in
Electrical Engineering

Dr. Anbo Wang, Chair
Dr. Ira Jacobs
Dr. Yilu Liu
Dr. Guy Indebetouw
Dr. Ioannis M. Besieris

October 12, 2004

Blacksburg, Virginia

Keywords: Optical fiber sensors, acoustic emission, optical interferometer, partial discharges, power transformer

Development of Novel Optical Fiber Interferometric Sensors with High Sensitivity for Acoustic Emission Detection

Jiangdong Deng

Committee: Dr. Anbo Wang (Chair), Dr. Ira Jacobs,
Dr. Yilu Liu, Dr. Guy Indebetouw and Dr. Ioannis M. Besieris

Abstract

For the purpose of developing a new highly-sensitive and reliable fiber optical acoustic sensor capable of real-time on-line detection of acoustic emissions in power transformers, this dissertation presents the comprehensive research work on the theory, modeling, design, instrumentation, noise analysis, and performance evaluation of a diaphragm-based optical fiber acoustic (DOFIA) sensor system.

The optical interference theory and the diaphragm dynamic vibration analysis form the two foundation stones of the diaphragm-based optical fiber interferomtric acoustic (DOFIA) sensor. Combining these two principles, the pressure sensitivity and frequency response of the acoustic sensor system is analyzed quantitatively, which provides guidance for the practical design for the DOFIA sensor probe and system.

To meet all the technical requirements for partial discharge detection, semiconductor process technologies are applied, for the first time to our knowledge, in fabricating the micro-caved diaphragm (MCD) used for the DOFIA sensor probe. The novel controlled thermal bonding method was proposed, designed, and developed to fabricate high performance DOFIA sensor probes with excellent mechanical strength and temperature stability. In addition, the signal processing unit is designed and implemented with high gain, wide band response, and ultra low noise.

A systematic noise analysis is also presented to provide a better understanding of the performance limitations of the DOFIA sensor system. Based on the system noise analysis results, optimization measures are proposed to improve the system performance.

Extensive experiments, including the field testing in a power transformer, have also been conducted to systematically evaluate the performance of the instrumentation systems and the sensor probes. These results clearly demonstrated the feasibility of the developed DOFIA sensor for the detection of partial discharges inside electrical power transformers, with unique advantages of non-electrically conducting, high sensitivity, high frequency response, and immunity to the electro-magnetic interference (EMI).

Acknowledgements

First and foremost I would like to express my sincere gratitude to my advisor and friend, Dr. Anbo Wang, for his faith, patience, generous supports, and encouragement throughout my study and research. His technical and editorial advice was essential to the completion of this dissertation and has taught me innumerable lessons and insights on the working of academic research. With his confidence, determination, dedication, and incredible achievements, he will continue to serve as my mentor who sheds light on my journey ahead.

I would also like to thank Dr. Ira Jacobs, Dr. Yilu Liu, Dr. Guy Indebetouw and Dr. Ioannis M. Besieris for serving on my committee and for the encouragement and valuable suggestions that I received from them.

Words are too limited to express my appreciation to Dr. Hai Xiao, my brother and colleague, for his contributions to this research work, and for his support and encouragement in the past years. Many of the ideas in my work originated in discussions with him. I have been fortunate to have such a brother and friend in my life.

Acknowledgement and thanks must be extended to all my colleagues and friends at Center for Photonics Technology (CPT). Among them, I would like to thank Dr. Russell May, Dr. Gary Pickrell, Dr. Ming Luo, Dr. Bing Qi, Bing Yu, Zhengyu Huang, Wei Huo, as well as other CPTers, for their valuable suggestions and support. I am also grateful to Debbie Collins, who with her patience and thoughtfulness has made CPT a family with pleasure.

Last but not least, I am deeply grateful to my loving wife, Meng, for her understanding and support. Her love and encouragement was in the end what made this dissertation possible. My parents, receive my deepest gratitude and love for their patience and support during the years of my studies and work. The success of finishing this dissertation is my first present to my daughter, Claire, who brings the sunshine in my life.

Table of Contents

Abstract ..... **II**
Acknowledgements ..... **IV**
Table of Content ..... **V**
List of Figures ..... **VIII**
List of Tables ..... **XIII**
Index ..... **XIV**

Chapter 1. Introduction **1**
1.1 Background of Proposed Research 1
1.2 Acoustic Wave and Acoustic Sensors 2
1.3 Introduction to Fiber Optic Acoustic Sensors (FOAS) 5
1.3.1 Intensity-based FOAS sensor 5
1.3.2 Spectrally modulated FOSA sensor 6
1.3.3 Interferometric acoustic sensor 6
1.4 Progress of PD Detection 8
1.4.1 Introduction of partial discharges in power transformers 8
1.4.2 Commonly used approaches for PD detection 9
1.4.3 State of the art of acoustic PD detection for power transformers 10
1.5 Using FOAS for PD Detection 11
1.6 Scope of Proposed Research 14

Chapter 2. Theory of Diaphragm-Based Optical Fiber Acoustic Sensors **15**
2.1 Sensor Configuration 15
2.2 Optical Interference Theory in DOFIA 16
2.2.1 Interference intensity in a Fabry-Perot interferometer 16
2.2.2 Interference fringe versus surface reflectance 19
2.2.3 Interference fringe versus cavity length and source band-width 21
2.2.4 Sensitivity of interferometer 23
2.3 Diaphragm Dynamic Vibration Theory 26
2.3.1 Diaphragm deflection 27
2.3.2 Natural frequency of circular plates clamped at boundary 29
2.4 Sensor Responsivity and Sensitivity 37

Chapter 3. Fabrication of DOFIA Sensor Probe 40
3.1 Sensor Probe Practical Design Requirements.....40
3.1.1 Special design requirements of DOFIA probes for PDs application 40
3.1.2 Sensor Structure and Fabrication Requirements.....42
3.2 Sensor Fabrication System Configuration and Assembly Processing Steps 42
3.3 Sensor Material and Components 45
3.4 Development of Sensor Bonding Methods 50
3.4.1 Epoxy bonding method.....50
3.4.2 Inter-medium layer thermal bonding method.....52
3.4.3 Direct thermal bonding using CO_2 laser technology 55
3.4.3.1 CO_2 Laser sensor bonding system configuration.....55
3.4.3.2 Sensor bonding procedure.....56
3.4.4 Comparison of different bonding methods.....60
3.5 White-light Interferometric Sensor Cavity Length Monitoring Sub-system 61

Chapter 4. Instrumentation of DOFIA Sensor System 65
4.1 DOFIA Sensor System Configuration 65
4.2 Opto-electronic Circuits Design 67
4.2.1 Photo-detector and I-V Converter.....69
4.2.2 Gain-tunable amplifier 70
4.2.3 Band-pass filter 71
4.3 Preliminary Test of Signal Processing Unit.....72

Chapter 5. System Noise Analysis and Performance Improvement 75
5.1 Electronic Noise in DOFIA Sensor System.....75
5.1.1 Electronic noise assumption.....75
5.1.2 Power budget and electronic noise estimation of the sensor system 79
5.2 Optical Noise in Diaphragm-Based Acoustic Sensor System.....80
5.2.1 Noise analysis for light source.....80
5.2.1.1 Relative intensity noise (RIN).....81
5.2.1.2 Requirement of RIN for the sensor system.....82
5.2.1.3 Phase and frequency noise of laser source in the interferometric system.....82
5.2.2 Impact of optical feedback to the sensor performance 86

Chapter 6. Temperature Cross-Sensitivity in DOFIA Sensor 95
6.1 Mechanisms of Temperature Cross-sensitivity 95
6.2 Experiment Results and Discussion 97
6.3 Improvement of Sensor's T-cross Sensitivity 98

Chapter 7. DOFIA Sensor System Performance Evaluation and Calibration..... 101
7.1 Hydrostatic Pressure Test 101
7.2 Sensor Capability for Aerodynamic Pressure 103
7.3 Hydrodynamic Pressure Calibration and Test 106
7.3.1 Sensor calibration system for hydrodynamic pressure 106
7.3.2 System pressure resolution (P_{res}) 108
7.3.3 System frequency response test and acoustic wave detection 110
7.4 Sensor Capability for Propagation Characteristics of Acoustic waver 113
7.4.1 Basic concepts of acoustics 113
7.4.2 Acoustic wave attenuation test 115
7.4.3 Sensor directional sensitivity test 116
7.4.4 Location experiment for acoustic source 117

Chapter 8. Sensor Application for Partial Discharge Detection..... 119
8.1 Laboratory Setup for the Simulation of PD Acoustic Aaves 119
8.2 Field Test Results and Discussion.....122

Chapter 9. Summary and Conclusions 126

Reference 131
VITA..... 137

List of Figures

Figure 2.1 Illustration of the principle of the optical fiber acoustic sensor 15
Figure 2.2 Typical LED spectrum (λ_0=1310nm) 17
Figure 2.3 Interference fringe intensity for different reflectances (curve 1, R_1=R_2=0.04; curve 2, R_1=0.04 and R_2=0.4, curve 3, R_1=R_2=0.2, curve 4, R_1=R_2=0.4) 19
Figure 2.4 Fringe visibility for different reflectance (λ_{FWHM}=50nm, curve 1, *R_1=R_2=0.04*; curve 2, *R_1=0.04 and R_2=0.4,* curve 3, *R_1=R_2=0.2,* curve 4, *R_1=R_2=0.4*) 20
Figure 2.5 Sensor visibility as function of surface reflectance (L=20um, λ_{FWHM}=50nm) 20
Figure 2.6 Interference fringe via cavity length (λ_{FWHM}=50nm, curve 1, *R_1=R_2=0.04*; curve 2, *R_1=0.04 and R_2=0.4,* curve 3, *R_1=R_2=0.2,* curve 4, *R_1=R_2=0.4*) 22
Figure 2.7 Interference fringe via cavity length (λ_{FWHM}=20nm, curve 1, *R_1=R_2=0.04*; curve 2, *R_1=0.04 and R_2=0.4,* curve 3, *R_1=R_2=0.2,* curve 4, *R_1=R_2=0.4*) 22
Figure 2.8 Illustration of a linear operating range of the sensor response curve 23
Figure 2.9 (a), Interference fringes for different reflectance, and (b) corresponding sensitivity curves for each fringe 24
Figure 2.10 Structure model for diaphragm-based acoustic sensor 26
Figure 2.11 Predicted diaphragm sensitivity (μm/psi) versus diaphragm thickness at *a=1* mm .. 28
Figure 2.12. Maximum tolerable pressure and linear response pressure of sensors 29
Figure 2.13 Predicted frequency response of the sensor at *r=1* mm 32
Figure 2.14 Sensor frequency response with single-mode resonation 34
Figure 2.15 Normalized frequency response of diaphragm based sensor (Theoretical) 36
Figure 2.16 Experimental result of Sensor frequency response (*h= 100um, a=1200um, I_0~2mW, f_{00}=110kHz)* 36
Figure 2.17 Acoustic pressure signal processing 37
Figure 3.1 Basic structure of diaphragm-based FP acoustic sensor 43
Figure 3.2 Schematic of diaphragm-based fiber optic fiber sensor fabrication system 43
Figure 3.3 Sensor head fabrication process diagragm 44
Figure 3.4 Micro-caved diaphragm 45
Figure 3.5 Schematic of the fabrication procedure of MCDs 46
Figure 3.6 A photo-mask with 1.5mm hole array 47
Figure 3.7 Reflectance of Au film versus Au thickness 48
Figure 3.8 (a) SEM picture of MCD and (b) photograph of diced MCD chips 49

Figure 3.9 Supporting system for epoxy bonding and solder bonding 51
Figure 3.10 From the left: Epoxied sensor, silica hollow core, another sensor, a single ferrule, and diaphragm chip 51
Figure 3.11 Schematic support system for Inter-medium layer bonding method 52
Figure.3.12 Modified inter-medium layer thermal bonding system 53
Figure 3.13 Controlled thermal bonding method to fabricate PD sensors 53
Figure 3.14 Heating process of thermal bonding 54
Figure 3.15 Photograph of three diaphragm-based sensor probes fabricated by inter-medium layer thermal bonding method 55
Figure 3.16 System setup diagram for CO_2 thermal Bonding 56
Figure 3.17 Sensor fabrication procedure using CO2 laser direct bonding approach 57
Figure 3.18 Laser beam path surrounding the fiber-ferrule assembly 58
Figure 3.19 Photograph of stage system for direct laser bonding methods (a) stage and mirror system for fiber-ferrule bonding, (b) stage for ferrule-MCD bonding 58
Figure 3.20 Laser heating curve for MCD sensor bonding 59
Figure 3.21 Sensor fabricated by CO_2 laser bonding method 59
Figure 3.22 (a) Light source with band-width 50nm, (b) Sensor spectrum (L=20um, and R=20%), (c) Normalized sensor spectrum 61
Figure 3.23 Photography of white-light cavity length monitoring system 62
Figure 3.24 Typical interference spectrum of medium fineness sensor 63
Figure 4.1 Schematics of the diaphragm-based OFAS sensor system 65
Figure 4. 2 Spontaneous emission spectrum of the SLED1300D20A 66
Figure 4.3 Prototype of the signal processing unit for diaphragm-based fiber sensor system 67
Figure 4.4. Schematic of one-channel signal processing circuits 68
Figure 4.5 Roll-off phenomenon in current amplifiers without amplitude equalizer 69
Figure 4.6 (a) Light detection and I/V converter. (b) Frequency response of T-feedback amplifier 70
Figure 4.7 Gain tunable main amplifier 70
Figure 4.8 Second-order low-pass Butterworth filter. (a) Circuit. (b) Frequency response 71
Figure 4.9 Second-order high-pass Butterworth filter. (a) Circuit. (b) Frequency response 72
Figure 4.10 Frequency response of the signal processing system 72
Figure 4.11 Noise performance of the electric circuit (Noise level~15mV) 73
Figure 4.12 Noise performance of the whole system (Noise level <30mV) 73

Figure 5.1. Noise equivalent circuit of the transimpedance amplifier 76
Figure 5.2 Schematic representation of an diaphragm interferometer 83
Figure 5.3 Normalized spectral noise density. The actual spectral noise density distributes in the region I 85
Figure 5.4. Schematic arrangement of a laser diode cavity with external optical feedback 86
Figure 5.5 The round-trip phase change $\Delta\phi_L$ versus optical frequency ν with and w/o feedback 88
Figure 5.6 Laser diode with a fiber pigtail with a sensor head at its fiber end 89
Figure 5.7 C curves as function of R_{2ext} for a laser diode 90
Figure 5.8 Noise performance in the DFB-sensor system (a) with isolation H=45dB, noise~40mv, and (b) without isolator, noise level >200mv 91
Figure 5.9 (a) 1310nm SLED source without reflectivity end-face at the fiber end, noise ~25mv; (b)1310nm SLED source with reflectivity end-face at the fiber end, noise ~30mv ... 92
Figure 5.10. (a) 1310nm DFB laser without reflectivity end-face at the fiber end, noise ~40mv; (b) 1310nm DFB laser with reflectivity end-face (4%) at the fiber end, noise ~75mv 94
Figure 6.1 Thermal expansion model of sensor head 95
Figure 6.2. Temperature dependence of various sensors. (a) thermally bonded sensor (b) Epoxy bonded sensor (green line) and thermally bonded sensor 97
Figure 6.3 Structure of the open-air sensor head 98
Figure 6.4 Temperature effect of the open-air sensor (β ~$1.6x10^{-3}$(μm/°C)) 99
Figure 6.5 Experiment set-up for external dynamic compensating the temperature coefficient .. 99
Figure 6.6 Sensor response results under external dynamic compensation 100
Figure 7.1 Experiment set-up for hydrostatic pressure test (Sensor probe, a=1.25mm, h=100μm) 102
Figure 7.2 Sensitivity test by applying a known hydrostatic pressure 102
Figure 7.3 Experiment set-up for DOFIA sensor responses to the scanning air blows 103
Figure 7.4 Comparison of the Kulite sensor and fiber optic acoustic sensor responses to the scanning air blows 104
Figure 7.5 Experiment set-up for the shock wave testing using DOFIA sensor 105
Figure 7.6 Comparison of the Kulite sensor and fiber optic acoustic sensor responses to a passing air shock wave 105
Figure 7.7 Frequency of shock-wave 106
Figure 7.8 Schematics of Sensor calibration system 107

Figure 7.9 Photograph of the sensor calibration system 107
Figure 7.10 Frequency responsivity of the calibrating sensor (WDU-PAS Inc.) 108
Figure 7.11 Sensor response and FFT spectrum, (curve 1, DOFIA sensor with $R=R_0=0.04$, and curve 2, WDU calibrating sensor 109
Figure 7.12 Sensor response and FFT spectrum. (Ch.1 and A, DOFIA sensor with R=0.2, and Ch.2 and B, WDU calibrating sensor) 109
Figure 7.13 Response comparison between DOFIA (a) and WDU (b) sensors to an acoustic emission 111
Figure 7.14 DOFIA sensor's frequency response (r:1200um, h:100um, I_0 ~2mW, f_{00}=91 kHz in water) 112
Figure 7.15 Frequency response of a broad-band sensor (r:1200um, h:254um, I_0 ~2mW, f_{00}=91 kHz in water) 112
Figure 7.16 Signal attenuated with increasing distance to the acoustic source (*f=230kHz)* 115
Figure 7.17 Direction sensitivity of DBI sensor (*f=230kHz*) 116
Figure 7.18 Acoustic source location experiment using optical fiber sensors 117
Figure 7.19 Sensors response to the same source in the water tank 118
Figure 8.1 Partial discharges device set-up 119
Figure 8.2 Photograph of the PDs simulation systems 120
Figure 8.3 (a) Partial discharge detected by fiber sensor. Conditions: Optical power is 1.5mW, sensor is 0.5cm from the spark plug. (b) Measured with PZT sensor. The PZT sensor is 2cm from the PD source box 120
Figure 8.4 Fiber sensor and PZT are far away from the enclosed PDs source (a) Partial discharge detected by fiber sensor. Conditions: the same as those in Figure1, except that the light source is turned off. (b) Measured with PZT sensor. The power supply to preamplifier is off and the PZT sensor is about 30cm from the PD source box 121
Figure 8.5 Partial discharge test setup at J.W. Harley Inc. at Twinsburg, Ohio, U.S.A. 122
Figure 8.6 Test setup for the field-testing performed at J.W. Harley Inc. at Twinsburg, Ohio. a) Partial discharge simulator, b). Prototype fiber optic sensor system, c) Fiber optic acoustic sensor probe immersed within transformer oil close to the needle-plate discharge generator 123
Figure 8.7 Typical partial discharge acoustic signals detected by the fiber optic sensor and the Physical acoustic sensor. (a), Physical acoustic sensor output; (b), Fiber optic sensor output at 10cm away from the partial discharge source 124

Figure 8.8 Fiber optic sensor output at 50cm away from the partial discharge source. 124
Figure 8.9 Amplitude dependence on the distance between sensor location and the PD source. 125

List of Tables

Table 1.1 Acoustic wave spectrum 14
Table 2.1 Reflection-sensitivity increase factor Λ 25
Table 2.2 Properties of fused silica (@25 ^{o}C) 27
Table 2.3 Value of $(\lambda a)_{mn}$ 31
Table 3.1 Basic components and materials for diaphragm-based acoustic sensor 50
Table 3.2 Comparison of different sensor bonding methods 64
Table 5-1. Optical loss mechanisms in single-mode DOFIA system 79

Index

APM	Acoustic Plate Mode
AW	Acoustic Wave
CPT	Center for Photonics Technology
CTE	Coefficient of Temperature Expansion
DFB	Distributed Feedback Laser
DOFIA	Diaphragm-based Optical Fiber Acoustic
EFPI	Extrinsic Fabry-Perot Interferometer
EHV	Extreme High-Voltage
EMI	Electro-Magnetic Interference
EPRI	Electrical Power Research Institute
FOAS	Fiber Optic Acoustic Sensors
FP	Fabry-Perot
FPW	Flexural Plate Wave
FSO	Full Scale Output
IFPI	Intrinsic Fabry-Perot Interferometer
MCD	Micro-Caved Diaphragm
MEMS	Micro Electro Mechanical System
MZ	Mach-Zehnder
NSF	National Science Fundation
OPD	Optical Path Difference
OSA	Optical Spectrum Analysis
PDs	Partial Discharges
PZT	Piezo-electric
QCM	Quartz Crystal Microbalance
RIE	Reactive Ion Etching
RIN	Relative Intensity Noise
SAW	Surface Acoustic Wave
SEM	Scanning Electrical Microscopy
SLED	Superluminescent LED

SNR	Singnal-to-Noise Ratio
SOG	Spin-on Glass
TSM	thickness-shear mode
VLSI	Very Large Scale Intergration

Chapter 1. Introduction

1.1 Background of Proposed Research

Accurate acoustic wave (AW) technology is increasingly important to both modern science and engineering applications. For example, in navigation [1], sonar systems have been used for depth sounding, sea bottom profiling, and speed monitoring. In materials characterization [2], ultrasonic techniques have been applied to non-destructively measure the mechanical properties of a material, and to detect a variety of material defects such as cracks, inner stresses, micro displacements and inclusions. In medical applications [3], ultrasonic broadband pulse-echo techniques are widely used in imaging and diagnosis of inside organs of a human body. In this research, the initial motivation is to develop a fiber optic acoustic pressure sensor system and related techniques for accurately detecting hydro acoustic waves in harsh environments where extreme physical and chemical conditions are involved, such as high-temperature, high-pressure, strong electromagnetic field, high-energy radiation, and chemical corrosion.

More specifically, this research is to meet the recently increasing needs for detecting in real-time partial discharges in power transformers. Electrical power transformers are usually the most critical and costly component in power transmission and distribution systems. However, the failure rate of extreme high-voltage (EHV) power transformers is as high as 3% per year per device [4], which results in the loss of tens of millions dollars for each failed unit due to serious oil spills, fires causes extensive damage to adjacent equipment, and major disruption of service. Partial discharges (PDs) are reported to be involved in any transformer insulation failure. These discharges can degrade electrical insulation and eventually lead to failure of the transformer. Therefore, it is important to monitor the partial discharge activity in a transformer in order to detect incipient insulation problems, and to prevent further catastrophic failure.

One of the methods of monitoring PDs is to detect the acoustic waves generated by PDs. An obvious advantage of the acoustic method is that it can locate the site of a PDs by

studying the phase delay or the amplitude attenuation of the acoustic waves. Piezoelectric acoustic sensors are typically used for realizing PDs while being mounted externally on the walls of the power transformer. The external method offers the advantage of easy installation and replacement. However, the piezoelectric sensors often suffer from corruption of the signal from environmental noises such as electro-magnetic interference (EMI). Another problem associated with the externally mounted piezoelectric sensors is that the multi-path of the acoustic wave transmission makes it difficult to locate the exact site of the partial discharges. It is thus desirable to have such sensors that can be reliably operated inside a transformer, even within the transformer windings, with high enough pressure sensitivity (~0.001psi) and frequency response (up to 300kHz) to pick up clean PD-induced acoustic signals. The sensor should also be able to 'realize' the direction of the acoustic wave for recovering location of the PDs source. Moreover, these sensors need to be chemically inert, electrically non-conducting, and small in size.

Having a number of inherent advantages, including small size, light weight, high sensitivity, high frequency response, and immunity to electromagnetic interference, optical fiber-based sensors have been proven to be attractive to measure a wide range of physical and chemical parameters. Sponsored by the National Science Foundation (NSF) and Electrical Power Research Institute (EPRI), the Center for Photonics Technology (CPT) at the Bradley Department of Electrical and Computer Engineering is currently leading the effort in developing novel fiber-based sensor techniques that can provide the desirable sensitivity and frequency response for real-time on-line detection of acoustic emissions in power transformers [5-7].

1.2 Acoustic Wave and Acoustic Sensors

As a mechanical effect, an acoustic wave may be described as the passage of pressure fluctuations through an elastic medium as the result of a vibrational impetus imparted to that medium. The propagation of acoustic waves in different media is sensitive to the characteristics of the material. Therefore, acoustic methods have turned out to be informative tools for studying the structure of materials and the different physical

processes occurring in them. Actually, the characteristics of acoustic radiation have led to extensive applications in diverse areas: including sonar detection, defects detection in various materials and structures, medical diagnostics and therapeutic action on body organs, acceleration or stimulation of different technological processes, etc. Among all these applications, the acoustic sensor is the core instrument to obtain the initial information of the acoustic field in particular media.

Traditionally, there are various categories of acoustic sensors for different acoustic frequency ranges. In fact, the frequency spectrum of acoustic waves extends to more than fifteen orders of magnitude, from infrasonic, audible to ultrasonic wave, as indicated by Table 1.1. Table 1.1 also shows some typical sensors designed for purposes ranging from human heart imaging to cracks detection in airplane parts [8].

Besides audio-used microphones, the most commercially available acoustic sensor is piezoelectric crystal-based. Historically, the first piezoelectric acoustic sensor is a so-called thickness-shear mode (TSM) resonator, which is also widely referred to as quartz crystal microbalance (QCM) [9]. The TSM resonator typically consists of a thin disk of quartz with circular electrodes patterned on both sides. Due to the piezoelectric properties and crystalline orientation of the quartz, the application of a voltage between these electrodes results in a shear deformation of the crystal. The crystal can be electrically excited in a number of resonant thickness-shear modes. The presence of displacement maxima occurring at the crystal faces makes the thickness-shear modes of the sensor very sensitive to surface perturbation. That is, when the sensor surface is perturbed by the periodical pressure of acoustic waves, the resonant shear deformation will be changed, which results in the electrical output on electrodes. Employing similar principle of TSM, other acoustic devices are also introduced, such as the surface acoustic wave (SAW) device, the acoustic plate mode (APM) device, and the flexural plate wave (FPW) device. These devices are small in size, relatively inexpensive, quite sensitive, and inherently capable of measuring a wide variety of different input quantities.

1.3 Introduction to Fiber Optic Acoustic Sensors (FOAS)

Optical fiber has been involved in the sensing area for quite a long time. Optical fiber sensors have such advantages as: 1) immunity to electromagnetic interference (EMI); 2) avoidance of ground loops; 3) capability of responding to a wide range of measurands; 4) avoidance of electric sparks; 5) resistance to chemical corrosion, high temperature and other harsh environments; and 6) small size, lightweight, high sensitivity, large bandwidth, and capability of remote operation. These advantages make optical fiber sensors an excellent candidate for acoustic wave detection. Actually, optical fiber sensors have been successfully demonstrated in many acoustic related application areas, such as underwater acoustic sensing [10-12], material property analysis, and civil structure non-destructive diagnosis [13-14].

The light transmitted through an optical fiber can be characterized by such parameters as intensity, wavelength, phase, and polarization. By detecting the change of these parameters resulting from the interaction between the optical fiber and the measurand, fiber optic sensors can be designed to measure a wide variety of physical and chemical parameters. Accordingly, fiber optic acoustic sensors can be categorized into four major groups: intensity based sensors, spectrum based sensors, phase modulated (or interferometric) sensors, and polarization modulated devices. The extensive research in fiber optic sensor technologies in the past three decades has greatly enhanced the technical background of all the sensor categories.

1.3.1 Intensity-based FOAS sensor

In general, intensity-based fiber optic acoustic sensors (FOAS) are inherently simple and require only a modest signal processing complexity through a direct detection of the change of optical power either in transmission or in reflection. One of the most thoroughly analyzed intensity modulated FOAS is the reflective type sensor, which has a reflective end face at the fiber tip. The reflected light intensity is modulated by the pressure fluctuation through different interaction mechanisms. For example, the fiber

hydro-phone proposed by B. Jost [15] directly measures the temporal change of the pressure, inducing a change of the reflection coefficient, by detecting the reflected light intensity. G Zhou et al. [16] use a cantilevered fiber with reflection endface as the sensing element for measuring the pressure fluctuation. Another typical intensity based FOAS is based on the principle of total internal reflection [17]. However, intensity based FOAS has a series of limitations imposed by variable losses in the system that are not related to the measurand. Potential error sources include variable losses due to connectors and splices, microbending losses, and misalignment of light sources and detectors.

1.3.2 Spectrally modulated FOAS sensor

Spectrum based FOAS depends on a light beam being modulated in wavelength by acoustic pressure. The most popular FOAS is the fiber grating-based sensor [18,19]. Its signal detection mechanism is based primarily on the measurement of either the shift of the Bragg reflection wavelength or the change in transmitting optical power. It has been reported that fiber grating sensors can reach a resolution of 0.5% for hydrostatic pressure detection [20,21]. Recently, fiber grating sensors have been used to detect the acoustic wave [22], in which a 20kHz sound wave with pressure 130 dB re 1 uPa can be detected with resolution at about 2%. Fiber grating sensors have the advantages of immunity to the optical power loss variation of the sensor system and the capability of multiplexing many sensors to share the same signal processing unit. However, its sensitivity to pressure waves is inherently low. In addition, when used for pressure measurements, fiber grating sensors exhibit relatively large temperature dependence which limits their scale of applications for harsh environmental sensing.

1.3.3 Interferometric acoustic sensor

It has been of great interest to develop high performance interferometric fiber-optic sensors for the measurements of displacement, temperature, strain, pressure and acoustic signals. For acoustic pressure measurement, substantial efforts have been undertaken on Mach-Zehnder, Michelson interferometers, Sagnac, and Fabry-Perot interferometers.

Mach-Zehnder (MZ) and Michelson interferometers are the two intrinsic fiber sensors that have been investigated extensively for acoustic pressure detection in the early stage of fiber sensor development [23]. Hydrophones based on these two interferometers are reported to have high resolution of 0.1% [24, 25]. However, due to the low level of photoelastic or stress-optic coefficients of the silica glass fibers, a very long sensing fiber is necessary to obtain the desirable sensitivity, which unavoidably makes the sensor thermally unstable and sensitive to vibrations. In addition, due to source-induced phase noise in unbalanced interferometers, a highly coherent source with a relatively long coherence length is normally required [26]. Another drawback associated with these two types of interferometric sensors is the polarization-fading problem that refers to the interference fringe visibility as a function of the polarization status of the light transmitted inside the fibers. Since it is difficult to maintain the polarization status in practical applications, the long-term stability of these two types of interferometric sensor has been a concern.

Sagnac interferometer has been principally used to measure rotation as a replacement for ring laser gyros based on vacuum tube technology and mechanical gyros. For acoustic detection, due to balanced configuration in Sagnac interferometers, the phase noise problem met in MZ or Michelson interferometers can be eliminated [27]. In the frequency range of 0.4-1 MHz, the noise-equivalent pressure can be reduced down to 36-43 dB re. 1 uPa /$Hz^{1/2}$ [28]. However, this type of acoustic sensor has low frequency responsibility, unless a long fiber comprises the Sagnac loop. The problems of the temperature instability and the polarization fading also exist in Sagnac interferometer type acoustic sensors.

Fabry-Perot based fiber optic interferometric sensors are often categorized into two major types: (1) intrinsic Fabry-Perot interferometer (IFPI) sensor, in which the cavity is usually contained within the fiber without any air gaps; and (2) extrinsic Fabry-Perot interferometer (EFPI) sensor, in which the cavity is external to the fiber and includes an air gap. IFPI sensors embedded in solid materials have been widely used to measure

acoustic waves with relatively high pressure (peak pressure in the range 15,000- 30,000- Torr) [29-31]. EFPI fiber optic sensors are reported to be particularly well suited for weak acoustic wave measurement because of their extremely high sensitivity [32-34]. Compared with Mach-Zehnder and Michelson sensors, the EFPI sensor excels in its smaller size and the immunity to the polarization status. Moreover, because the reference and signal waves are packed closely together, one of potential advantages of EFPI sensors is them small temperature dependence.

In summary, optical fiber interferometric sensor usually has the reputation in flexibility in design, large dynamic range, and extremely high resolutions. However, due to the non-linear periodic nature of the interference signal, the accurate detection of the differential phase change of an interferometer has been a real challenge. In addition, interferometric sensors require complicated signal processing in order to achieve the potential high resolution of measurement. Such signal processing complexity greatly increases the cost and renders the interferometric sensors unacceptable for many applications.

Based on the survey above, it is realized that optical fiber-based acoustic sensors have the great potential to replace the majority of conventional electronic pressure transducers in today's sensor market, because of their unique set of advantages that cannot be offered by other technologies. However, several technical difficulties delay this becoming a reality. The most common concerns about the practical applications of fiber optic pressure sensors are their stability and cross-sensitivity among multiple environmental parameters. Fluctuation of source power and fiber loss can easily introduce errors to the measurement results, and make most optical fiber-based sensors unstable. The fact that most fiber sensors are cross sensitive to temperature changes also makes it difficult to use fiber optic sensors to measure parameters other than temperature in many practical applications.

1.4 Progress of PDs Detection

1.4.1 Introduction of partial discharges in power transformers

Power transformers are the most critical and costly component in transmission systems, especially those of large capacity such as generator step-up transformers and system tie auto-transformers. Catastrophic failures of power transformers can occur without any warning, resulting in serious oil spills, fires, extensive damage to adjacent equipment, and major disruption of service. If the transformer can not be repaired due to the extensive damage, the cost of failures can be several times bigger than the cost of new transformers, with the costs of reinstallation, transportation, other equipment damage and/or outages caused by the failure, lost sales revenue, etc., which can easily drive the total cost of a single transformer failure into tens of millions of dollars.

As mentioned in Section 1.1, EHV power transformers have unacceptable failure rates of more than 3% per year per device [4, 35]. An informal survey indicated that over 75% of large, EHV transformer failures are caused by dielectric problems. Involved in any transformer insulation failure, partial discharges can gradually degrade electrical insulation and eventually lead to failures and loss of the transformer. It is important to monitor the partial discharge activity of important transformers so that the incipient insulation failure can be recognized before creating any internal fault, and the transformer may be repaired or replaced in a controlled fashion.

Partial discharges in transformers include arcing, flashover, and sparking. In most cases, partial discharges in power transformers start well before the structure fails. An exception is the static electrification of normal AC and accumulated DC voltages, particularly during transformer startup. Partial discharges typically happen at regular time intervals ranging from seconds to hours apart. The more frequently they occur the more severe their activities are. Once there is partial discharge activity, failure can occur at any moment. Therefore, the monitoring of PDs is necessary and fast reaction to monitoring information is mandatory.

1.4.2 Commonly used methods for PDs detection

Generally there are three types of methods for PDs detection: the chemical methods, the detection of electrical pulses, and the detection of acoustic signals. By chemically analyzing the gas or oil samples from the transformer, the partial discharge activity and so as the quality of the transformer insulation medium can be assessed. Recent research indicates the trend of developing gas sensors and applying them as on-line gas monitors[4, 36]. Problems associated with chemical methods are the fact that there can be a long time delay between the initiation of a PDs source and the evolution of enough gas for it to be detectable. Besides, as gas and oil are taken from large reservoirs, there is also little information regarding the physical location of a source.

There is over thirty years of experience with partial discharge measurement in factories using electrical pulse detection techniques at the transformer terminals. However, the methods are difficult to apply in the field to in-service transformers because the noise from discharge on the lines and other equipment that makes it difficult to determine which signals are caused by problems in the transformer. A further limitation of these methods lies in the little possibility to indicate the location of the detected PDs source.

Acoustic PDs detection has been studied and developed over a long period, and a substantial body of knowledge has been accumulated. A PDs results in a localized, nearly instantaneous release of energy, appearing as a small ‘explosion’, which is a point source of acoustic waves. When the wave propagates to all directions, it can be detected and analyzed by a suitable sensor with data acquisition system. One of the most obvious advantages of acoustic PD detection is it is a real-time and on-line method.

1.4.3 State of the art of acoustic PDs detection for power transformers

A significant amount of work has been done in the detection and location of PDs by acoustic sensing for transformers. General Electric (GE) used acoustic detection for detecting discharges during factory tests in the early 1960’s**.** The acoustic signal

detection usually involves the use of piezoelectric probes followed by preamplifier, filters, power amplifiers and data acquisition units. Typically, the sensitive frequency of piezoelectric sensors is suggested to be in the range of 30 kHz to 300kHz [37]. This is basically because most of noises and signal drifting in transformers, such as the magnetostriction-introduced noise, usually exist in the low frequency range below 60kHz, and the acoustic emission frequency of a PD is mostly around 150kHz [38,39].

The acoustic sensors are usually mounted on the outside of the transformer tank wall by magnetic hold-downs with a thin layer of acoustic couplant to ensure good sensitivity. Since glass is a good conductor of acoustic signals, glass fiber rods are also placed directly down in to the oil to increase sensitivity. The piezoelectric sensor is attached to the end of the rod to pick up the signals.

Noise suppression is a major concern in developing an acoustic PD monitoring system. Principally, acoustic sensors are immune to EMI, but will still suffer if they are not properly shielded. In addition, there are two kinds of mechanical noises: continuous noise and transient noise. Continuous noise results from modal vibration of the transformer or from ambient environment, which dominates the low frequency regime. While transient noise results from rain, snow, blowing sand, etc., which usually has a broader frequency spectrum and can appear similar to signal from PDs [40].

Another major problem involved in the current piezoelectric sensor-based acoustic PD detection systems is that precisely locating the PD source is almost impossible, because of the effects of acoustic signal attenuation and spurious reflection due to the complex structure of the transformer. In addition, the existence of multiple partial discharges will result in the ‘pile-up’ effects, making the position estimation difficult.

1.5 Using OFS for PD Detection

As addressed above, optical fiber-based sensors have been shown to be attractive to measure a wide range of physical and chemical parameters because of the inherent

advantages. These advantages make optical fiber sensors an excellent candidate for transformer PD detection. Z. Zhao et al. [41] reported that a Mach-Zehnder fiber optic interferometer was used as an acoustic sensor in the PD detection and location. However, due to the low level of photoelastic or stress-optic coefficients with the silica glass fibers, a long coiled sensing fiber is necessary for the Mach-Zehnder method to obtain the desirable sensitivity, which makes the sensor bulky (in the order of ~ 1 inch). Large sensor size makes the sensor unattractive for the transformer on-line diagnostic monitoring.

For the partial discharge detection, a fiber optic acoustic sensor should basically provide ultra-high sensitivity response in a wide frequency range and stability among multiple environmental parameters. The transmission losses of acoustic waves produced by PDs may be large so that high sensitivity may be required. The frequency of acoustic emission usually ranges from 30kHz to 300 kHz. Besides, an ideal acoustic fiber sensor should be suitable in harsh environments, which may involve extreme physical conditions, such as elevated temperatures, chemical corrosion, toxicity, strong electromagnetic interference, and high voltage. These situations open up challenging opportunities for the research of fiber optic acoustic sensor technologies. To our knowledge, there are no existing fiber acoustic sensors that are suitable for the detection and location of partial discharges in the transformers due to either their geometrical size, limited detection sensitivity or strong frequency dependence.

The goal of this proposed research is to develop a new highly-sensitive, reliable fiber-based sensor technique for real-time on-line detection of acoustic emissions in power transformers. In general, fiber optic acoustic sensors that can be used for PDs detection in a high-voltage transformer have to satisfy several special requirements as explained below.

Ultra-high sensitivity

Due to the high acoustic attenuation coefficient of transformer oil, the acoustic signal generated by partial discharges is usually very weak at the sensors. Therefore, sensor's resolution for PDs detection should be at least 0.001 psi.

High and clean frequency response

The frequency range of the sensor needs to be 30~300kHz, which is basically due to the fact that the acoustic emission frequency of PDs is mostly around 150 kHz.

Wide directional response

For the purpose of locating partial discharges, the sensor should be able to respond to the acoustic wave at a wide range of incidence angles.

Small size

For acoustic wave detection, the size of sensors should be less than the sound wavelength, otherwise the directionality of the sensor is not isotropic. Small size provides better geometric flexibility.

Good thermal stability

Fiber acoustic sensors designed for measuring partial discharges must be thermally stable or with the capability of compensating for temperature changes. Otherwise the temperature fluctuations of environment may cause sensitivity change and easily introduce errors in the measurement.

Quantitative measurement

Fiber optic acoustic sensors with quantitative pressure and frequency readouts are much more attractive in real engineering applications.

Cost-effectiveness

As the market of fiber optic acoustic sensors is increasing rapidly, the cost of sensors and instrumentation becomes an issue. In order to successfully commercialize the new technology, fiber optic sensor systems must be robust as well as with low costs.

This requires that the complexity of fiber sensor system should be kept to the minimum, also the technique and process of fabricating sensor probes should have the potential of allowing mass production.

1.6 Scope of Proposed Research

The research work in this project, entitled “Development of Novel Optical Fiber Interferometric Sensors with High Sensitivity for Acoustic Emission Detection ”, is focused on the following:

1) Illustrate the theory of diaphragm-based fiber interferometer systematically, and build up the fundamentals of optical fiber acoustic sensors.
2) Design and develop techniques for sensors fabrications and system instrumentation.
3) Evaluate and optimize the sensor system performance.
4) Apply the developed sensor technologies to PDs detection.

In Chapter 2, the basic theories involved in the diaphragm-based optical fiber acoustic (DOFIA) sensor will be built up, including the principle of an optical interferometer and dynamic analysis for the diaphragm-based sensor structure. Chapter 3 will concentrate on the sensor fabrication technologies for diaphragm-based sensor probes. The work of implementing the diaphragm-based acoustic instrumentation sensor systems is reported in Chapter 4. The sensor system noise analysis and performance optimization are presented in Chapter 5. As one of the major concerns of sensor performance, the evaluation of sensor’s temperature-cross sensitivity is separately discussed in Chapter 6. Chapter 7 will be dedicated to performance evaluation and calibration of the entire sensor system, in terms of hydrostatic/dynamic pressure sensitivity, and frequency response. In Chapter 8, the experiment and results in PDs detection will be described. Chapter 9 will summarize the research results and conclusions.

Table 1.1 Acoustic wave spectrum

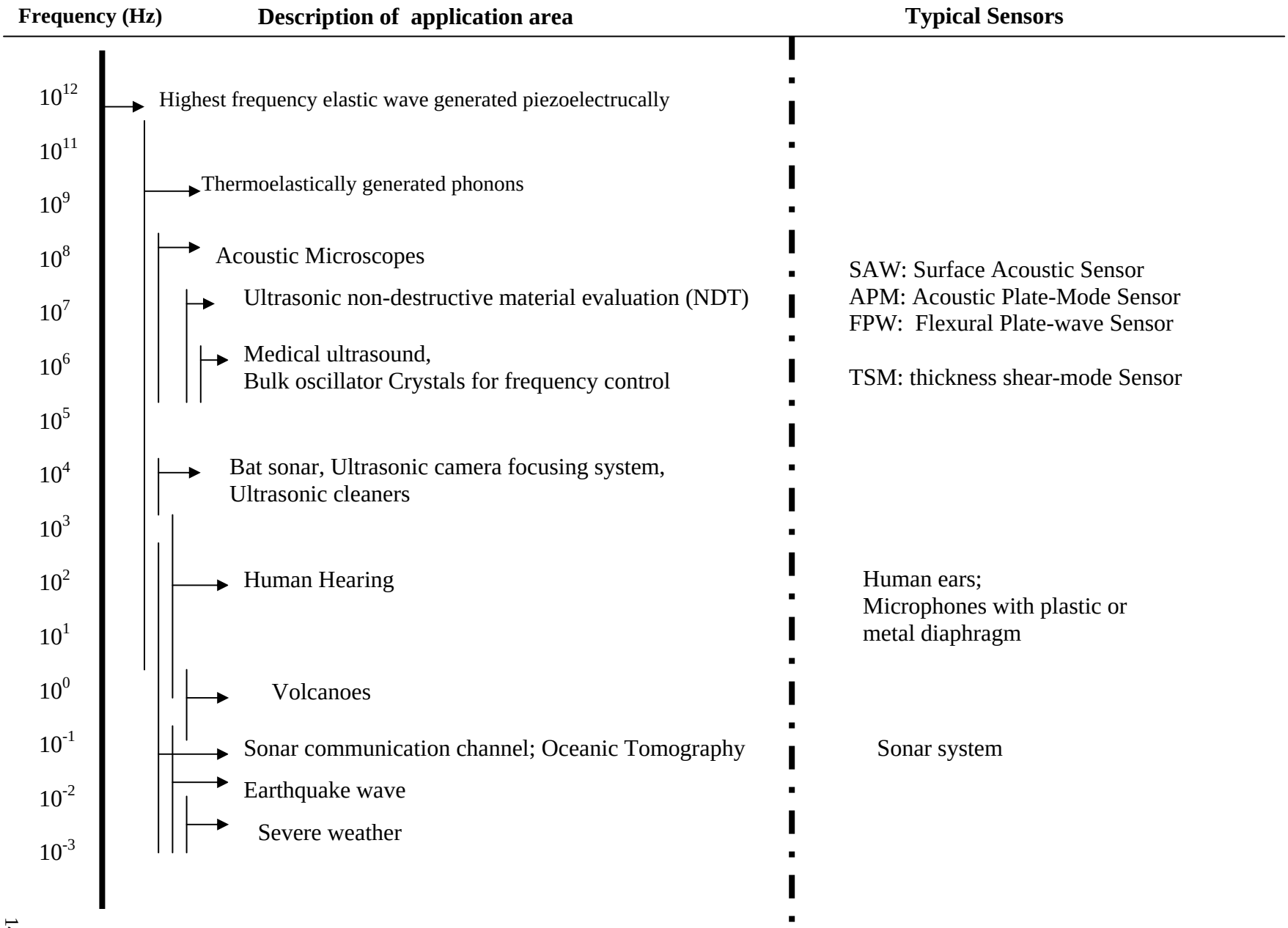

Chapter 2. Theory of Diaphragm-Based Optical Fiber Acoustic Sensors

2.1 Sensor Configuration

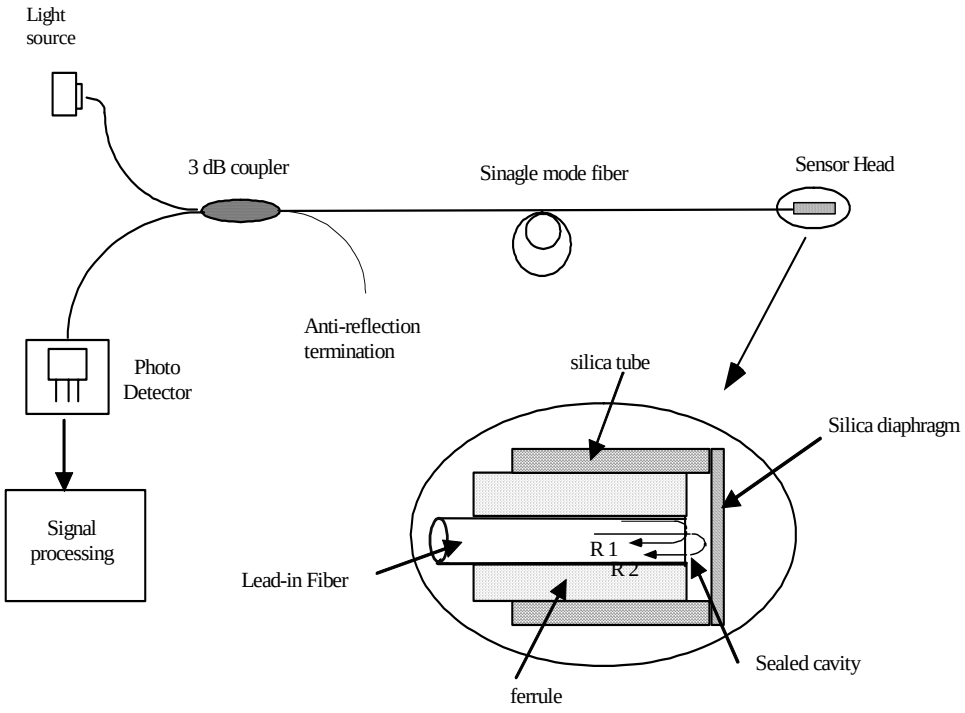

Figure 2.1 Illustration of the principle of the optical fiber acoustic sensor.

The basic configuration of the diaphragm-based optical fiber interferometric acoustic (DOFIA) sensor is illustrated in Figure 2. 1. The system consists of a sensor probe, a laser diode, an optoelectronic signal processing unit, and a single mode fiber linking the sensor probe and the signal-processing unit. The light source is launched into a 2×2 fiber coupler and propagates along the fiber to the sensor head. As shown in the enlarged view of the sensor head, the lead in/out fiber and the thin silica glass diaphragm are bonded together on a cylindrical silica glass tube/ferrule assembly to form a Fabry-Perot (FP) cavity. The incident light is first partially reflected (R_1) at the endface of the lead in/out fiber due to the Fresnel reflection at the glass-air interface. The remainder of the light propagates across the air gap to the inner surface of the diaphragm with reflectivity (R_2).

The two reflections travel back along the same lead-in fiber through the same fiber coupler to the photo-detection end. The interference of these two reflections produces intensity variations, referred to as interference fringes, as the air gap is continuously changed.

Obviously, in the sensor system, the diaphragm is the key element, which not only forms the FP cavity, but also works as a pressure 'vibrator' to sense the acoustic wave. In this chapter, the theory of the diaphragm-based interferometric acoustic sensor will be established on two fundamentals: optical interference theory, and diaphragm mechanical vibration theory. Based on the characteristics of sensor interference and diaphragm dynamic vibration, we will analyze the sensor sensitivity systematically, which is often the most concerned parameter in a sensing system.

2.2 Optical Interference Theory in DOFIA

2.2.1 Interference intensity in a Fabry-Perot interferometer

Consider a low-coherence light source, such as LEDs and superluminescence LEDs (SLEDs), illuminates an extrinsic Fabry-Perot interferometer (EFPI) formed by two mirrors. The optical intensity $I_0(\lambda)$ of the light source at wavelength λ is described as a Gaussian function[42, 43], as shown in Fig 2.1:

$$I_0(\lambda) = I_0 f(\lambda) = \frac{I_0}{(2\pi)^{1/2}\Delta\lambda}\exp[-(\lambda-\lambda_0)^2/(2\Delta\lambda^2)] \quad (2\text{-}1)$$

where $f(\lambda)$ is the spectral distribution of this laser, which typically shows

$$f(\lambda) = \frac{1}{(2\pi)^{1/2}\Delta\lambda}\exp[-(\lambda-\lambda_0)^2/(2\Delta\lambda^2)] \quad (2\text{-}2)$$

and λ_0 is the central wavelength, and $\Delta\lambda = \Delta\lambda_{FWHM}/(8\ln 2)^{1/2}$. I_0 is the output power after the pigtail at λ_0.

The coherence length L_c of a Gaussian source is inversely proportional to the spectral width of the source, given by

$$L_c \approx \frac{{\lambda_0}^2}{\Delta\lambda}, \tag{2-3}$$

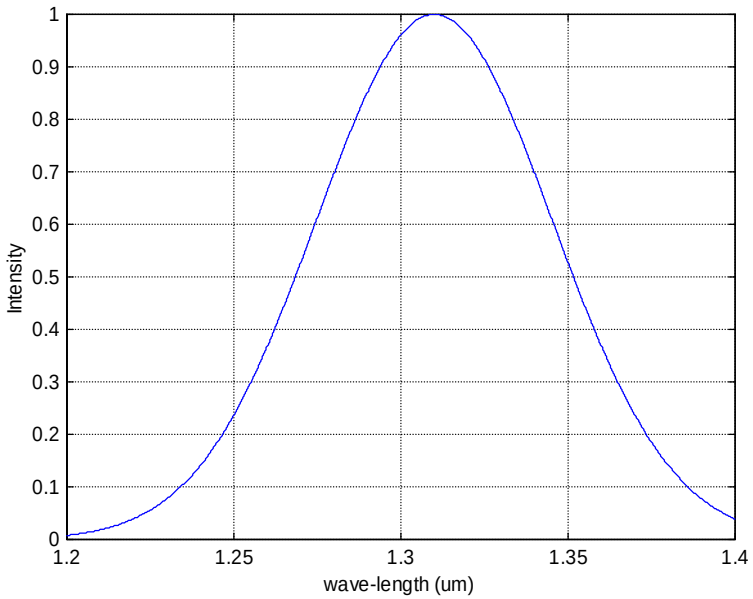

Figure 2.2 Typical laser spectrum (λ_0=1310nm)

For the interferometer consisting of two mirrors with arbitrary reflectivity (assuming that the fiber end and the diaphragm have reflectance R_1 *and* R_2, respectively), the interference intensity at wavelength λ is [7]:

$$I_r(\lambda) = [\alpha I_0 f(\lambda)] \frac{R_1 + \eta^2 R_2 - 2\eta\sqrt{R_1 R_2}\cos(4\pi n_0 L/\lambda)}{1 + \eta^2 R_1 R_2 - 2\eta\sqrt{R_1 R_2}\cos(4\pi n_0 L/\lambda)} \tag{2-4}$$

where α is the loss coefficient of the optical path (from the source to the sensor and from the sensor to the receiver), L is the air-gap length, n_0=1 is the refractive index of the air in the cavity, and η is the coupling efficiency for the round-trip between the fiber-end to the diaphragm. Provided that the diaphragm is parallel to the fiber-end, η can be calculated by [44]

$$\eta = 1/\{1 + [2\lambda_0 L/(2\pi n_0 w^2)]^2\} \tag{2-5}$$

where *w* is the mode spot-size of the single mode fiber. Therefore, the total optical power received by the receiver can be expressed as

$$I = \int_{\lambda_0 - BW/2}^{\lambda_0 + BW/2} I_r(\lambda) d\lambda$$

$$= \frac{\alpha I_0}{(2\pi)^{1/2}\Delta\lambda} \int_{\lambda - BW/2}^{\lambda + BW/2} \frac{R_1 + \eta^2 R_2 - 2\eta\sqrt{R_1 R_2}\cos(4\pi n_0 L/\lambda)}{1 + \eta^2 R_1 R_2 - 2\eta\sqrt{R_1 R_2}\cos(4\pi n_0 L/\lambda)} \exp[-(\lambda - \lambda_0)^2/(2\Delta\lambda^2)] d\lambda \tag{2-6}$$

where *BW* is the total spectrum width.

Eq. (2.6) gives the integrated expression of interference signal for most of EFPI systems, which involves most of the key factors in the sensor system, such as the cavity length, source central wavelength and bandwidth, reflectance of surfaces, and optical loss.

Usually, two parameters are defined to evaluate the quality of an optical interferometer: fringe visibility γ and fineness. The fringe visibility is defined as,

$$\gamma = \frac{I_{\max} - I_{\min}}{I_{\max} + I_{\min}} \tag{2-7}$$

where I_{min} and I_{max} are the minimum and maximum intensities of the optical interference, respectively. According to Eq. (2-6), we may obtain:

$$\gamma = \frac{4\eta\sqrt{R_1 R_2}(1 - R_1)(1 - \eta^2 R_2)}{(R_1 + \eta^2 R_2)(1 + \eta^2 R_1 R_2) - 4\eta^2 R_1 R_2} \tag{2-8}$$

It is clear that the fiber sensor's visibility relies on the surface reflectance and the cavity length. Higher fringe visibility always means higher performance in terms of sensitivity.

For the case of R_1=R_2=R, we usually define the fineness of the interferometer as [45]:

$$F = \pi R^{1/2}/(1 - R) \tag{2-9}$$

When $R<<1$, we have $F<1$, then Eq. (2-6) becomes,

$$I = \frac{\alpha I_0}{(2\pi)^{1/2}\Delta\lambda}\int_{\lambda-BW/2}^{\lambda+BW/2} R(1+\eta^2-2\eta\cos(4\pi n_0 L/\lambda))\exp[-(\lambda-\lambda_0)^2/(2\Delta\lambda^2)]d\lambda \tag{2-10}$$

This is typical low-finesse FP interferometer signal, which performs sinusoidal fringe. When R_1 and R_2 are within 0.1 to 0.5, the interferometer has medium-fineness $1<F<5$.

2.2.2 Interference fringes versus surface reflectance

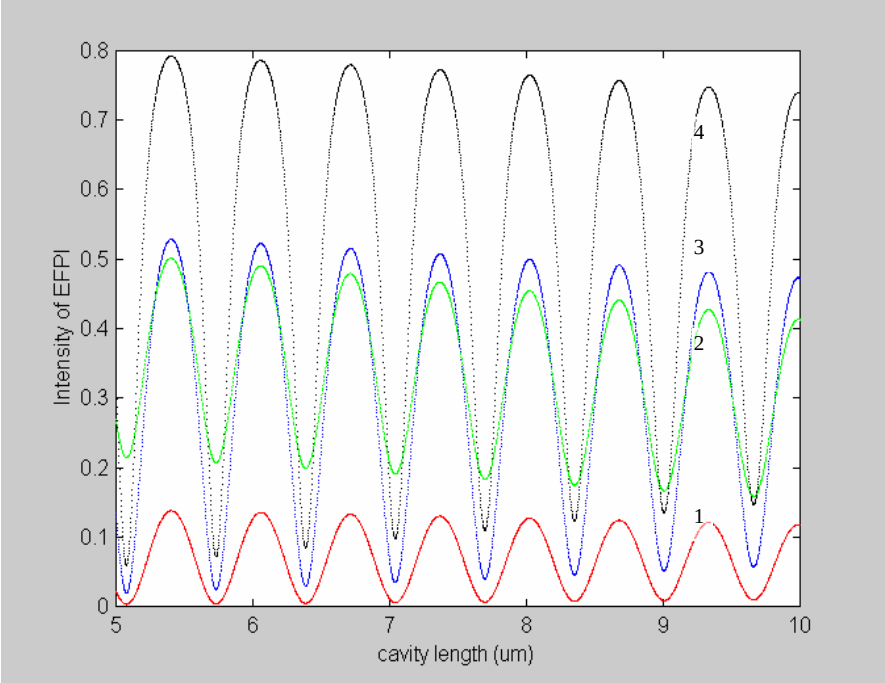

Figure 2.3. Interference fringe intensity for different reflectivity
(curve 1, $R_1=R_2=0.04$; curve 2, $R_1=0.04$ *and* $R_2=0.4$, curve 3, $R_1=R_2=0.2$, curve 4, $R_1=R_2=0.4$)

Figure 2.3 shows the reflection interference fringes with different surface reflectivity, based on Eq. (2-6). Obviously, comparing with the low-fineness interferometric sensor (as curve 1 in Figure 2.3), the sensor with higher reflectance (higher fineness) has higher intensity. However, higher fringe intensity doesn't mean better visibility. Figure 2.4 illustrates the fringe visibility for each interference curve in Figure 2.3. The low-fineness ineterferometer (curve 1) has better visibility than that with higher reflectance (curve2, 3 and 4).

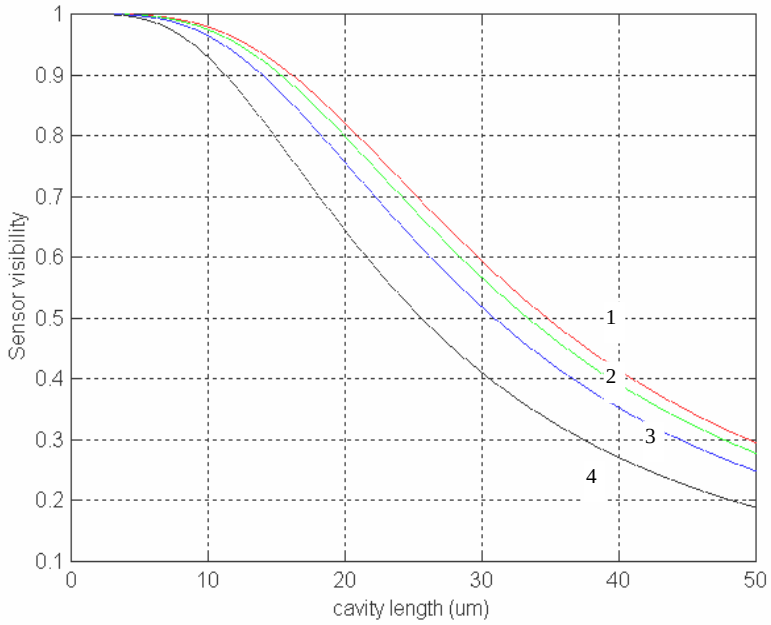

Figure2.4 Fringe visibility for different reflectance

(λ_{FWHM}=50nm, curve 1, $R_1=R_2=0.04$; curve 2, $R_1=0.04$ *and* $R_2=0.4$, curve 3, $R_1=R_2=0.2$, curve 4, $R_1=R_2=0.4$)

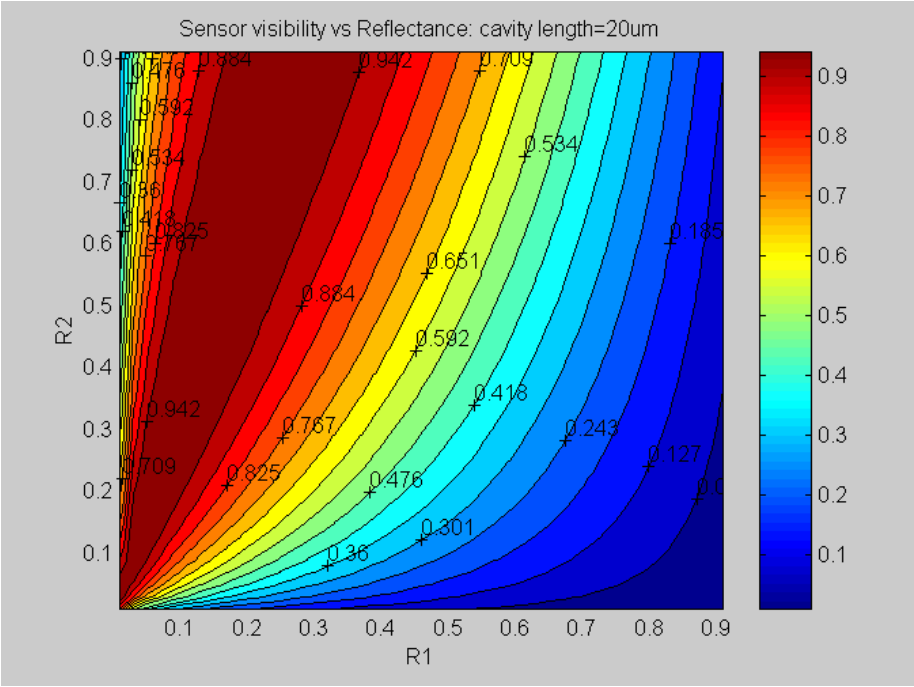

Figure 2.5 Sensor visibility as function of surface reflectance (L=20um, λ_{FWHM}=50nm)

Figure 2.5 illustrates the visibility of interferometer (with cavity length 20μm) for different surface reflectance. To keep the sensor visibility greater than 80%, it is noticed that the reflectance of the first surface should be within the range of 0.01 to 0.5, while R_2 has larger window from 0.01 to 0.9. The main reason of this is that the interferometer has the best visibility when $R_1 = \eta^2 R_2$, so the second surface should provide higher reflectance to compensate the coupling loss between two surfaces. Since η is a function of cavity length as indicated in Eq. (2-5), it is necessary to keep R_2 much higher than R_1 for long cavity interferometer. On the contrary, shorter cavity will give us more flexibility on the reflectance design. In practice, we chose L less than 10 μm, and $R_1 \sim 0.1$, and R_2 in the range of 0.4~0.9. This will ensure the interferometric sensor a higher intensity, as well as an enough fringe visibility.

2.2.3 Interference fringes versus cavity length and source band-width

Fig 2.6 shows the interference fringes as a function of the cavity length for two cases: case 1, the band-width of light-source is 50nm, shown in Fig 2.6; and case 2, light source band-width is 20nm, shown in Fig 2.7.

From Figure 2.6 and Figure 2.4, we may easily observe the impact of the cavity length on the fringes. With increasing cavity length, both the absolute interference intensity and fringe visibility decrease. This phenomenon results from two facts: 1) Due to the divergent property of light beam out of the single-mode fiber, the loss increases with the cavity length, as indicated in Eq. (2-5). 2) To obtain an interference signal from the interferometer, the optical path difference (OPD) has to be smaller than the coherence length of the source described in Eq. (2-3). If the OPD of the interferometer is close to or larger than the coherence length of the source being used, the two optical waves will not effectively interfere to generate fringes.

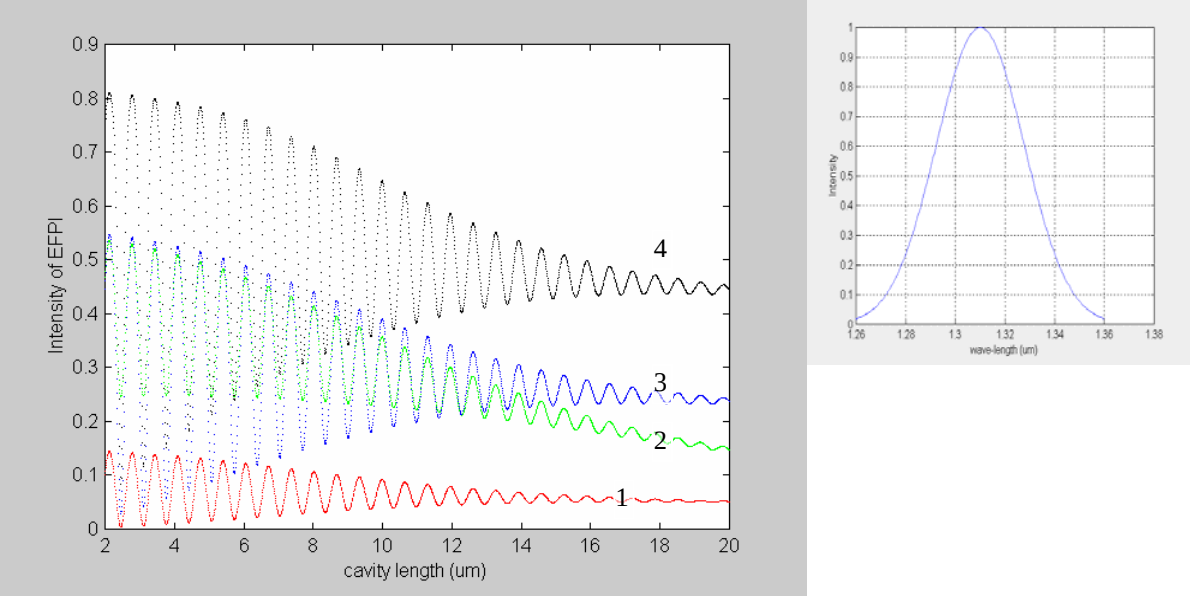

Figure 2.6 Interference fringe via cavity length

(λ_{FWHM}=50nm, curve 1, $R_1=R_2=0.04$; curve 2, $R_1=0.04$ *and* $R_2=0.4$, curve 3, $R_1=R_2=0.2$, curve 4, $R_1=R_2=0.4$)

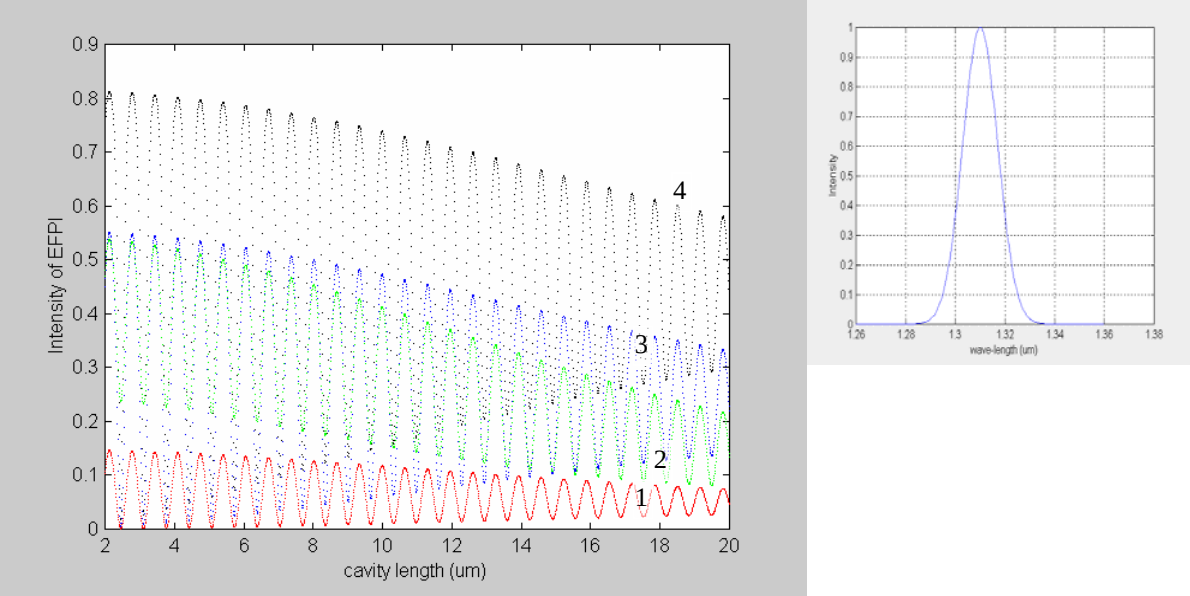

Figure 2.7 Interference fringe via cavity length

(λ_{FWHM}=20nm, curve 1, $R_1=R_2=0.04$; curve 2, $R_1=0.04$ *and* $R_2=0.4$, curve 3, $R_1=R_2=0.2$, curve 4, $R_1=R_2=0.4$)

Therefore, for the sensor with short coherentlength (wide band source), the cavity length is required to be short, in order to get higher fringe visibility. For example, if using 50nm band-width source, the air cavity should be kept within 10 μm, which places more difficult manufacturing constraints to the sensor head. In contrast, if the $\Delta\lambda_{FWHM}$ is reduced to 20 nm, interference fringes will still keep good visibility even when the air gap is above 20 μm, as shown in Figure 2.7, which gives more flexibility for sensor head fabrication.

2.2.4 Sensitivity

In our sensor, the acoustic signal generated by partial discharges can cause deformation of the diaphragm, which modulates the sealed air gap length. The sensor therefore gives outputs that correspond to the acoustic signals, as shown in Figure 2.8, in which the sinusoidal interference intensity of a low-fineness sensor is taken as an example.

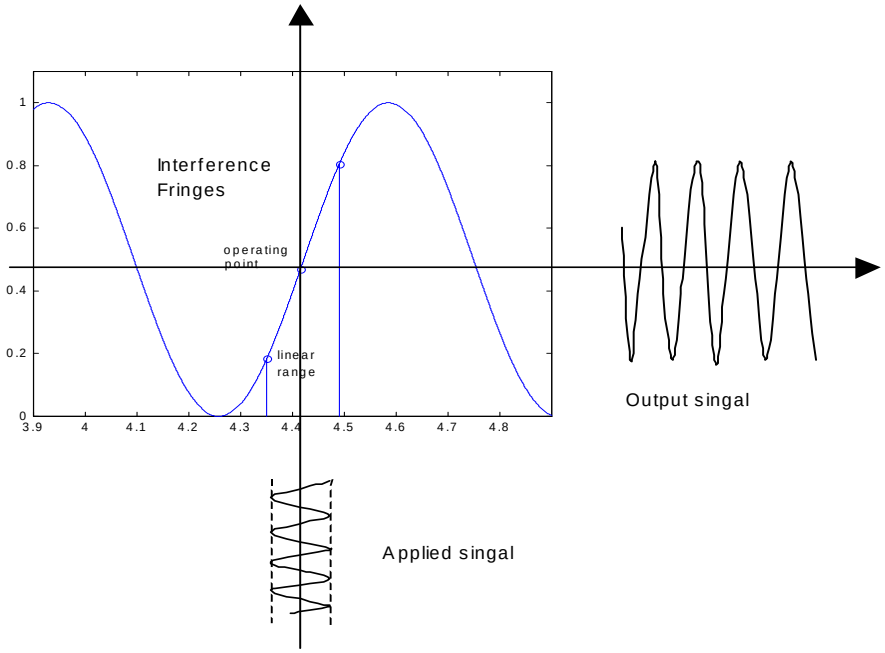

Figure 2.8 Illustration of a linear operating range of the sensor response curve.

The sensitivity of an interferometer (I_{sens}) can be defined as the intensity change produced in response to unit air gap change. For the sake of convenience, we consider a single

wavelength light incident on an interferometric sensor that has the same reflectance ($R_1=R_2=R$) on both surfaces, and assume the coupling efficiency is close to 1. According to Eq. (2-6), I_{sens} can be expressed as

$$I_{sens} = abs(\frac{dI}{dL}) = abs(\alpha I_0 \frac{2\eta R(1-\eta^2 R)(1-R)\cdot\frac{4\pi}{\lambda}\sin(\frac{4\pi L}{\lambda})}{[1+\eta^2R^2-2\eta R\cos(\frac{4\pi L}{\lambda})]^2}) \quad (2\text{-}11)$$

$$\overset{\eta\approx 1}{=} abs(\alpha I_0 \frac{2R(1-R)^2\cdot\frac{4\pi}{\lambda}\sin(\frac{4\pi L}{\lambda})}{[1+R^2-2R\cos(\frac{4\pi L}{\lambda})]^2})$$

According to Eq. (2-11), the interferometer is very sensitive to the air-gap change. However, it is also noticed that the measurement would suffer from the disadvantages of sensitivity reduction and fringe direction ambiguity when the sensor reaches peaks or valleys of the fringes, as shown in Figure 2.8. Fringe direction ambiguity is defined as the difficulty in determining whether the air gap is increasing or decreasing by detecting the optical intensity only. If a measurement starts with an air gap corresponding to the peak of a fringe, the optical intensity will decrease, regardless whether the gap increases or decreases.

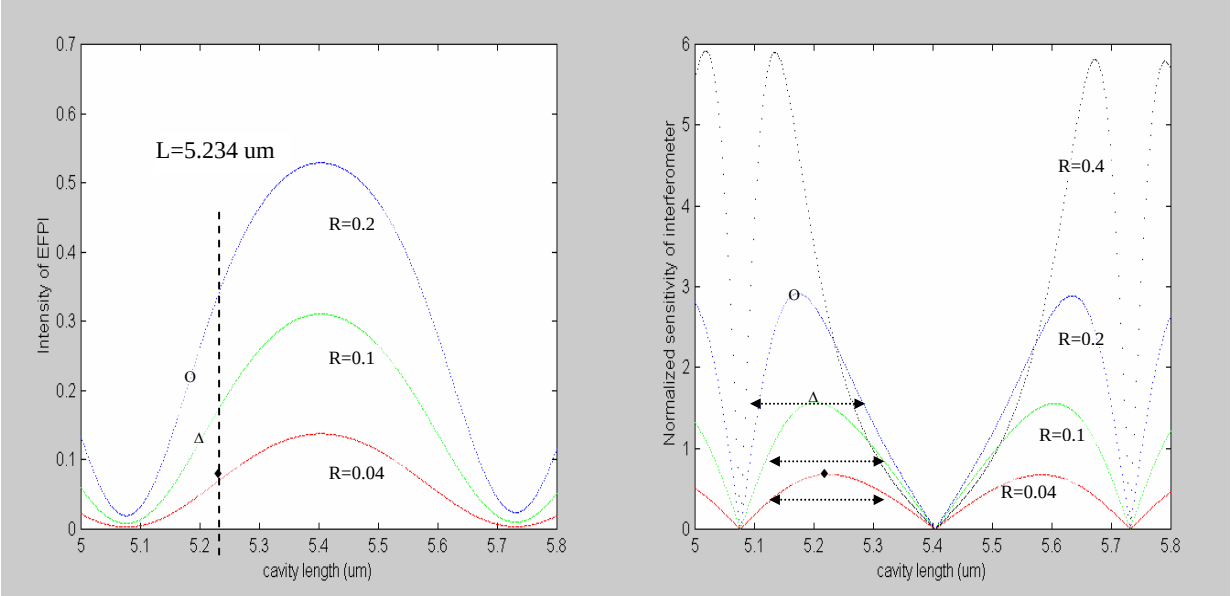

(a) (b)

Figure 2.9(a), Interference fringes for different reflectance, and (b) corresponding sensitivity curves for each fringe.

To solve these problems, the sensor head is designed so that the cavity length is close to the operating point (O-Point) where the sensor has the maximum sensitivity ($I_{sens\text{-}max}$). Figure 2.9(a) shows the normalized interference fringes from sensor a head with an airgap length change from 5 μm to 5.8 μm, at different reflectance *R=0.04, 0.1* and *0.2*. Correspondingly, the interferometer sensitivity curves at different cavity lengths are illustrated in Figure 2.9 (b).

Figure 2.9 indicates that the sensitivity at O-point increases with a reflectance increase. For practical convenience, we introduce the factor Λ to describe the reflection-induced sensitivity increase in reference to the sensitivity at $R_0=0.04$. For example, the increase of the reflectivity R from 0.04 to 0.2 results in a sensitivity increase by a factor Λ=4.54 (from 0.65 to 2.95 at O-point). Table 2.1 shows some commonly-used Λ factors for different surface reflectance. Therefore, the interferometer sensitivity at the O-point for different reflectance is

$$I_{sen}(R) = \alpha \cdot \Lambda \cdot I_0 \cdot 2R_0 \cdot \frac{4\pi}{\lambda} \tag{2-12}$$

Table 2.1 Reflection-sensitivity increase factor Λ

$R_1=R_2=R$	0.04	0.1	0.2	0.4
Λ	1	2.46	4.54	9.06

At the same time, according to Figure 2.9, it is noticeable that the O-point drifts toward the valley of the fringes when the reflectance is increased. For R=0.04, the interference intensity has sinusoidal shape due to the low-fineness, and the maximum sensitivity ($I_{sens\text{-}max}$) obtained at the quadrature points (Q-points) of the interference fringes where:

$$\frac{4\pi L}{\lambda_c} = \frac{\pi}{2} + k\pi, \qquad k = 0,1,2,3....$$

So, one of the O-points in Figure 2.9(a) is at L=5.234um for R=0.04. While, for R=0.2, the O-point shifts to L=5.165.

In practice, it is not easy to make the cavity length locate exactly on the O-point. Actually, for the sensor with medium fineness, the sensor will work with an acceptable sensitivity if the cavity length is designed within the operating range (L_{FSO}) around the O-point, which is defined as

$$L_{FSO} = \frac{\lambda}{4} \cdot 50\% \quad \text{(in } \mu\text{m)}$$

2.3 Diaphragm Dynamic Vibration Theory

As shown in the enlarged view of Figure 2.1, the sensor head is fabricated by bonding the fiber and the silica diaphragm in or on the silica ferrule/tubing together to form a sealed fiber optic extrinsic Fabry-Perot interferometer (EFPI). This kind of sensor structure can be simplified as a circular plate clamped at its circular edges, as shown in Figure 2.10. The diaphragm vibrates at the presence of an acoustic wave that imposes a dynamic pressure on the diaphragm. In this section, the frequency response and pressure sensitivity of the sensor head will be introduced based on a diaphragm vibration analysis.

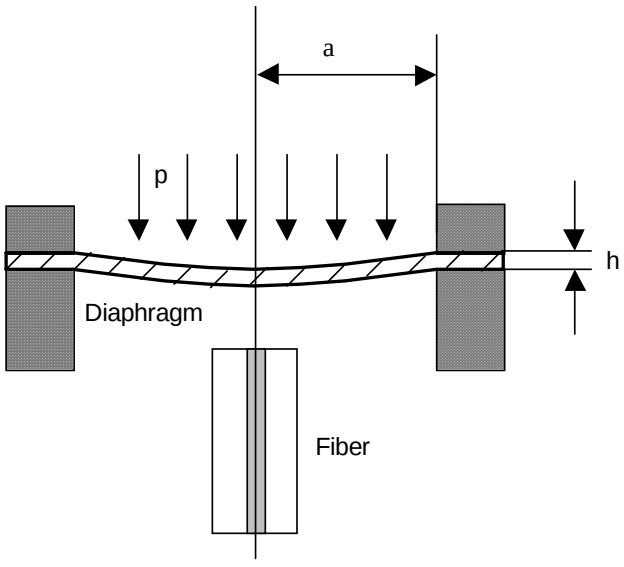

Figure 2.10 Structure model for diaphragm-based acoustic sensor

2.3.1 Diaphragm deflection

The diaphragm will be deflected when there is a differential pressure *p* between the inside and outside of the sealed cavity. The out-of-plane deflection of the diaphragm *u* is a function of the pressure difference at any radium position *r* given as [46]

$$u = \frac{3(1-\mu^2)p}{16Eh^3} \times (r^2 - a^2)^2 . \tag{2-13}$$

where *a* is the radium of the diaphragm. Usually, we define the ratio between the deflection and the pressure difference as the diaphragm pressures sensitivity (δ_{diap}), which partially determines the whole sensor system's pressure sensitivity that will be described in the following section. In our sensor configuration, the fiber is positioned to the center of the diaphragm so that only the center deflection u_0 is interested. Based on the properties of fused silica shown in Table 2.2, δ_{diap} is given by

$$\delta_{diap} = \frac{u_0}{p} = \frac{3(1-\mu^2)}{16Eh^3} \times a^4 = 1.71 \times 10^{-8} \frac{a^4}{h^3}, \tag{2-14}$$

where u_0 is in microns, and *p* is in pounds per square inch (*psi*), so δ_{diap} is in $\mu m/psi$. Figure 2.11 shows the sensor sensitivity predicted by Eq. (2-14).

Table 2.2 Properties of fused silica (@25 ^{o}C)

Density	$w(\rho\rho)$	2.202 x 10^3	Kg/m^{-3}
Young's Modulus	E	73.73 x 10^9	Pa
Poisson's Ratio	$\mu\mu$	0.17	-
Max. tensile stress	$\sigma\sigma_m$	~1.5 x 10^9	Pa
Coefficient of thermal expansion	$\alpha\alpha_T$	~5.5~7.5 x10^{-7}	(°C)$^{-1}$

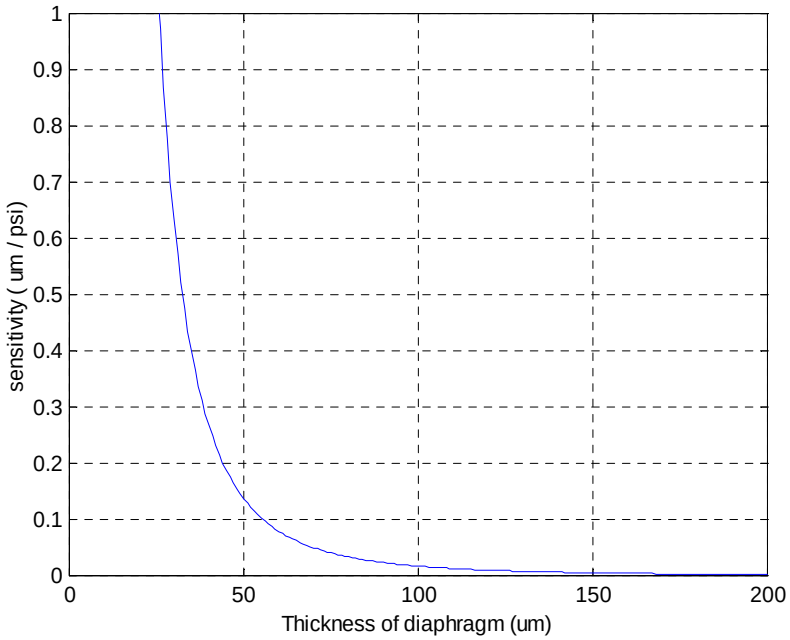

Figure 2.11 Predicted diaphragm sensitivity (μm/psi) versus diaphragm thickness at *a=1* mm.

For the diaphragm-based pressure sensor, the maximum tolerable pressure P_{max} corresponds to the maximum tolerable tensile stress, which occurs at the center of the diaphragm. It is given by

$$P_m = \sigma_m \frac{8}{3(1+\mu)} \frac{h^2}{a^2} = 4.9 \times 10^5 \times \frac{h^2}{a^2} \qquad \text{(in psi)} \qquad (2\text{-}15)$$

The maximum linear response pressure P_o, which is defined as the maximum pressure within which the diaphragm strain/pressure relation remains approximately linear, is given by

$$P_0 = \frac{8E}{3(1-\mu^2)} (\frac{h}{a})^4 = 2.939 \times 10^7 \times (\frac{h}{a})^4 \qquad \text{(in psi)} \qquad (2\text{-}16)$$

Figure 2.12 illustrates relationships between the thickness and the maximum tolerable pressure and the maximum linear response pressure. Generally, P_m and P_0 should be much larger than the acoustic pressure to be detected, which ensure the sensor work without risk of glass breakage.

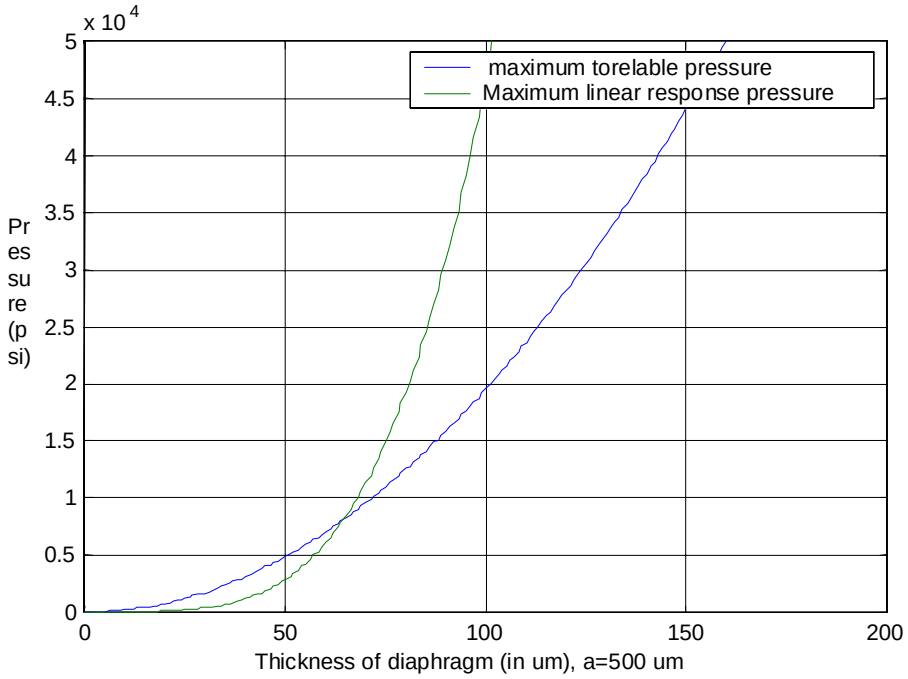

Figure 2.12. Maximum tolerable pressure and linear response pressure of sensors

2.3.2 Natural frequency of circular plates clamped at boundary

(1) Free circular plate vibration [47]

Assuming there is no pressure on the surface of a diaphragm, the equation of motion for free vibration is,

$$D\nabla^2 u(r,\theta,t) + \rho h \frac{\partial^2 u(r,\theta,t)}{\partial t^2} = 0 \qquad (2\text{-}17)$$

where h is thickness of plate (m), ρ stands for mass density, $u(r,\theta,t)$ is the displacement of vibrating diaphragm; ∇^2 is the opterator $\nabla^2(\bullet) = \frac{\partial^2(\bullet)}{\partial r^2} + \frac{1}{r}\frac{\partial(\bullet)}{\partial r} + \frac{1}{r^2}\frac{\partial^2(\bullet)}{\partial \theta^2}$, and D is the flexural rigidity of the diaphragm defined by

$$D = \frac{Eh^3}{12(1-\mu^2)} (\mathrm{N/m^2}). \qquad (2\text{-}18)$$

where μ is the Poisson's ratio; E is the Young's modulus of the silica glass material. Set $u(r,\theta,t) = U(r,\theta)e^{j\omega t} = R(r)\Theta(\theta)e^{j\omega t}$, and $\lambda^4 = \frac{\rho h\omega^2}{D}$, the motion equation becomes:

$$\begin{aligned} &\frac{d^2\Theta}{d\theta^2} + k^2\Theta = 0 \\ &\frac{d^2R}{dr^2} + \frac{1}{r}\frac{dR}{dr} + (\pm\lambda^2 - \frac{k^2}{r^2})R = 0 \end{aligned} \tag{2-19}$$

For the first equation, we have solution:

$$\Theta = A\cos(k\theta) + B\sin(k\theta) \qquad k=n=0,1,2,3\ldots \tag{2-20}$$

For the second equation, set $\xi^2 = \pm\lambda r$ for $(\pm\lambda^2)$, we get

$$\frac{d^2R}{d\xi^2} + \frac{1}{\xi}\frac{dR}{d\xi} + (1 - \frac{k^2}{\xi^2})R = 0 \tag{2-21}$$

The solution is Bessel's functions. For $\xi = \lambda r$, the solution is Bessel functions of the first & second kind, $J_k(\lambda r)$ and $I_k(\lambda r)$; for $\xi = j\lambda r$, the solution is modified Bessel functions of the first & second kind, $Y_k(\lambda r)$ and $K_k(\lambda r)$. So the total solution of the circular plate is,

$$R(\lambda r) = CJ_n(\lambda r) + C'I_n(\lambda r) + FY_n(\lambda r) + F'K_n(\lambda r) \tag{2-22}$$

C, C', F, and *F'* are constant for each solution components. For plate clamped at boundary, $F = F' = 0$, and

$$u(a,\theta,t) = 0$$

$$\frac{\partial u}{\partial r}(a,\theta,t) = 0$$

we have, $R(a) = 0$ and $\frac{dR}{dr}(a) = 0$

$$\begin{bmatrix} J_n(\lambda r) & I_n(\lambda r) \\ \frac{dJ_n}{dr}(\lambda r) & \frac{dI_n}{dr}(\lambda r) \end{bmatrix} \begin{pmatrix} C \\ C' \end{pmatrix} = 0 \tag{2-23}$$

then,

$$J_n(\lambda r)\frac{dI_n}{dr}(\lambda r) - \frac{dJ_n}{dr}(\lambda r) I_n(\lambda r) = 0 \tag{2-24}$$

Searching this equation for its roots λa, labeled successively m=0,1,2,… for each n=0,1,2,…, gives the natural frequencies. Values of the roots $(\lambda a)_{mn}$ are collected in Table 2.3. The natural frequencies are related to these roots by

$$\omega_{mn} = \frac{(\lambda a)_{mn}^2}{a^2}\sqrt{\frac{D}{\rho h}} \tag{2-25}$$

the mode-shape can be expressed, and

$$U(r,\theta) = A\left[J_n(\lambda r) - \frac{J_n(\lambda a)}{I_n(\lambda a)} I_n(\lambda r) \right] \cos n(\theta - \phi)$$

Table 2.3 Value of $(\lambda a)_{mn}$

m \ n	0	1	2	3
0	3.196	4.611	5.906	7.143
1	6.306	7.799	9.197	10.537
2	9.44	10.958	12.402	13.795
3	12.577	14.108	15.579	17.005

From the properties of fused silica shown in Table 2.2, the frequency response of the sensor can thus be calculated by combining Eq. (2-18) and (2-25) into the following

$$f_{mn} = 2.749 \times 10^9 \times \frac{\alpha_{mn}}{\alpha_{00}} \frac{h}{a^2} \text{ (Hz)} \tag{2-26}$$

where $\alpha_{mn}=(\lambda a)_{mn}$, h and r are in microns.

If a plate is immersed in a fluid, its natural frequencies may be considerably altered. In order to take the mass of the fluid into account for the fundamental mode of vibration, Eq. (2-25) should be replaced by,

$$\omega_{mn}^{l} = \frac{1}{\sqrt{1+\zeta}}\omega_{mn} = C\omega_{mn} \tag{2-27}$$

in which,

$$C = \frac{1}{\sqrt{1+\zeta}}, \text{ and } \zeta = 0.6689\frac{\rho_1}{\rho}\frac{a}{h}$$

where (ρ_1/ρ) is the ratio of mass density of the fluid to that of the material of the plate.

$$f_{mn}^{l} = C \times 2.749 \times 10^{9} \times \frac{h}{a^2} \tag{2-28}$$

For example, considering the sensor with $a=1$ mm and h=100 μm is immersed in water (ρ_w=1.0X10^3 kg/m^3) and transformer oil (ρ_{oil}~0.9X10^{3}kg/m^3), which have C_w= 0.48 and C_{oil}=0.50. The frequency response of the sensor will be lowered to 0.48 and 0.50 times its original value in air, respectively.

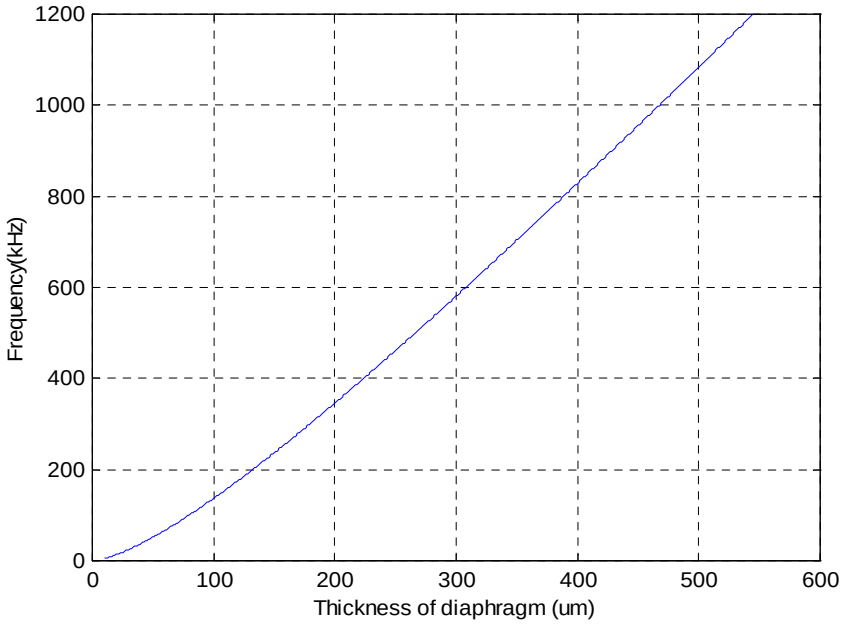

Figure 2.13 Predicted frequency response of the sensor at $r=1$ mm

As indicated by Eq. (2-26), the sensor's frequency response in liquid is proportional to the thickness of the diaphragm and inversely proportional to the square of the effective diaphragm radius. If we choose the diaphragm with the effective radius of 1 mm, we can plot the predicted frequency response of the sensor as a function of diaphragm thickness as shown in Figure 2.13.

(2) Forced vibration of diaphragm

According to Eq. (2-13), when the circular plate with clamped edges is under uniformly static pressure, the maximum displacement (u_{max}) is expressed as following:

$$u_{\max} = \frac{3(1-\mu^2)p}{16Eh^3} \times a^4 \tag{2-29}$$

Considering a plate is under a load varying harmonically with time, the equation of motion is

$$D\nabla^2 u + \rho h \frac{\partial^2 u}{\partial t^2} + \nu \frac{\partial u}{\partial t} = pe^{iqt} \tag{2-30}$$

in which ν is coefficient corresponding to the damping of liquid, q is the frequency of varying pressure, and p is the amplitude of varying pressure. Set,

$$\omega^2 = \frac{D}{\rho h}, 2n = \frac{\nu}{\rho h}, P = \frac{p}{\rho h}$$

then the solution of Eq.(2-30) is

$$u = e^{-nt}(A'\sin\omega_1 t + B'\cos\omega_1 t) - \frac{2qPn}{(\omega_{mn}^2 - q^2)^2 + 4q^2n^2}\cos(qt) + \frac{P(\omega^2 - q^2)}{(\omega_{mn}^2 - q^2)^2 + 4q^2n^2}\sin(qt) \tag{2-31}$$

where $\omega_1^2 = \omega_{mn}^2 - n^2$, and ω_{mn} is the natural frequency defined by Eq. (2-25) in air and Eq. (2-27) in the liquid.

It is obviously that the ω_1 components will vanish after long enough time, so the response of plate will be harmonic with the frequency of acoustic pressure but lagging behind by a phase ϕ_k:

$$u = \Sigma \sin(qt - \phi_k) \tag{2-32}$$

where $\tan\phi_k = \dfrac{2qn}{\omega_{mn}^2 - q^2}$, and Σ is the intensity modulation factor, which is defined as

$$\Sigma = \frac{P}{\sqrt{(\omega_{mn}^2 - q^2) + 4q^2n^2}} \tag{2-33}$$

This means that the intensity will resonate at the natural vibration frequency of the diaphragm. We define β_{mn} as the enhancement coefficient of each vibration mode,

$$\beta_{mn} = \frac{\Sigma_{force}}{\Sigma_{no-force}} = \frac{\omega_{mn}^2}{\sqrt{(\omega_{mn}^2 - q^2)^2 + 4q^2n^2}} \tag{3-34}$$

Considering the maximum displacement of the diaphragm occurs when frequency is 0 (static case), the vibration response of the diaphragm at its central point is:

$$u_{mn}(q) = u_{\max} \bullet \beta_{mn}(q) = \frac{3p(1-\mu^2)}{16Eh^3} a^4 \frac{\omega_{mn}^2}{\sqrt{(\omega_{mn}^2 - q^2)^2 + 4q^2n^2}} \tag{2-35}$$

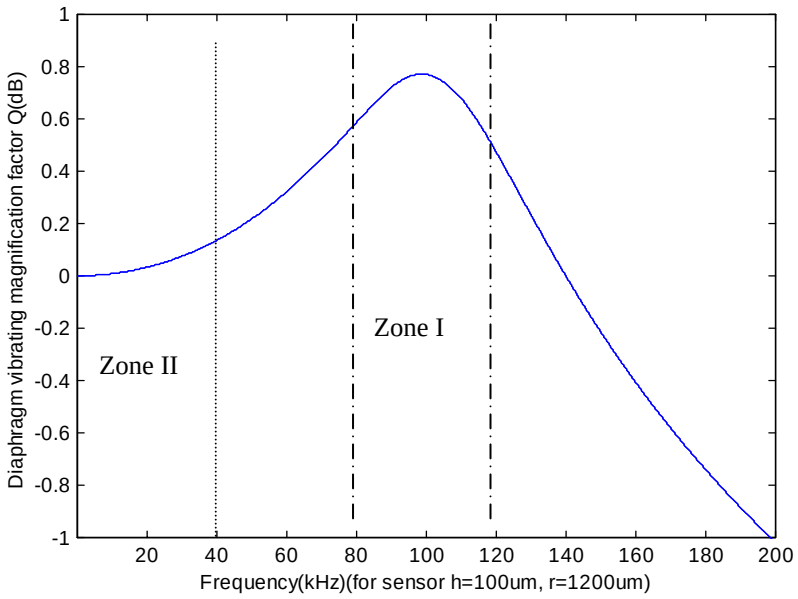

Figure 2.14. Sensor frequency response with single-mode resonance

Figure2.14 shows a typical sensor frequency response around its fundamental natural frequency. In this case, the sensor has a diaphragm with 100 μm in thickness, 1100 μm in diameter, and is immersed in water (ρ_1*~0.9*, and damping coefficient *n~20*). Its natural frequency in water is f_{00} = 113 kHz. Obviously, the intensity is enhanced about 6 times around 110 kHz due to the resonance. Therefore, if a designed sensor has fundamental natural frequencies close to the frequency of detected acoustic wave, the sensor would provide ultra- high sensitivity, which is called narrow-band sensor.

However, since the narrow-band sensor works at the non-linear range of the diaphragm vibration, it is not straightforward to quantitatively predict the acoustic intensity from the diaphragm deformation. Sometimes, in order to ensure the sensor working in the linear range, where vibration amplitude of diaphragm is proportional to the pressure of acoustic waves, the fundamental natural frequency of the sensor should be at least 2.5 times larger than the working frequency of acoustic pressure. This kind of sensor is called broad-band sensor, which works in Zone II as shown in Fig 2.14. In this frequency zone, the frequency response of the sensor would be maintained relatively 'flat'.

Actually, if the fundamental natural frequency of the diaphragm is smaller than the frequency of the impinging acoustic wave, not only the fundamental natural frequency, but also other natural frequency components will be excited. Thus, the vibration of the diaphragm will consist of a set of natural modes, and may be described as:

$$U(q) = u_{\max} \bullet \sum_{m=0,n=0}^{\infty} A_{mn}\beta_{mn}(q) = \frac{3p(1-\mu^2)}{16Eh^3}a^4 \sum_{m=0,n=0}^{\infty} \frac{A_{mn}\omega_{mn}^2}{\sqrt{(\omega_{mn}^2 - q^2)^2 + 4q^2n^2}} \qquad (2\text{-}36)$$

where A_{mn} is the weight constant for each mode.

For the previous sensor (*h= 100μm, a=1200μm*) with f_{00} = 113 kHz in water, Figure 2.15 shows the theoretic results of sensor's normalized response to the acoustic pressure, in which three vibration modes are considered. The result is very similar to that from experiment shown in Figure 2.16. In the figure, there are 2 response peaks around 110kHz and 210kHz, which correspond to the first and second vibration modes.

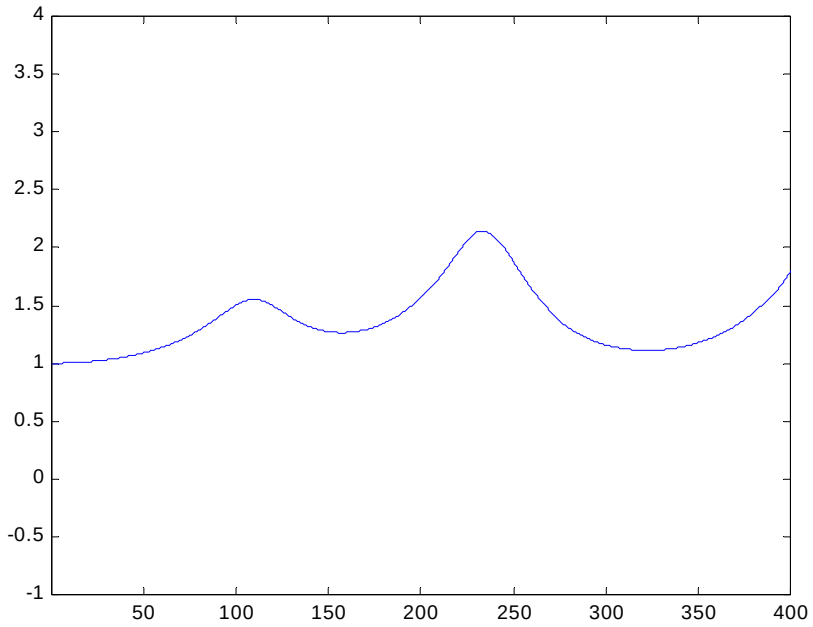

Figure 2.15 Normalized frequency response of diaphragm based sensor (Theoretical)

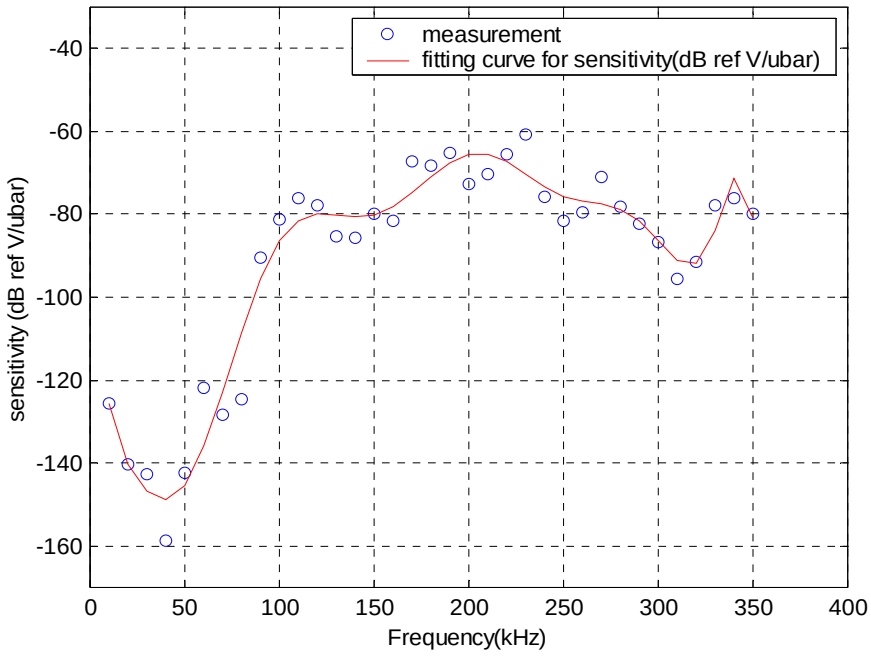

Figure 2.16 Experimental result of Sensor frequency response

(*h= 100um, a=1200um, I_0~2mW, f_{00}=110kHz*)

According to these results, we have several conclusions:

1) When the natural frequency is close to the acoustic frequency, the vibration will be magnified and the frequency response is no longer flat. But it is where the sensor with very high sensitivity can be designed (Narrow band sensor).

2) To maintain the sensor frequency response flat in the frequency range (Broad band sensor), the fundamental natural frequency of the sensor should be at least 2.5 times than the working frequency of dynamic acoustic pressure.

2.4 Sensor Responsivity and Sensitivity[*14]

As one of the most important performance parameters, the pressure responsivity (δ_{sys}) and resolution of our acoustic sensor system depend not only on the diaphragm sensitivity (δ_{diap}), but also on other components, such as the light source, the detector and the (pre)-amplifiers.

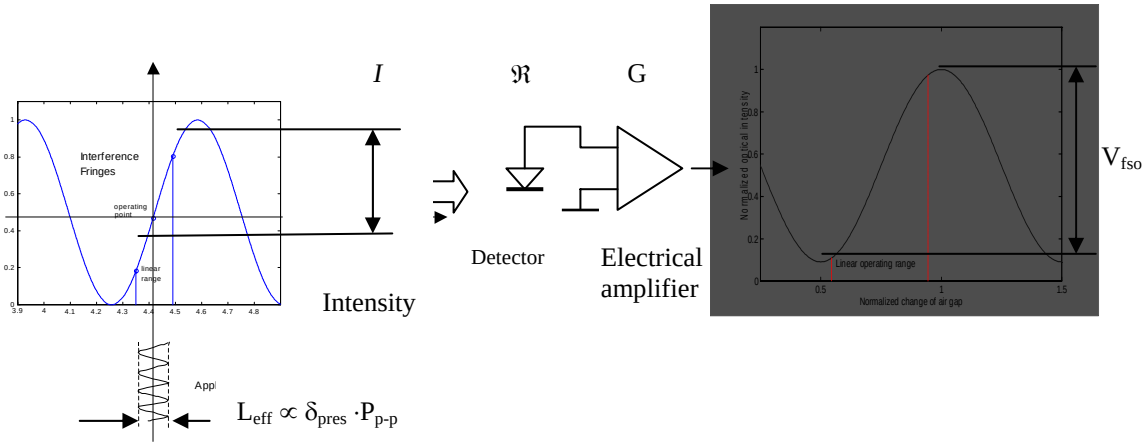

Figure 2.17 Acoustic pressure signal processing

Mathematically, the responsivity (δ_{sys}) may be calculated by dividing the Full Scale Output (FSO) of the sensor system by the Full Scale pressure or by determining the slope of a line fitted to multi-point calibration data. That is

*1) In optics the term *responsivity* is usually defined as the ratio of the change in the magnitude of an instrument output to the corresponding change in the magnitude of the measurand. *Resolution* is defined as the smallest increment of the measurand which can be detected by the instrument, sometime it is termed the *sensitivity* of a sensor system[48].

$$\delta_{sys} = \frac{dV_{out}}{dP} \tag{2-37}$$

The pressure detection resolution is defined as the minimum pressure (P-P) that can be detected, which depends on the signal-to-noise ratio (SNR) of the whole system. It can be expressed as

$$P_{res} = P_{FSO} \frac{V_{noise}}{V_{FSO}} \tag{2-38}$$

where V_{noise} is the system's noise, V_{FSO} is the Full Scale Output after amplifier, and P_{FSO} is the pressure which causes the output reaching V_{FSO}.

Figure 2.17 shows the signal processing of an acoustic pressure wave passing through the whole system, from which we can derive the expression of the responsivity and the sensitivity. After the amplifier, the output voltage of an acoustic signal is

$$V_{out} = \alpha \cdot \Re \cdot G \cdot I_0 \frac{R_1 + \eta^2 R_2 - 2\eta\sqrt{R_1 R_2}\cos(4\pi L/\lambda)}{1 + \eta^2 R_1 R_2 - 2\eta\sqrt{R_1 R_2}\cos(4\pi L/\lambda)} \tag{2-39}$$

where $\Re$ is the responsivity of the photo-detector (A/W), and G is the gain of the electrical amplifier. If $R_1=R_2=R$ and $\eta \sim 1$, the pressure responsivity of the sensor is

$$\delta_{sys} = \frac{dV_{out}}{dP} = \delta_{diap} \cdot \alpha \cdot \Re \cdot G \cdot R \cdot I_0 \frac{2R(1-R)^2 \cdot \frac{4\pi}{\lambda}\sin(\frac{4\pi L}{\lambda})}{[1 + R^2 - 2R\cos(\frac{4\pi L}{\lambda})]^2} \tag{2-40}$$

Assuming the sensor works near its maximum sensitivity point (O-point) and the displacement caused by P_{FSO} is smaller than L_{FSO}, according to Eq.(2-12), we have

$$\begin{aligned} \delta_{sys} &= 2 \cdot \delta_{diap} \cdot \Re \cdot G \cdot R_0 \cdot \alpha \cdot \Lambda \cdot I_0 \cdot \frac{4\pi}{\lambda} \\ &= 1.368 \cdot 10^{-7} \cdot \pi \cdot \Re \cdot G \cdot R_0 \cdot \alpha \cdot \Lambda \cdot I_0 \cdot \frac{a^4}{\lambda \cdot h^3} \end{aligned} \tag{2-41}$$

For example, if in our sensor system, r=1000 μm, h=100μm, λ=1.325μm, $\Re$ =0.9 (A/W), G = 6 x 10^6, $R=R_0=4\%$, Λ=1, I_0 = 0.016 W and α ~0.01~0.02, the system responsivity will be about 9~18V/psi, theoretically. If R=0.2, Λ=4.54, the system responsivity will be increased to 40.86~81.72V/psi. The pressure resolution of the sensor system is

$$P_{res} = \frac{V_{noise}}{\delta_{sys}} = \frac{\lambda_c \cdot h^3 \cdot V_{noise}}{1.368 \cdot 10^{-7} \cdot \pi \cdot \Re \cdot G \cdot R \cdot A \cdot I_0 \cdot a^4} \tag{2-42}$$

Obviously, to get higher pressure detection resolution, we need to reduce the system noise. From the above equations, it is seen that the resolution of the sensor can be designed to fit different application requirements either by adjusting the source, the detector, or the amplifier or by changing the geometric parameters of the sensor head with desired effective diaphragm size *r* and thickness *h*. In general, a diaphragm with a larger radius and a smaller thickness will render more sensitive detection of acoustic signals. However, as indicated above, the operating range of the sensor head needs to be limited within the linear range, which is a fraction of an interference fringe to avoid the sensitivity reduction and fringe direction ambiguity problems. This imposes a limitation on the thickness of the silica diaphragm.

Another issue in the design is the trade-off between sensitivity and frequency response. From Equations (2-14), (2-26) and (2-27), the higher the pressure sensitivity requirement, the thinner the diaphragm, which lowers the frequency response. Therefore, by changing the sensor size and the thickness of the diaphragm, sensors with different dynamic ranges and frequency response ranges can be designed for various requirements of acoustic emission detection.

Chapter 3. Fabrication of DOFIA Sensor Probe

In the preceding chapter, the fundamental theory of the diaphragm-based interferomitric sensor is addressed in terms of sensitivity and sensor frequency response. This chapter will focus on the practical design and fabrication of the optical sensor head, which is the most critical component in the sensor system.

3.1 Sensor Probe Practical Design Requirements

3.1.1 Special design requirements of DOFIA probes for PDs detection

To apply the diaphragm-based optical fiber acoustic sensor for PD detection, the sensor head should meet several special specifications as follows.

1) Proper frequency response range

   It has been reported that the PD pulse originates with a duration of at most a few nanoseconds (10^{-9}s). Due to the short signal duration, the frequency of PDs is distributed over a wide range. Attenuating materials, like pressboard in the transformer, generally attenuate high frequencies more. Therefore, the dominant acoustic emission by PDs is within the range of 30~300kHz.

2) High pressure sensitivity

   The acoustic pressure generated by a partial discharge is sometimes as weak as 1 Pa, which requires that the acoustic sensor for PD detection provide high pressure sensitivity. According to Chapter 2, two factors of sensor probes would improve the pressure sensitivity: a) choose thinner and wider diaphragm, and b) use medium-fineness interferometer, by increasing the reflectivity of interfaces. Since thinning and widening the diaphragm will narrow the sensor's frequency bandwidth, the second option is a better choice, which may permit the sufficient bandwidth, and sensitivity at the same time.

3) Temperature cross-sensitivity (Thermal stability)

Power transformers installed in the field should be able to withstand temperatures changing from –40 °C in winter to > 60°C in the sun-shining summer. This requires the partial discharges sensor in a transformer provide stable sensitivity in the whole temperature range. Accordingly, the thermal properties of the sensor have to be considered carefully to reduce the temperature-cross sensitivity. To achieve this purpose, two facts are important in the sensor practical design: 1) the materials' coefficient of temperature expansion (CTE) should be kept as small as possible; 2) the difference between materials' CTEs should be as small as possible. Since fused silica has a small CTE similar to that of silica fibers, we choose fused silica as the major material for key elements in the sensor head fabrication.

4) Sensor Reliability and Sensor Productivity

From the manufacturing point of view, the sensor designed should have high enough reliability for the hash environment in a power transformer, such as higher temperature, and immersion in the transformer oil. Meanwhile, the sensor structure should be easy to fabricate and have potential for mass production.

5) Sensor physical size

The size of optical head should be designed as small as possible mainly because of sensing directional sensitivity. For a fiber acoustic sensor configured as an interferometric cavity head, the directional sensitivity of the sensor is not isotropic when the sound wavelength is less than the diameter of the probe. The higher the acoustic frequency, the greater the effect of the incidence angle on the response. Acoustic phase velocity is computed from the wavelength of the oscillations at a given frequency (v=fx). In transformer oil, the velocity of PD-induced acoustic wave is about 1400m/s. For a frequency range of 100k-300kHz, the wavelength range is 5~14mm. Therefore, to ensure higher directional sensitivity, the size of the fiber sensor should be designed as small as possible.

3.1.2 Sensor Structure and Fabrication Requirements

From fabrication point of view, the DOFIA sensor probes should provide the following features:

1) The initial cavity length of the DOFIA probe needs to be adjusted to a certain optimal value so that the signal channel can output interference fringes with good enough fringe visibility.
2) The initial sensor operating point needs to be precisely adjusted to be close to the operating point. This allows the operating range of the sensor to cover the full linear portion of the interference fringe.
3) To achieve the best thermal stability, the diaphragm and the fiber must be permanently bonded together with a high mechanical strength.
4) The sensor fabrication process should be controlled, and have the potential for mass production with good reproducibility and low cost.
5) The sensor probe needs to be properly packaged, sealed and protected so that the sensor can be easily handled, and mounted in the liquid environment.

3.2 Sensor Fabrication System Configuration and Assembly Processing Steps

The basic structure of a DOFIA sensor probe consists of a diaphragm, a lead-in fiber, and a fiber housing ferrule/tube, as shown in Figure 3.1. As addressed above, the pressure sensor head should be fabricated by bonding the silica fiber, the ferrule, the tube and the diaphragm together to form an interferometer with a sealed cavity. Technically, there are several challenges in the fabrication, in order to get a good acoustic sensor with required sensitivity and frequency response:

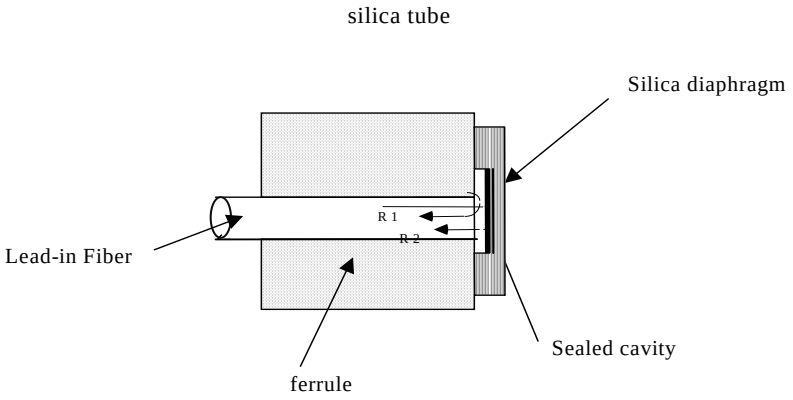

Figure 3.1 Basic structure of DOFIA sensor probe

(1) The material and suitable bonding methods determine the performance of a sensor. To achieve high temperature stability, solid bonding is necessary.

(2) The mechanical support system for bonding should provide enough stability, repeatability and accurate control for every component of the sensor head.

(3) The cavity length control and monitoring system is important during sensor fabrication.

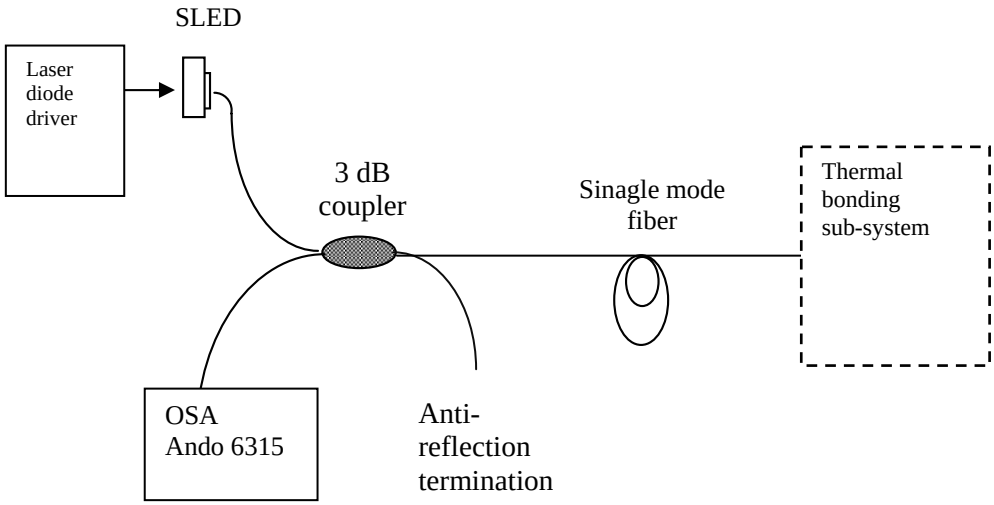

Figure 3.2 Schematic of DOFIA sensor probe fabrication system

As shown in Figure 3.2, the basic DOFIA sensor probe fabrication system includes two separate sub-systems: 1) the cavity length monitoring sub-system, and 2) sensor bonding

sub-system, which is further divided into heating/curing system and mechanical support system.

As illustrated in Figure 3.3, the main processing steps of the sensor head fabrication include component preparation, sensor assembly and sensor performance pre-test. For different design requirements, the preparation of components, especially diaphragm processing, is very critical to the final sensor performance. Sensor assembling is defined as the process of physically connecting all the components to form a real acoustic sensor with expected performance. Such an assembling process involves two major bonding interfaces: (1) fiber bonding in the fiber ferrule/tube; (2) diaphragm bonding on the ferrule to form a sealed FP cavity. Several sensor assembling methods have been developed. Assembled Sensor heads are then evaluated in terms of thermal properties and hydro-pressure sensitivity before going to a real PDs test, which will be presented in later chapters.

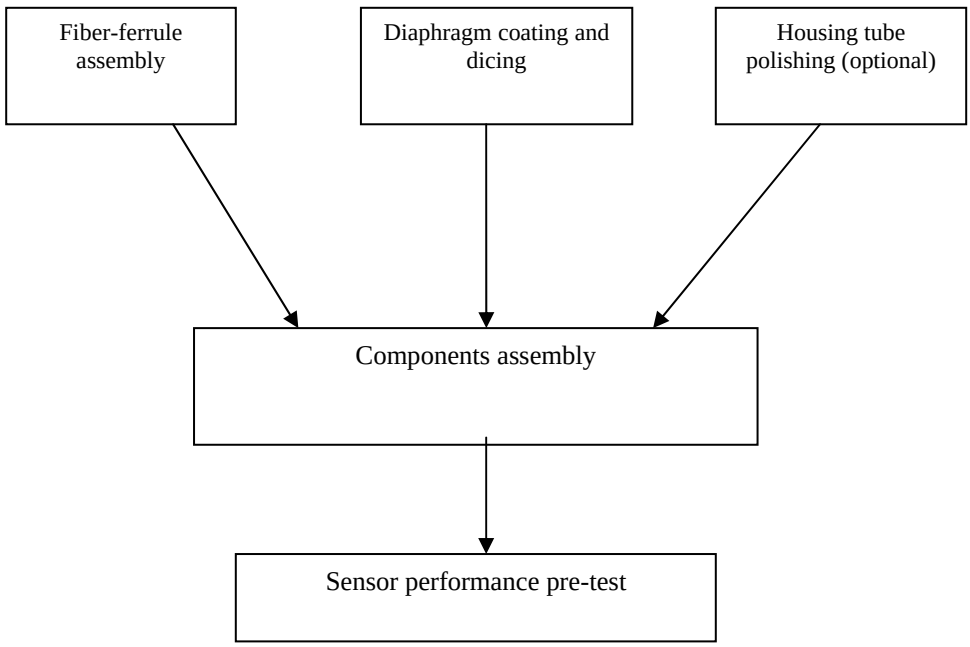

Figure 3.3 Sensor head fabrication process diagram

3.3 Sensor Materials and Components

In the proposed acoustic sensor, the diaphragm works as the key sensing element. In the low-fineness interferometer case, a blank thin fused silica plate is simply utilized. This kind of sensor is limited in the sensitivity due to the low reflectivity of the diaphragm interface(~4%). In order to achieve higher sensitivity, the diaphragm can be coated with dielectric or metal layers for a higher reflectivity.

On the other hand, to control the cavity length of the sensor precisely, a very straight forward method is to make a micro-cave in the diaphragm with a fix depth (*d*). This kind of cave should have desired span (*S=2a*) and provide desired reflectance (*R*) on the bottom, shown as in Figure 3.4. This kind of diaphragm is called Micro-Caved Diaphragm (MCD).

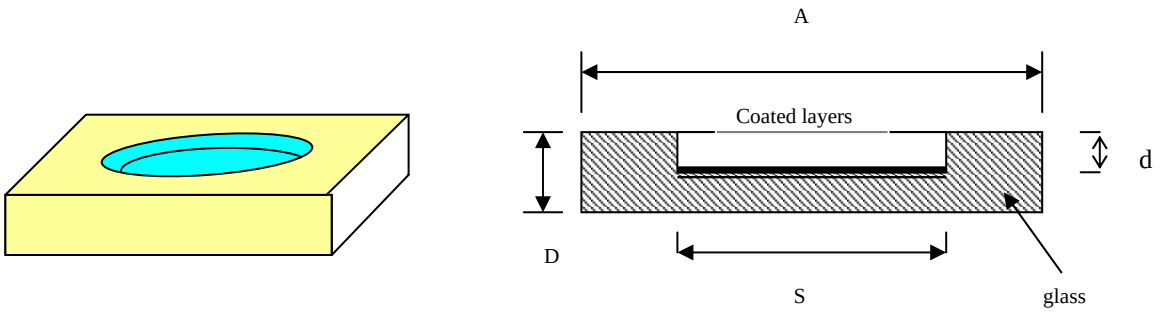

Figure 3.4 Micro-caved diaphragm

It's not easy to get a cavity in micron scale using standard mechanical methods. Benefiting from the Micro Electro Mechanical System (MEMS) technology, we applied standard IC processing technologies for manufacturing our sensor diaphragms, including photolithography, dry/wet etching, and metal evaporating deposition. This method provides higher process control capability for sensor fabrication, in terms of pre-cavity depth, coated reflectance, and yield.

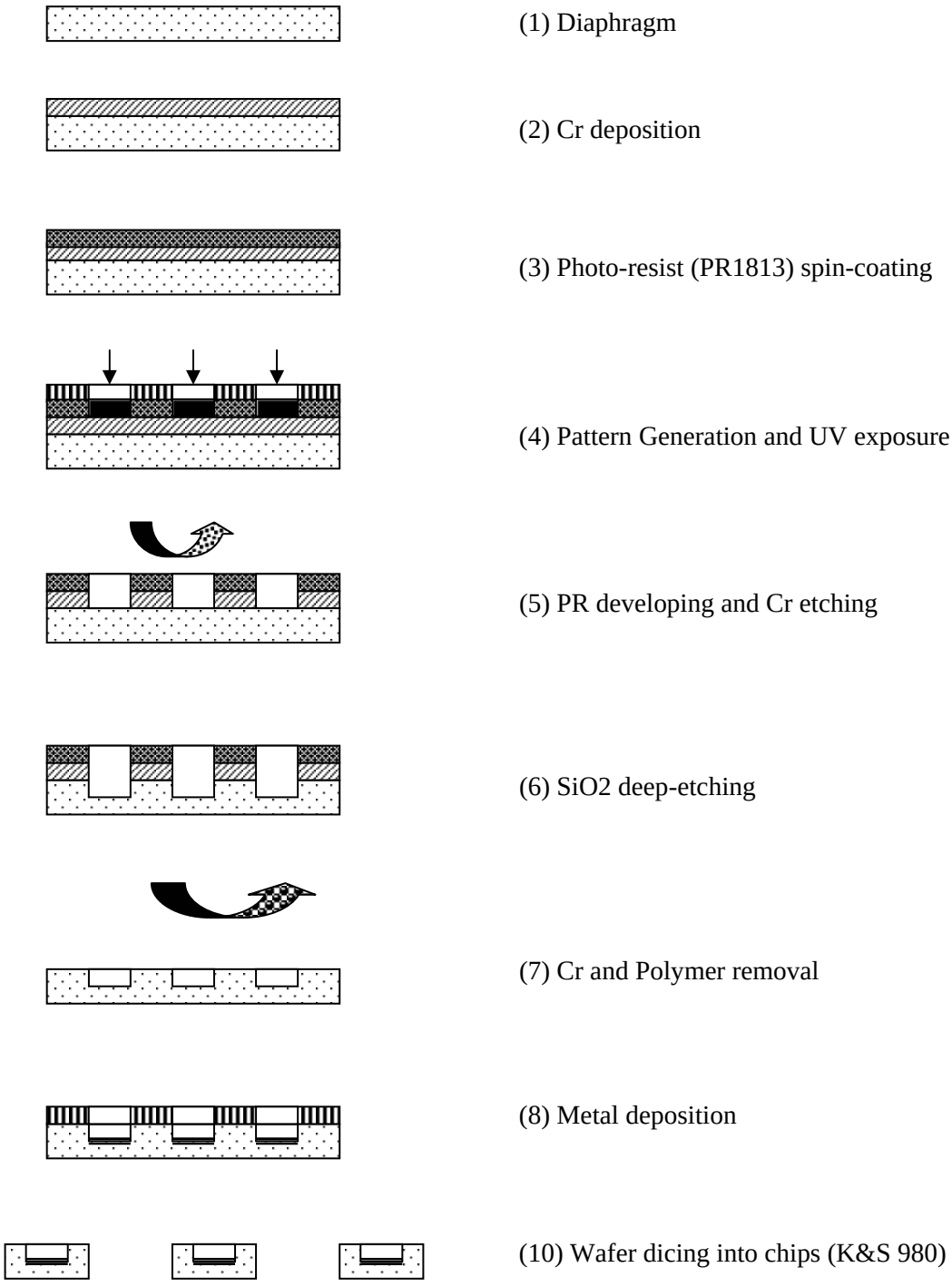

Figure 3.5 Schematic of the fabrication procedure of MCDs

Reactive ion etching (RIE) is one of the key techniques for MCD fabrication. RIE is a standard dry etching method in the very large scale intergration (VLSI) area, which combines physical etching mechanism (e.g. sputtering or ion milling) with chemical basis mechanism (e.g. plasma etching). Comparing to wet etching methods (for example, HF acid etching), RIE is able to reproduce the desired features with fidelity in terms of slope of side-wall, degree of undercutting, and etching depth as well [49,50].

Figure 3.5 shows a schematic of fabrication procedure of MCDs for acoustic sensors, which includes several main steps: 1) hard mask deposition; 2) photo-lithography; 3) RIE deep-etching; and 4) metal deposition of reflectance layers.

The first step is to build a suitable etching mask that will configure the feature of the micro cave, so this step is also called pattern generation. Chromium (Cr) is usually chosen as the hard mask for etching due to its high etching selectivity to SiO_2. Using electric beam evaporation method (TEMESCAL-FC-1800), 100nm-thick chromium (Cr) is deposited on the start wafer (fused silica wafer, thickness 100μm or less). Then, about 2μm-thick photo-resist (Shipley S1813) layer is spun on the Cr layer through a spin-coater (HEADWAY RESEARCH PWM32).

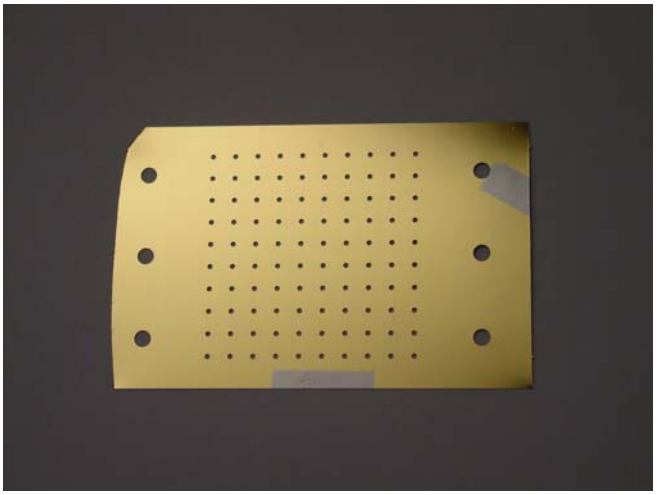

Fig 3.6 A photo-mask with 1.5mm hole array

In the step of photo-lithography, a stainless plate was fabricated with holes array in advance, and then is used as the exposure mask to generate the desired pattern. Figure 3.6

shows a mask with 1.5mm diameter holes. During UV exposure, a contact alignner with a UV source (ABM aligner) is used. The UV wavelength is 360nm and exposure time is 30sec. After PR developing (MP32, ~1min developing time) and Cr etching (chromium etchant CR-7), the Cr mask is formed on the diaphragm.

RIE deep-etch is produced in the SLR-720 RIE with gas compositions O_2/CF_4 at chamber pressure=4.0mTorr and power=100W. Under that condition, the etching rate for SiO_2 is about 15nm/min, and Cr/SiO etching selectivity is better than 20:1. Therefore, the depth of the cavity can be controlled precisely. The possible etching reactions include:

$e + CF_4 \rightarrow CF_3^+ + F + 2e$ (CF2 +F)

$e + CF_4 \rightarrow CF_3 + F + e$

$O + CF_3 \rightarrow COF_2 + F \rightarrow CO + F + F_2$

$SiO_2 + 2F \rightarrow SiF_2 + O_2$

$SiO_2 + 3F \rightarrow SiF_3 + O_2$

$SiO_2 + 4F \rightarrow SiF_4 + O_2$

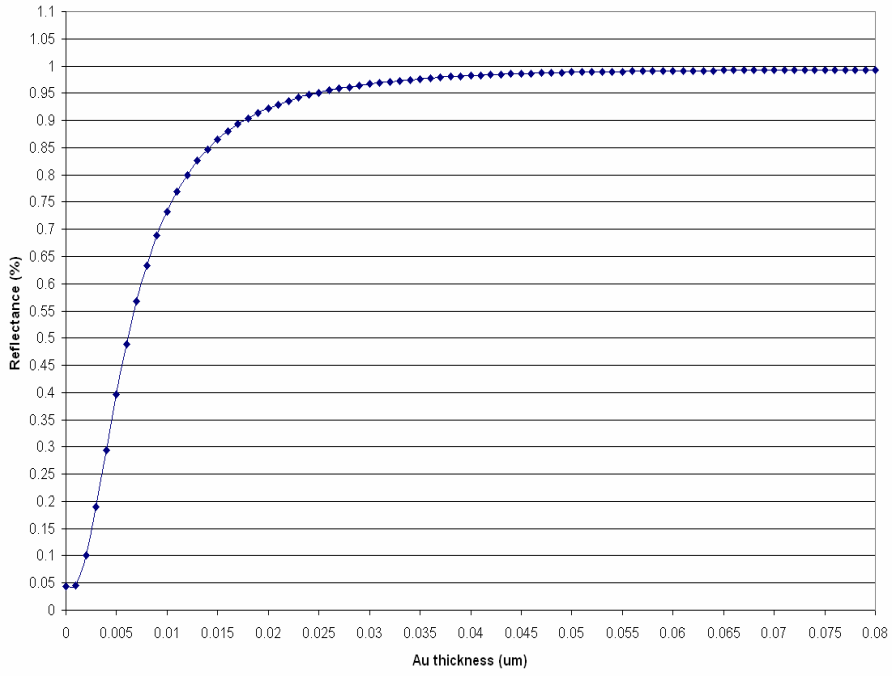

Figure 3.7 Reflectance of Au film versus Au thickness

After the deep etching to the desired depth, the caved diaphragm wafer is merged in the chromium etchant (CR-7) to remove the Cr residual. Then the O_2 plasma cleaning method is applied to clean the polymer residual. In the step of metalization, titanium (Ti) and gold (Au) are deposited for the reflectance layer, because of their stable properties at high temperature (>1000 °C). Among them, Ti works as adhesion layer due to the poor adhesion between Au and SiO_2 surface. The curves shown in Figure 3.7 indicate the reflectance as function of Au thickness. For example, 50nm thick Au-layer provides ~99.2% reflectivity. Finally, the coated MCD are diced into the desired size, usually, 2x2mm, or 3x3mm, which is determined by the size of supporting ferrule/tubing. In Figure 3.8 (a), the Scanning Electrical Microscopy (SEM) picture of the finished MCD shows the depth of the cave is 2.01 um. Diced MCD chips are shown in Figure 3.8 (b).

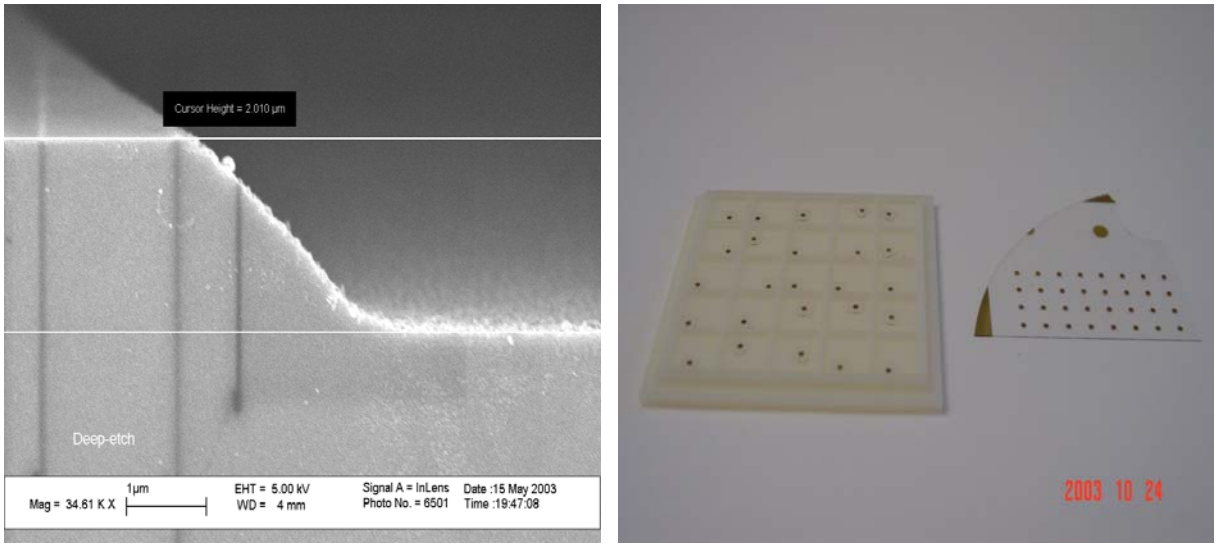

(a) (b)

Figure 3.8 (a) SEM picture of MCD and (b) photograph of diced MCD chips

Besides the diaphragm, the fiber, the ferrule and the housing tube are also important elements for the sensor head. Table 3.1 illustrates the basic parameters for the sensor fabrication.

Table 3.1 Basic components and materials for DOFIA sensor probe

Components	**Material**	**Functions**	**Dimension**	**Vendors**
1) Diaphragm	Fused silica	Sensing elements	50, 100 , 200um thick	E&C Inc.
2) Fiber	Fused silica	Light leading	9/125 single-mode	Corning Corp.
3) Ferrule	Fused silica	Fiber housing	127um IDx1990(or 2500)um OD	PG Inc.
4) Outside Tubing	Fused silica	Sensor supporting	2000um ID x 4500um OD	PG Inc.
5) Inter-media layer	Borasilicate	Adhesion layers	Grains with size<5 um	Corning Corp.

3.4 Development of Sensor Bonding Methods

Three major bonding methods have been proposed and developed, which are epoxy/solder bonding, inter-medium layer thermal bonding and CO_2 laser thermal bonding [51-54].

3.4.1 Epoxy bonding method

Epoxy is a commonly used bonding material in micro-system packaging. At the earlier project stage, several epoxies, such as Epoxy 907 Adhesion System, were used to bond the fiber, ferrule, tubing and diaphragm together. Figure 3.9 shows the supporting system used for the epoxy bonding method. In this bonding scheme, the ceramic ferrule with an inner diameter of 127 μm, often commercially used in fiber optical connectors, is used to hold standard single mode fiber (with 125μm cladding) by Epoxy 907. Silica tubing having a slightly larger inner diameter (2.54mm) than the outer diameter (2.5mm) of the ferrule, is chosen to support the fused silica diaphragm. Usually, the ferrule with the fiber bonded to it is prepared at first, then the tubing, the ferrule and the diaphragm are bonded together using the epoxy at the same time. During the solidifying period of the epoxy, the air gap between the fiber end-face and the diaphragm inner surface can be slightly adjusted by two X-Y-Z translation stages to the initial operating point. Figure3.10 shows sensors fabricated using the epoxy bonding method.

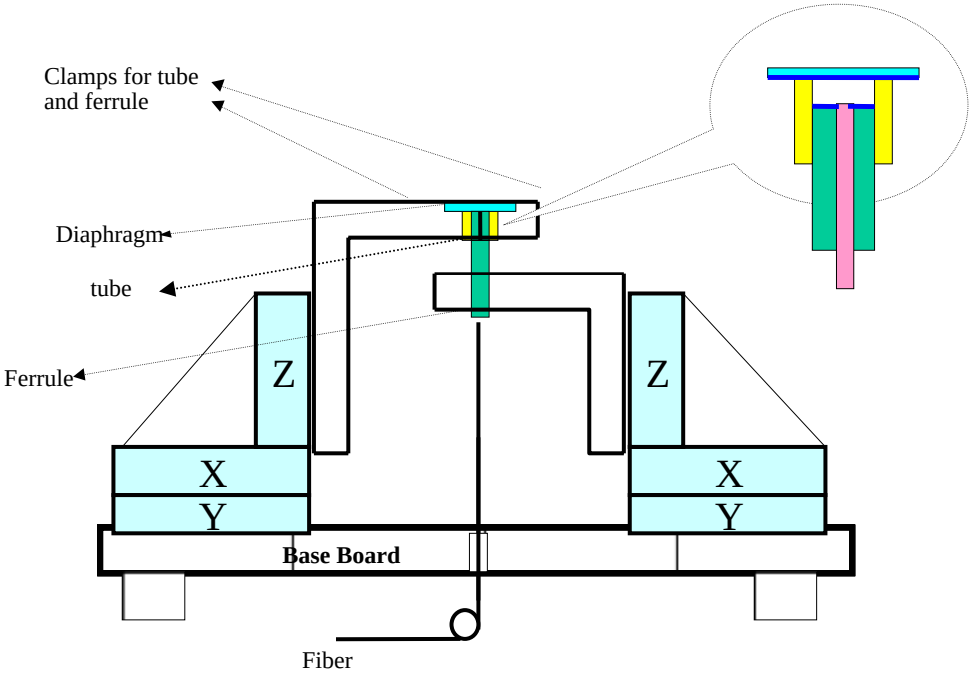

Figure 3.9 Supporting system for epoxy bonding and solder bonding

Figure 3.10. From the left: Epoxied sensor, silica hollow core, another sensor, a single ferrule, and diaphragm chip

3.4.2 Inter-medium layer thermal bonding method

Instead of using soft materials such as Epoxy, if we can bond the sensor by some solid inter-medium layer materials that match the thermal properties of the fused silica, the sensor is expected to have better mechanical strength and temperature stability. To achieve this, the bonding should be done at higher temperatures. Therefore, a thermal bonding method with the use of a inter-medium layer material was proposed and investigated.

We managed to use a glass material instead of epoxy as an inter-medium layer between the diaphragm and the tubing, the tubing and the ferrule,. The mainly-used glass is borasilica with a softening point ~600 °C, which is lower than that of fused silica (1400 °C), but much higher than regular epoxies and solders. When all these elements are heated up to the softening point of the borasilica in a furnace, the tubing, diaphragm, ferrule and fiber will be bonded together through the inter-medium layer among them, and a sealed cavity will be formed. With the glass inter-medium layer, the sensor working temperature would be raised up to 600 °C.

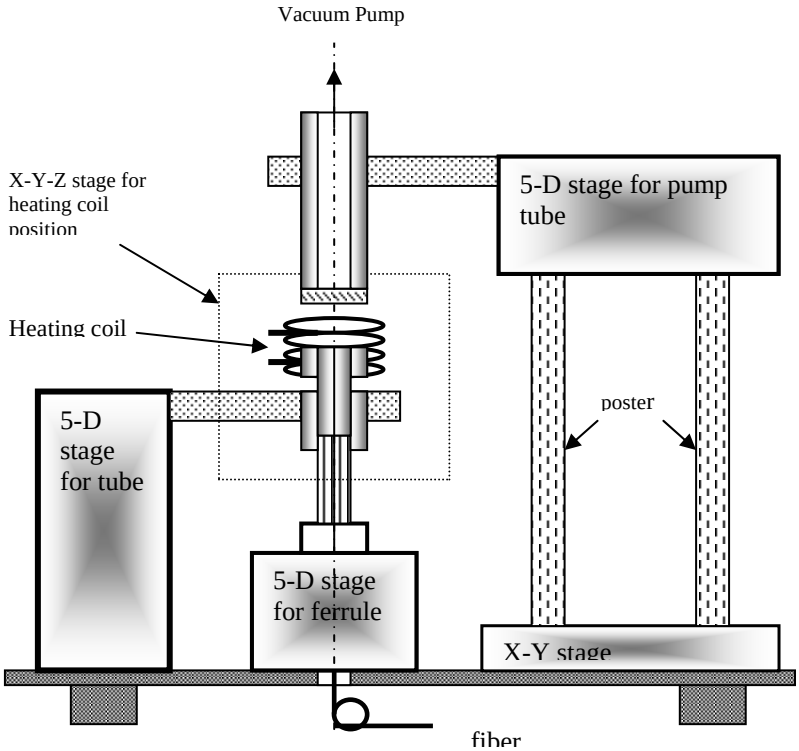

Figure3.11 Schematic support system for Inter-medium layer bonding method

Figure 3.11 shows a thermal bonding supporting system for the fabrication of DOFIA sensor probes. In this scheme, The ferrule, fiber, tubing and diaphragm are bonded using bora-silica powders (powder size < 5um). The diaphragm is handled and moved by a vacuum arm made of a silica tubing. A special heater is made of heating wires (Kanthal Inc.), which can reach 1200 °C. The size of the heater is shortened to 1cm in diameter and 1 cm in length so that the air gap change due to the thermal expansion of each component during bonding process can be reduced. Four 5-axis precise stages are used for controlling the positions of the ferrule, tubing, diaphragm and heater, respectively. The photograph of this supporting system is shown in Figure 3.12.

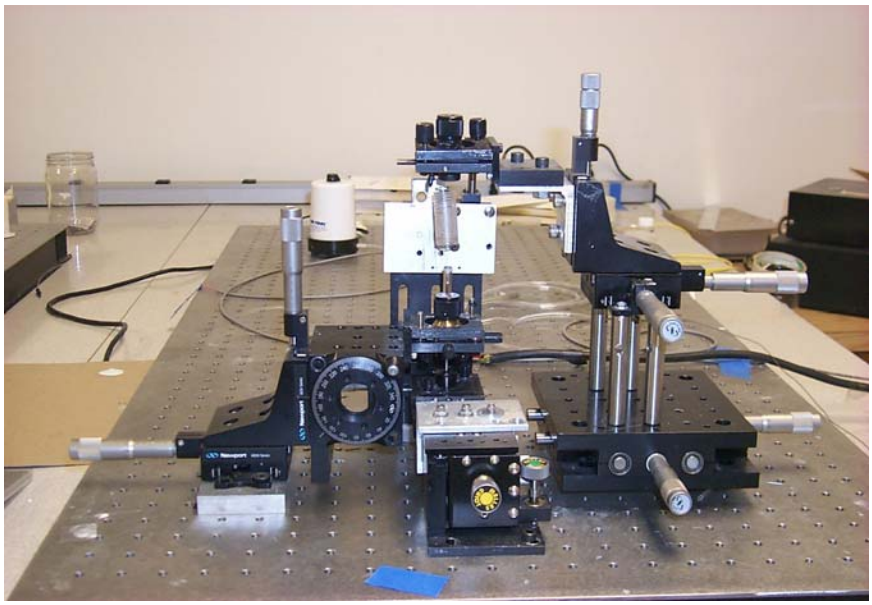

Figure3.12 Modified inter-medium layer thermal bonding system

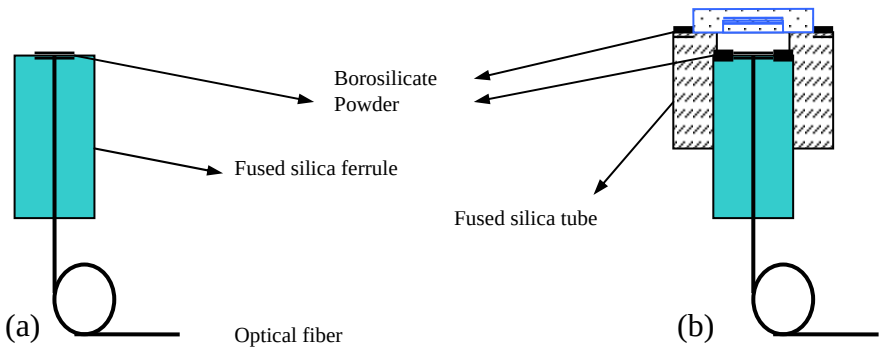

Figure 3.13 Controlled thermal bonding method to fabricate PD sensors

The main fabrication process includes two major steps as explained in Figure 3.13. First, a single-mode fiber was carefully cleaned, cleaved, and inserted into the polished quartz ferrule under an optical microscope. Then a layer of borosilicate powders is applied on the top of the ferrule, and the single-mode fiber is bonded with the quartz ferrule at high temperature. After being bonded, the end of the fiber is carefully polished. At the second stage, the ferrule module is inserted through the supporting tubing with end-face polished. Carefully inject powders at the joining edge of the ferrule and inner surface of tubing. A MCD chip is put on the polished end of the tubing with boracilicate powders surrounding the edge of the MCD chip. Move the heater to surround the whole module, and heat up to desired temperature. Every thermal heating step is finished in the heater at ~850 °C. To avoid inner thermal stresses which will break the glass assembly, the heat process is divided into preheating (~5 min), heating (~850 °C ~10min), and annealing time (~30min), as illustrated in Figure 3.14. The air gap between the fiber and the inner surface of the silica diaphragm is adjusted to give the highest interference fringe visibility during the thermal process.

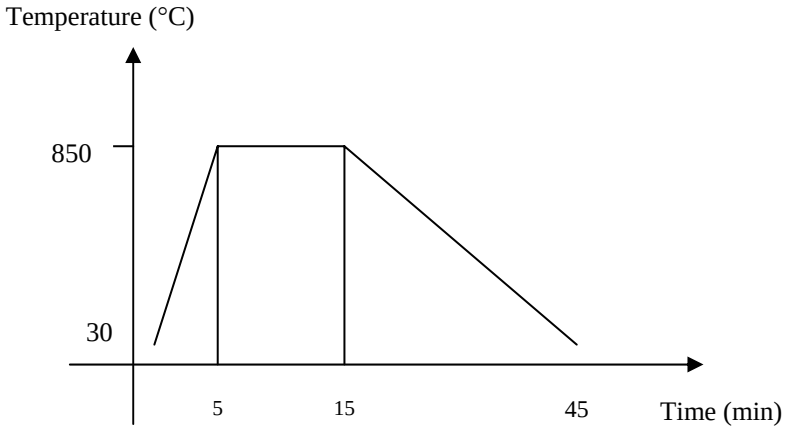

Figure3.14 Heating process of thermal bonding

The photograph of three DOFIA sensor probes fabricated by this method is shown in Figure 3.15. The sensor size is determined by the outside tubing, which typically is 4.5mm in diameter and ~6-8mm in length.

Figure 3.15 Photograph of three diaphragm-based sensor probes fabricated by inter-medium layer thermal bonding method

3.4.3 Direct thermal bonding using CO_2 laser technology

3.4.3.1 CO_2 laser sensor bonding system configuration

Theoretically, an ideal solid sensor should be composed of the same material (fused silica in our sensor), and bonded directly without any inter-media layer material. A direct bonding method is developed mainly based on utilizing a CO_2 laser sensor bonding system available in CPT. As shown in Figure 3.16, the CO_2 laser (SYNRAD, Inc. Model 48-2) has the wavelength 10.6 μm and the maximum output power 25W. At the typical wavelength 10.6 μm, silica glass materials have a high absorption coefficient, and the CO_2 laser power will be transformed into heat. This will raise the temperature and eventually reaches the softening/melting point of the materials in a short time period. Based on this principle, two glass materials can be heated locally and melted together to form solid thermal bonding. Obviously, the utilization of a CO_2 laser in the bonding will potentially provide precise temperature control as well as small and localized bonding points, which are important in the sensor fabrication. Actually, the CO_2 laser system has been successfully used to fabricate tubing-based SCIIB sensors for a while in CPT

[55,56,57]. By modifying the bonding supporting system, we have also successfully applied this method to fabricate diaphragm-based acoustic sensors.

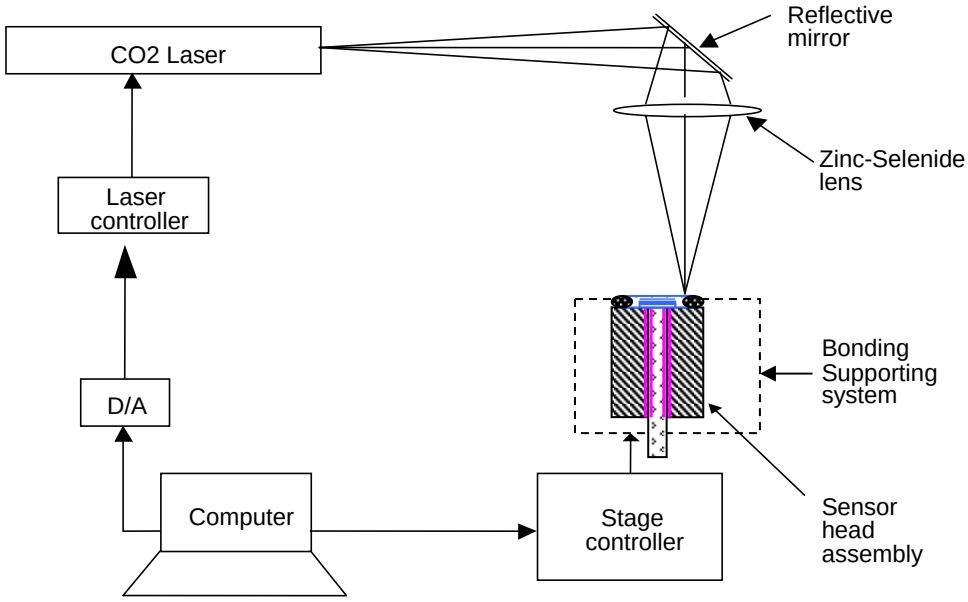

Figure 3.16 System setup diagram for CO_2 thermal Bonding

The original beam diameter of the laser output is 3.5mm. After a cylindrical ZnSe lens with a focal length of 5 inches, a laser spot with the line width of 100 μm and the length of 3.5mm is obtained at the focus point. The laser controller has a pulse gate and an analog voltage input. A computer D/A board was designed (by Ming Luo, Wei Huo and Hai Xiao[55]) to enable precise control of output power and lasing time.

3.4.3.2 Sensor bonding procedure

Figure 3.17 briefly describes the procedures of the sensor bonding using the CO_2 laser bonding approach, including fiber-ferrule bonding, ferrule polishing and MCD-ferrule bonding. At the first step of ferrule-fiber bonding, the Filmtronics Silicate Spin-on Glass (SOG) P104F is used as the inter medium material to bond the ferrule and the fiber. Spin-on Glass (SOG) is liquid solution which, upon curing at certain temperature (<500 °C), forms solid SiO_2 layer with melting point ~900°C. SOG is usually used as an interlevel dielectric material that is applied to a silicon wafer to fill narrow spaces in the

pre-metal and metal levels while planarizing the surfaces. In the fiber-ferrule bonding, since the gap between the fiber and inner-face of ferrule is less than 5 μm, SOG is an ideal material to fill this gap and form solid bonding at the same time.

(1) Fiber cleaving and insertion in the ferrule

(2) SOG filling and fiber-ferrule bonding

(3) Fiber end-face polishing

(4) MCD bonding on the ferrule

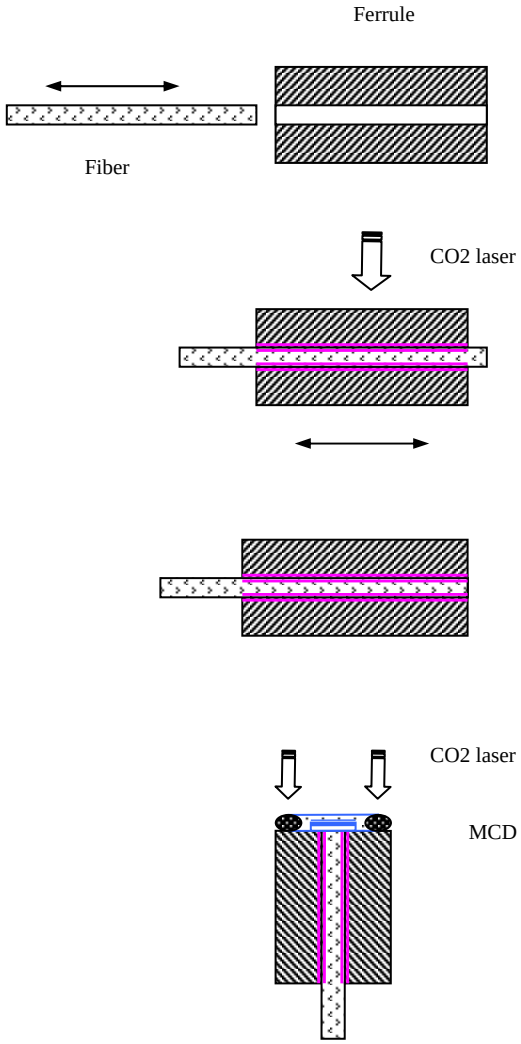

Figure 3.17 Sensor fabrication procedure using CO_2 laser direct bonding approach

As shown in Figure 3.17, the fiber is inserted into the ferrule under an optical microscope first. SOG is then filled into the gap between the fiber and ferrule. The fiber and ferrule assembly is positioned in the CO_2 laser path with desired laser power, usually at or near the focus point. The laser shines the ferrule laterally. To make the light exposure on the ferrule assembly more uniform and symmetrical, two copper mirrors are used to fold partial light beam back to the ferrule, as shown in Figure 3.18 (a) and (b). Since SOG is

supposed to be cured through several temperature steps, the laser power and exposure time should be controlled to achieve required optimal values for the best bonding.

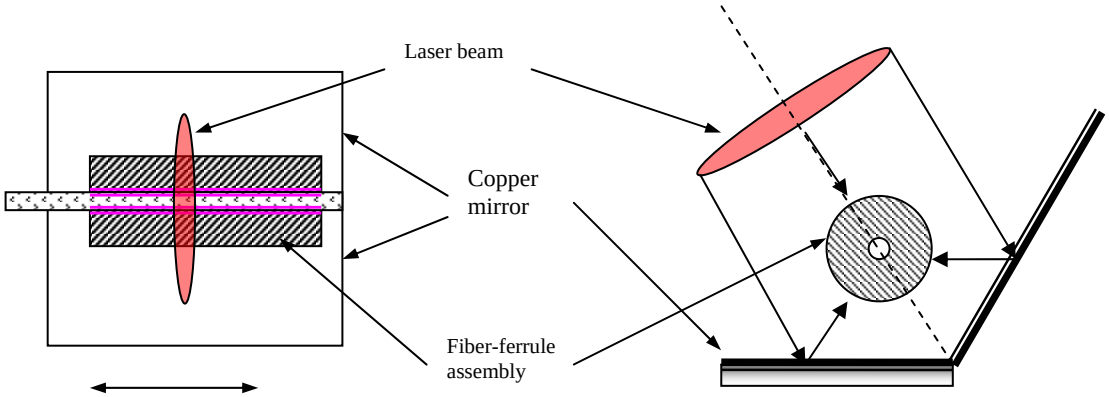

(a) (b)

Figure 3.18 Laser beam path surrounding the fiber-ferrule assembly

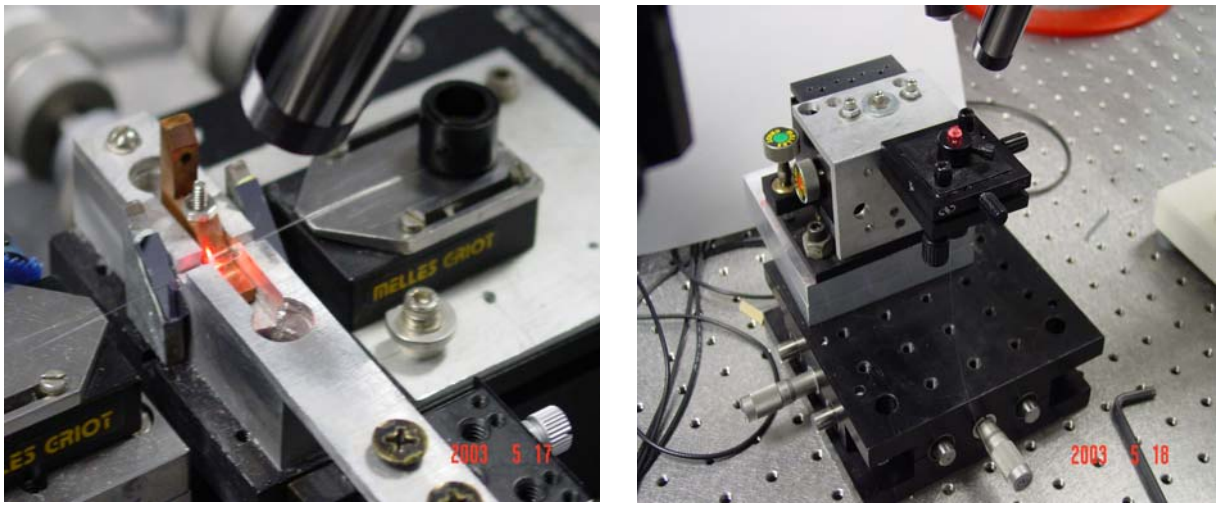

(a) (b)

Figure 3.19 Photograph of stage system for direct laser bonding methods
(a) stage and mirror system for fiber-ferrule bonding, (b) stage for ferrule-MCD bonding

The fiber-ferrule assembly is polished carefully after bonding so as to reach good surface reflectivity. At the step of ferrule-MCD bonding, a MCD chip is put on the top of fiber–

ferrule assembly and positioned in the laser beam path again. To bonding the diaphragm on the ferrule, the edges of the MCD chip are directly exposed to the laser from the top, instead of laterally. In this case, the mirror system is not applied. Figure 3.19 (b) shows the photograph of the stage system for the MCD bonding. To release the inner thermal stresses generated during the laser exposure, which may break the glass component, the laser power and exposure time is optimized and divided into preheating (~2 sec), heating and holding (~4W and ~3 sec), and ~20sec of annealing time, as illustrated in Figure 3.20.

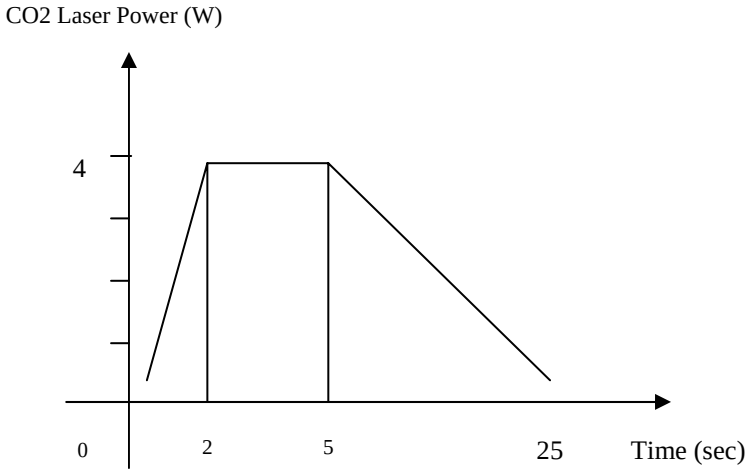

Figure 3.20 Laser heating curve for MCD sensor bonding

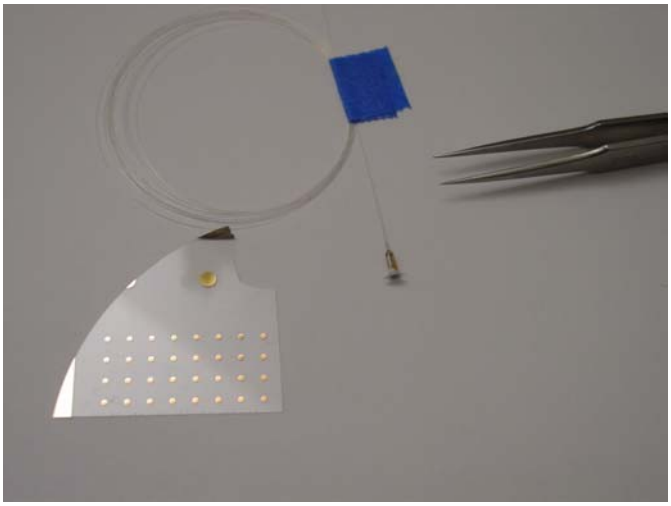

Figure 3.21 Sensor fabricated by CO_2 laser bonding method

Figure 3.21 shows a sensor made by the direct bonding method. The diameter of the sensor is 2.5mm, and the sensor head length is about 7mm, which is much smaller than sensors fabricated by the previous methods.

3.4.4 Comparison of different bonding methods

The main characteristics of each of three sensor bonding technologies are summarized in Table 3.2. The Epoxy bonding approach is a straight-forward method with relatively simple bonding procedures. However, the epoxy can only work at low temperature due to its lower softening point (usually less than 300 $^{\circ}$C). The sensor made by this method is thus limited for low operating temperature. Moreover, the epoxy has completely different coefficients of thermal expansion and Young's modulus from that of the fused silica components in the sensor, which also limits sensor's frequency response and temperature stability.

The sensors fabricated by thermal bonding method have similar size to that of the Epoxy bonded sensors, which is limited by the supporting outside tubing. But benefiting from the glass inter-medium layer, the thermal bonding sensor has better temperature independence performance, and solid frequency response. Since all the components of the sensor are connected in high temperature, it is not easy to control the bonding process precisely, which causes poor fabrication controllability in terms of cavity length, gauge length and yield.

The state of development on the CO_2 laser direct bonding method is less than that of Epoxy and inter-medium layer thermal bonding methods. This method already shows potential advantages in terms of sensor size, and cavity length controllability, since 1) the cavity/gauge length of sensors is directly determined by the cavity depth of MCD; 2) all of the sensor bonding processes are performed at room temperature. Sensors made by this method have similar or better performance in temperature independence performance, and frequency response. Obviously, this method has great potential for mass production of sensors once the supporting stage systems are improved.

3.5 White-light Interferometric Sensor Cavity Length Monitoring Sub-system

As described in Eq. (2-6), the interferometer intensity is a function of wavelength. Assuming a given light source with FWHM=50nm as shown in Figure 3.22(a), Figure 3.22(b) illustrates the interferometer spectrum of a sensor with cavity gap 20 μm, while Figure 3.22(c) shows the normallized spectrum of Figure 3.22(b).

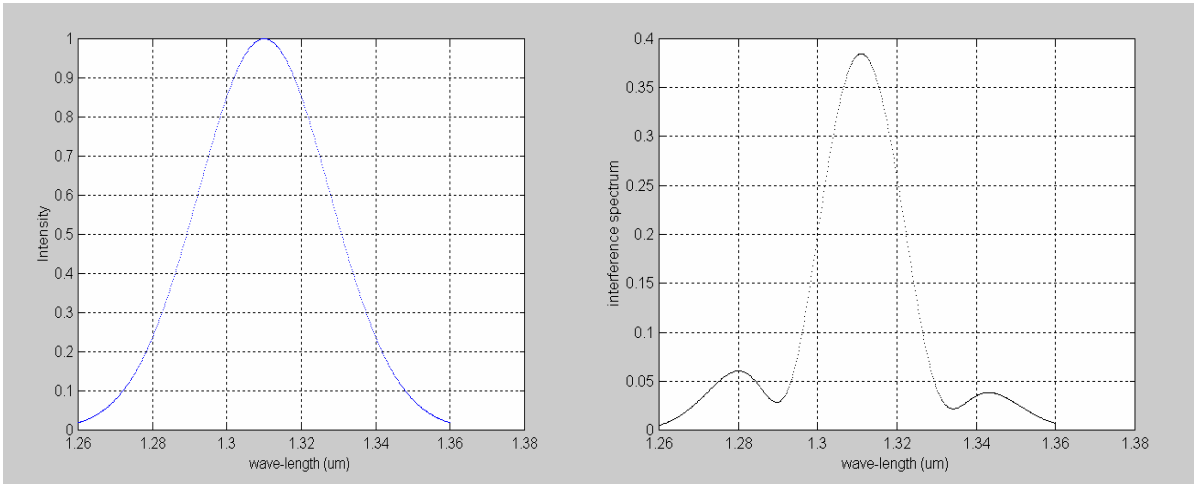

(a) (b)

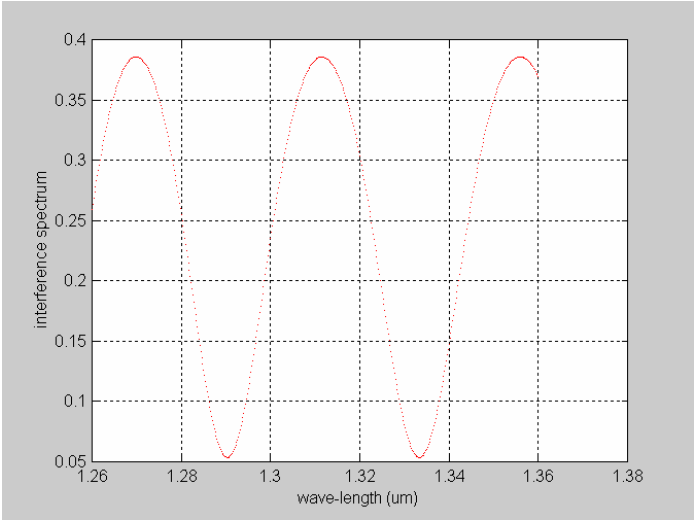

(c)

Figure 3.22 (a) Light source with band-width 50nm, (b) Sensor spectrum (L=20um, and R=20%), (c) Normalized sensor spectrum

Considering two wavelength components (λ_1 and λ_2) in the spectrum, they cause different phase ($\phi_{1,2}$), which can be expressed as:

$$\phi_{1,2} = \frac{4\pi L}{\lambda_{1,2}} + \phi_0 \tag{3-1}$$

Then the phase difference is given by

$$\Delta\phi = \phi_2 - \phi_1 = \frac{4\pi L(\lambda_2 - \lambda_1)}{\lambda_1\lambda_2} \tag{3-2}$$

We have

$$L = \frac{\Delta\phi\lambda_1\lambda_2}{4\pi(\lambda_2 - \lambda_1)} \tag{3-3}$$

If the phase difference of these two spectral components are known, the absolute value of the cavity length L can be calculated by Eq. (3-3).

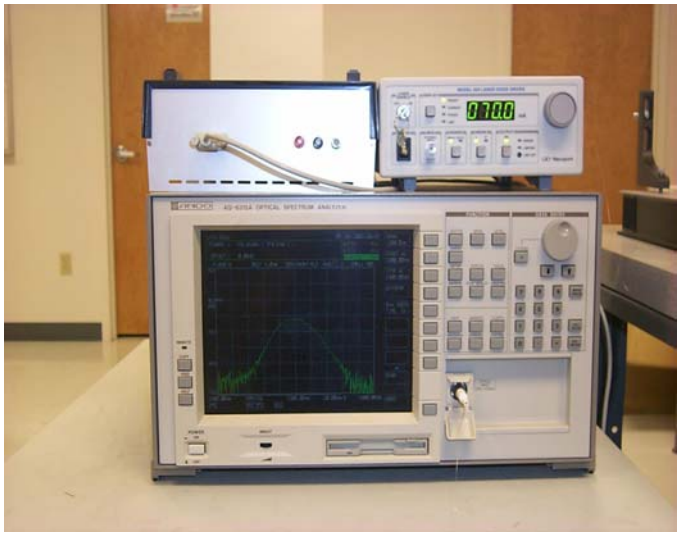

Figure 3.23 Photography of white-light cavity length monitoring system

Based on this principle, a white-light cavity length monitoring system has been set up for medium-fineness interferometric sensors, as illustrated in Figure 3.1 and Figure 3.23. This system is based on a broad-band source (1310nm LED) and an optical spectrum analyzer (OSA, Ando 6315), instead of a fiber optic PC plug-in spectrometer (PC2000 manufactured by Ocean Optics, Inc.) which is used for low-fineness sensors [57,58,59].

Figure 3.24 shows the typical interference spectrum of a sensor with medium-fineness, which has air-gap 30.980um and visibility ~60%.

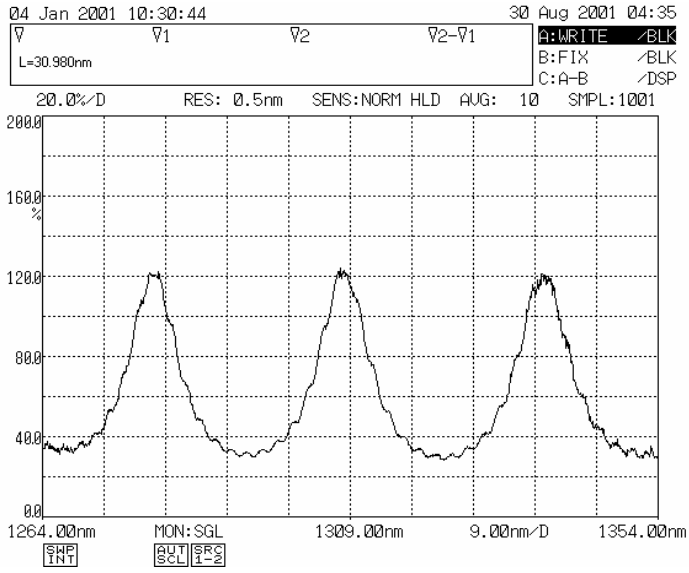

Figure 3.24 Typical interference spectrum of medium fineness sensor

Table 3.2 Comparison of difference sensor bonding methods

Sensor bonding method	Sensor Size	Cavity range (um)	Gauge length range (mm)	Cavity and gauge length controllability	Visibility controllability	Temperature cross sensitivity	Frequency response	Operating temperature	Reliability	Fabrication yield	Application
Epoxy	4~6mm(D)X 6-8mm (L)	>10	>1mm	poor	good	poor	poor	<200 C	poor	good	low temperature, low frequency response, high sensitivity
Inter-medium layer thermal bonding	4~6mm(D)X 6-8mm (L)	>5 um	>0.5mm	poor	poor	good	good	>600 C	good	poor	high temperature, high frequency response
Direct bonding	2~3mm(D)X 5~7mm (L)	>1um	<0.2mm	good	good	good	good	>800 C	good	poor, potential to improve	high temperature, high frequency response, high directional sensitivity

Chapter 4. Instrumentation of DOFIA Sensor System

This chapter will mainly describe the design and the implementation of the optoelectronic signal processing unit in the diaphragm-based acoustic sensor system.

4.1 DOFIA Sensor System Configuration

Figure 4.1 illustrates the schematic of the DOFIA sensor system. Besides the diaphragm-based sensor probes, another significant part in the system is the optoelectronic signal processing unit, which is framed with the dash lines. This unit consists of two main parts: light source and connection, and detectors and electronic amplifiers.

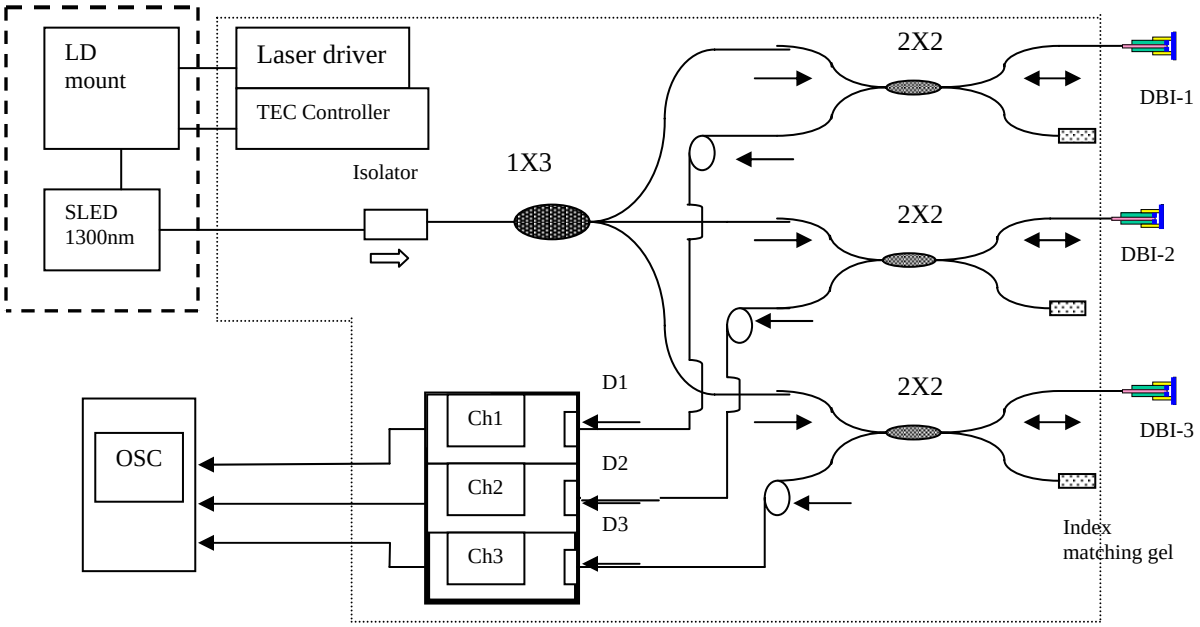

Figure 4.1 Schematics of the diaphragm-based OFAS sensor system

Instead of the distributed feedback laser (DFB) used before [60], the optical source in the improved sensor system is a superluminescent LED (SLED1300D20A, Optospeed corp.) centered at 1300 nm, with maximum power output of 20mW. The SLED is a low-coherence light source with a broad-band spectrum, as shown in Figure 4.2. It provides the advantages over DFB lasers in terms of stability of output, and insensitivity to

environment perturbations, which will be shown in the following chapter. The SLED source is mounted on the LD Mounts (ILX Lightwave, LDM-4980) and equipped with a temperature electrical controller (TEC, Wavelength Electronics, Inc., HTC-3000) to reduce the power/wavelength drift due to temperature fluctuations.

To reduce the optical back reflections back into the source, the output of the SLED is launched to an optical isolator (Thorlab Inc.) with isolation >60 dB @1310nm, and split into three channels through a 1X3 single mode optical fiber coupler (AC Photonics Inc.). For the purpose of location analysis in partial discharge detection, at least 3-channels of sensors are required. In each channel, a 2x2 single mode optical fiber coupler (AC Photonics Inc) serves as the bi-directional light guide to and from the sensor head. Only one arm of the coupler "output" side is used; and the other output arm is scattered into an index matching gel so that minimal light is reflected back. The remaining arm is connected to the photo-detector and signal processing electronics.

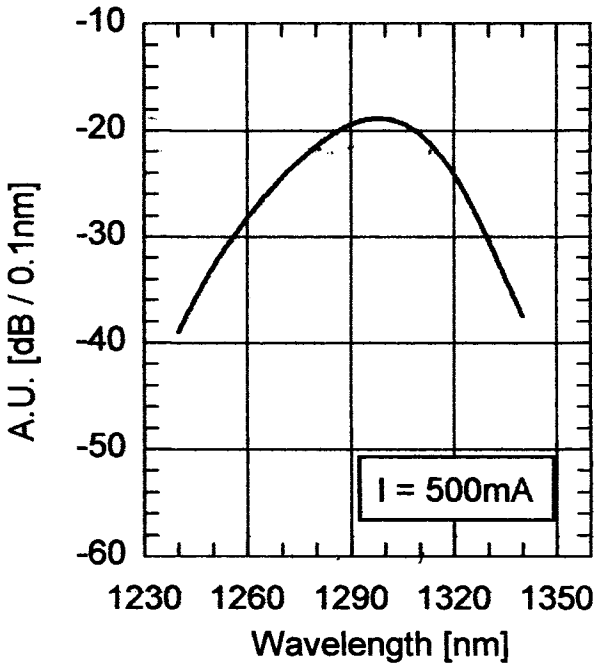

Figure 4. 2 Spontaneous emission spectrum of the SLED1300D20A

The exterior of the sensor system is shown in Figure 4.3 (a), where the SLED source mount sits on the signal processing box. Figure 4.3(b) illustrates the interior of the signal processing box. On the bottom layer, the power supplier, and three signal processing circuit units are located. The top layer serves as a fiber platform, where a 1x3 coupler, three 2x2 couplers and an isolator are accommodated. The power supplier can provide both ± 15V DC and +5V DC (for power indicator) output.

On the front panel, three BNC connectors are provided for oscilloscope monitoring, and three FC connectors and another three ST connectors are also provided to connect sensors. On the back panel, two 9-pin connectors are used for connecting signals to an A/D card and a laser driver input, respectively.

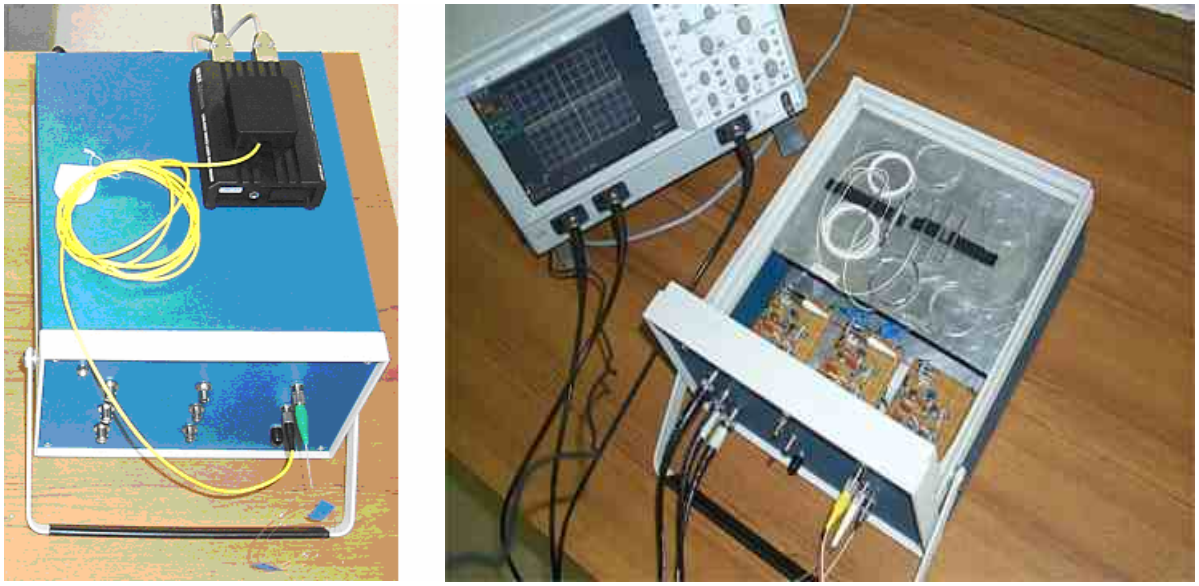

(a) (b)

Figure 4.3 Prototype of the signal processing unit for diaphragm-based fiber sensor system

4.2 Opto-electronic Circuits Design

One of the important parts in the DOFIA sensor instrumentation is the development of high-speed low-noise opto-electronic circuits for effective demodulation of the sensor signal with required frequency response and resolution. The performance of the sensor

system depends not only on the sensor structure design as we discussed in the previous chapter, but also on the output signal processing circuit. In the partial discharges detection, due to the fact that the magnetostriction-introduced noise of transformers usually exists in the low frequency range below 60kHz, and the acoustic emission frequency of PDs is mostly around 150kHz, the sensitive frequency of the sensor system is suggested to be within the range of 30kHz to 300 kHz. Moreover, fiber loss variations and laser power drifts, usually less than 100 Hz, could introduce errors to the amplitude of the interference signal and result in a poor accuracy of the measurement. These unwanted drifts can be eliminated by using an analog high pass filter in the signal processing unit. Therefore, the basic requirements for the signal processing unit for PD detection include:

(1) Frequency bandwidth (6dB): ~30 kHz – 300 kHz.
(2) Typical SNR in the bandwidth: > 55 dB.
(3) Gain: $>10^6$. The gain for each channel should also be adjustable to compensate for the non-uniformity of each sensor's response.
(4) Three channels to process the signals from three sensors simultaneously.

The signal processing circuits include three identical channels. Each channel is composed of a photo-detector, a current to voltage (I-V) converter, a gain-tunable amplifier and band-pass filters, as shown in Figure 4.4. The input is from a fiber sensor and the output can be monitored by an oscilloscope or directly connected to a data-capture-card. In the following sections, we will briefly introduce the design and function of each component used to fulfill the signal processing units.

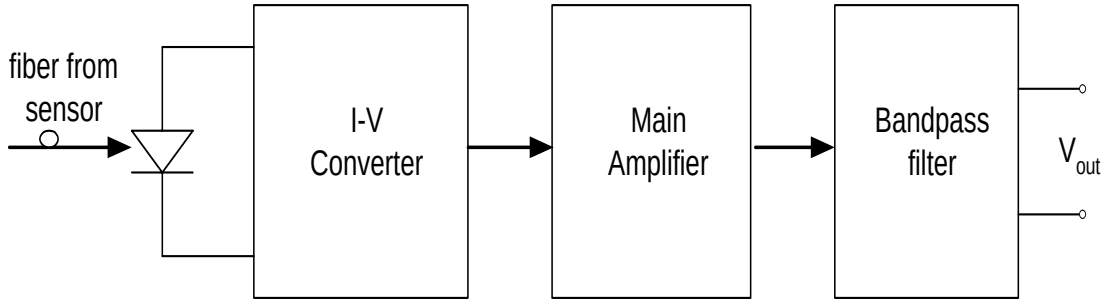

Figure 4.4. Schematic of one-channel signal processing circuits

4.2.1 Photo-detector and I-V Converter [61]

The detector used is FD150FC InGaAs photodiode. In the front-end, a transimpedance amplifier is used to fulfill current-voltage conversion. Transimpedance amplifiers are widely used in optical communication receivers because of their advantages of low noise, wide bandwidth and high stability. The key element is an operational amplifier (OP-37) manufactured by the Analog Device Corp due to its low noise, high speed, and low drift. A high-valued feedback resistor *R1* is clearly desirable from the noise point of view. Its value *R1* is determined by the minimum expected optical input power, detector conversion factor (A/W), dynamic range, and noise figure of the following amplifiers.

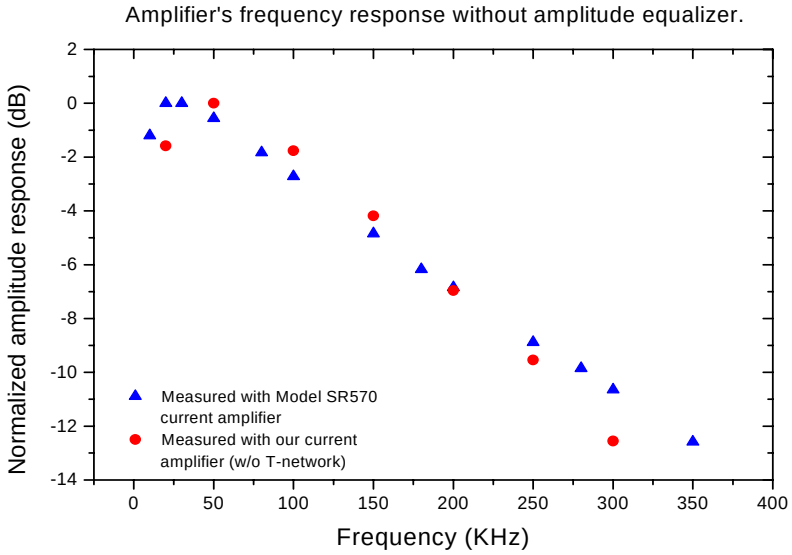

Figure 4.5 Roll-off phenomenon in current amplifiers without amplitude equalizer

However, because of the existence of the internal series resistance and junction capacitance of the photodiode, the frequency response of the I-V converter will roll-off with the increase of the signal frequency. Figure 4.5 shows the frequency response of two current amplifiers, including Agilent Model SR 570 current amplifier, and our current amplifier before any improvement.

Therefore, a T-network [62] is built in the feedback of the I-V converter for compensating the roll-off (Figure 4.6), where $f_P = 1/(2\pi R_1 C_1) \cong 80$kHz, $f_z = 1/(2\pi R_2 C_2) \cong 87$kHz, $f_b = 1/(2\pi R_3 C_2) \cong 330$kHz. The gain for I-V converter $G_{I\text{-}V}=R1=10^5$.

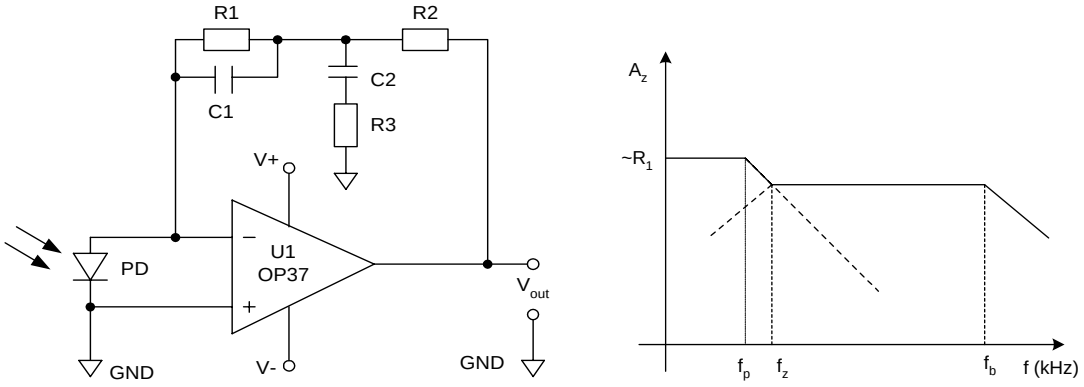

Figure 4.6 (a) Light detection and I/V converter. (b) Frequency response of T-feedback amplifier.

4.2.2 Gain-tunable amplifier

A gain-tunable amplifier, shown in Figure 4.7, is necessary in order to compensate for the non-uniformity of each sensor's response. This cannot be done by adjusting the gain of the current-voltage converter because I/V converter is more sensitive to the total noise of the system. The gain of the main amplifier $G_m = 1 + R_5/(R_4+W_1)$=33~23.

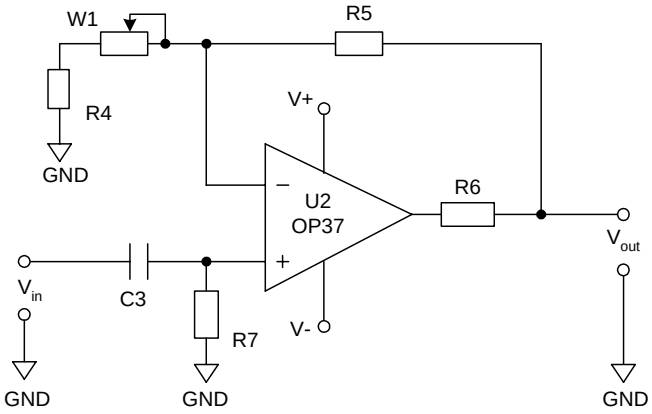

Figure4.7 Gain tunable main amplifier

4.2.3 Band-pass filter

The band-pass filter has a pass-band between two cutoff frequencies f_H and f_L ($f_H > f_L$). Any input signal with a frequency out of this band is attenuated. In this system, the required f_H and f_L are 300kHz and 30kHz, respectively.

The band-pass filter, with a 40-dB/decade roll-off, is formed by cascading a second-order Butterworth low-pass filter (Figure4.8) and a second-order Butterworth high-pass filter (Figure 4.9). Both filters have gain $G_{LP} = G_{HP} = 1.5$, respectively. The cutoff frequencies can be calculated by the following formulas.

$$f_H = \frac{1}{2\pi\sqrt{R_8 R_9 C_4 C_5}} \approx 300KHz$$

$$f_L = \frac{1}{2\pi\sqrt{R_{12} R_{13} C_6 C_7}} \approx 19KHz$$

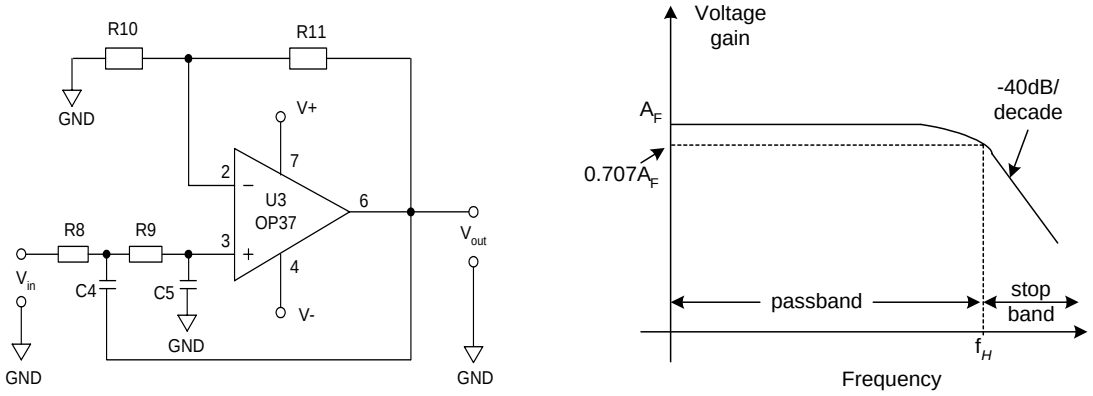

(a) (b)

Figure 4.8 Second-order low-pass Butterworth filter. (a) Circuit. (b) Frequency response.

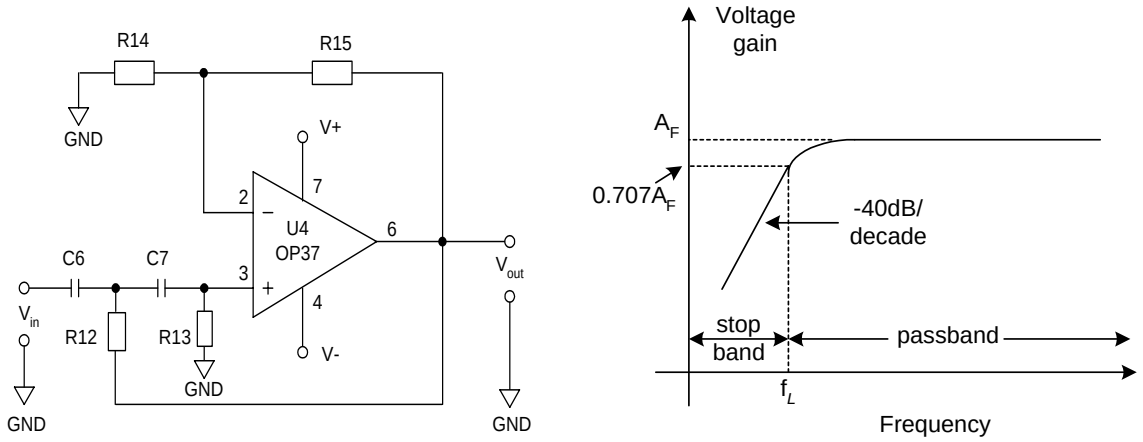

(a) (b)

Figure 4.9 Second-order high-pass Butterworth filter. (a) Circuit. (b) Frequency response.

4.3 Preliminary Test of the Signal Processing Unit

All circuits are installed in an aluminum enclosure with standard input and output connectors. The enclosure and the PCB are grounded and shielded very well to protect the circuits from most EMI and reduce parasitic oscillations. The frequency response of the three channels in the signal processing system is shown in Figure 4.10. The amplitude response non-flatness in the required bandwidth (30KHz to 300KHz) is less than 3.0dB. The largest difference between any two channels is less than 1dB.

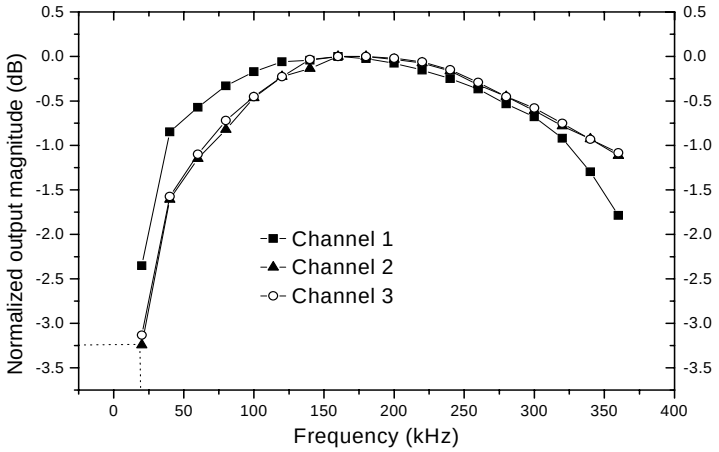

Figure 4.10 Frequency response of the signal processing system.

The electric noise of each channel is one of the main noise sources of the whole sensor system. Therefor, it is very important to keep the electric noise level as low as possible. Test results show that three channels have similar noise performance as shown in Figure 4.11 in the time domain and frequency domain, and the noise level of the electric circuit is about 15mV (peak-to-peak value). Figure 4.12 shows the noise performance of the whole sensor system, including the source, detector, optical connection, and electric unit, and the noise level is about 30 mV. More detailed noise performance and analysis will be performed in the following chapter.

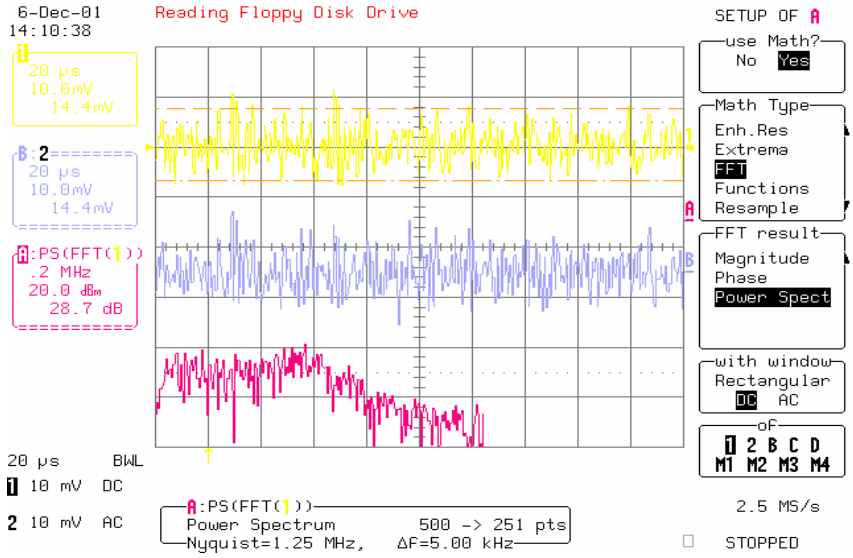

Figure 4.11 Noise performance of the electric circuit (Noise level~15mV)

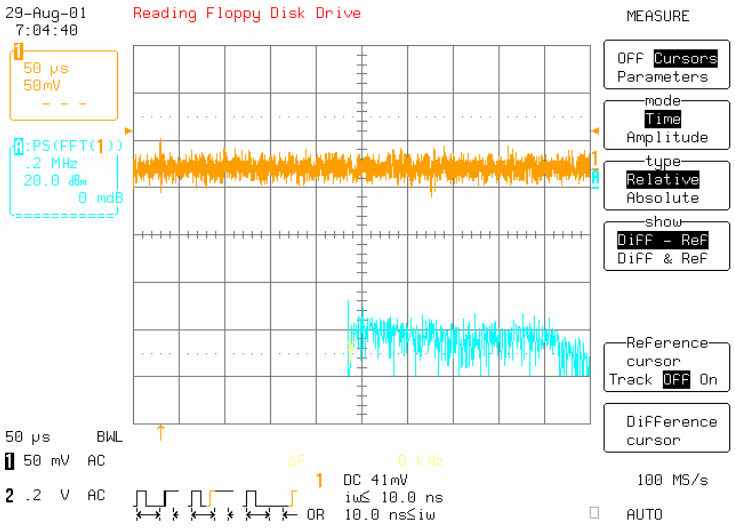

Figure 4.12 Noise performance of the whole system (Noise level <30mV)

In summary, the sensor system has following specifications for each channel:

(1) Frequency bandwidth (6dB): ~30 kHz – 300 kHz.

(2) Typical electrical noise in the bandwidth: 15mV

(3) Typical system noise level: < 30 mV

(4) The gain for each channel can be adjustable:

$$G = G_{I-V} \cdot G_m \cdot G_{LP} \cdot G_{HP} = 5.1 \sim 7.4 \times 10^6$$

(5) For the three channels, the amplitude response non-flatness in the required bandwidth (30KHz to 300KHz) is less than 3.0dB, and the largest difference between any two channels is less than 1dB.

Chapter 5. System Noise Analysis and Performance Improvement

As described in Chapter 2, the system signal-to-noises ratio (SNR) determines the minimum acoustic pressure that the sensor system can reach. The system noise associates with each individual electric element and optical component. A detailed analysis of these noise impacts or the performance of the diaphragm-based acoustic sensor system is very important for both system design and performance optimization.

The components of the diaphragm-based optical fiber acoustic sensor can be classified into two groups: 1) optical components, including the light source, the optical isolator, the optical connection components, and the diaphragm-based interferometric sensor heads; 2) electronic components, such as opto-electrical receiver, electrical amplifier, and band-pass filter. This chapter is dedicated to discuss the noise performance of both electronic and optical parts.

5.1 Electronic Noise

5.1.1 Electronic noise assumption

In the developed diaphragm-based acoustic system, a transimpedance amplifier is used to convert the optical current signals to the voltage outputs. The noise equivalent circuit of the transimpedance amplifier (as shown in Figure 4.6) is given in Figure 5.1[59,61,63]. The bandwidth of the transimpedance amplifier is *RC* limited and given by:

$$\Delta f = \frac{1}{2\pi R_f C_f}. \tag{5-1}$$

where R_f is the feedback resistance, and C_f is the feedback capacitance.

The output voltage (e_o) from the transimpedance amplifier can be calculated by

$$e_o = e_s + e_{no} = I_p R_f + e_{no}, \tag{5-2}$$

where e_s is the signal voltage of the amplifier, and I_p is the signal generated photocurrent from the photodetector. e_{no} is the total voltage noise of the amplifier which includes the shot noise of the detector (e_{nos}), the thermal noise of the feedback resistor (e_{noR}), the amplifier's input current noise (e_{noi}), and the amplifier's input voltage noise (e_{noe}). Since these noises are independent random processes that can be approximately modeled by Gaussian statistics, the total variance of voltage fluctuation at the output of the transimpedance amplifier can be obtained by adding individual variances. Therefore, the combined output voltage noise of all components is given by

$$e_{no} = \sqrt{e^2_{nos} + e^2_{noR} + e^2_{noi} + e^2_{noe}} \ . \tag{5-3}$$

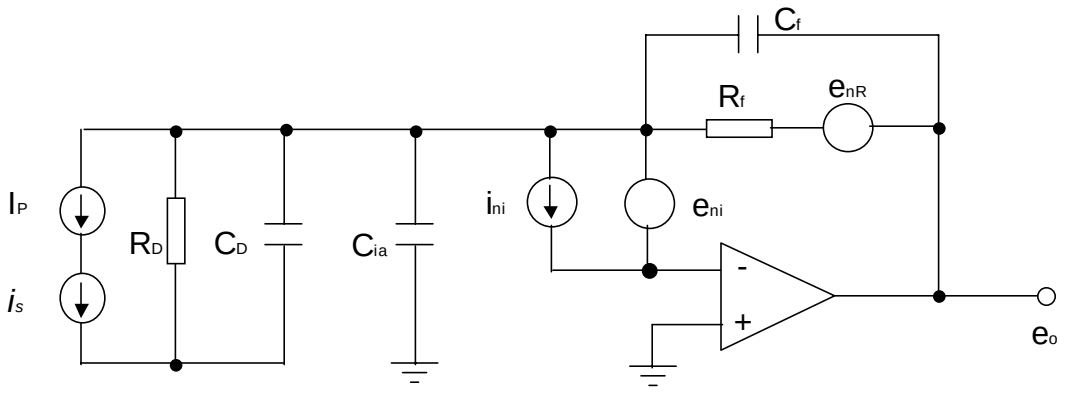

Figure 5.1. Noise equivalent circuit of the transimpedance amplifier

1. Effect of the photodetector shot noise

Shot noise of a photodetector is a manifestation of the fact that the electric current consists of a stream of electrons that are generated at random times. The photodiode current generated in response to a constant optical signal can be written as

$$\mathrm{I(t)} = I_p + i_s(t)\,, \tag{5-4}$$

where $I_p=RP_{in}$ is the average current and $i_s(t)$ is a current fluctuation related to shot noise. P_{in} is the input optical power to the photodetector and R is the responsivity of the photodetector in units of A/W. Mathematically, $i_s(t)$ is a stationary random process with Poisson statistics which in practice can be approximated by the Gaussian statistics. The

autocorrelation function of $i_s(t)$ is related to the spectral density $S_s(f)$ by the Wiener-Khinchin theorem

$$\langle i_s(t) i_s(t+\tau)\rangle = \int_{-\infty}^{\infty} S_s(f)\exp(2\pi i f\tau)df \ . \tag{5-5}$$

The spectral density of shot noise is constant and is given by $S_s(f)=qI_p$ (shot noise is called white noise for this reason). q is the charge on an electron (1.6×10^{-19} C).

The noise variance is obtained by setting $\tau=0$ in Equation (5-5) and is given by

$$\sigma_s^{\ 2} = \langle i_s^{\ 2}(t)\rangle = 2qI_p\Delta f \ , \tag{5-6}$$

where Δf is the effective noise bandwidth of the receiver. The actual value of Δf depends on where the noise is measured and it usually corresponds to the bandwidth of the amplifying circuits.

All photodetectors generate some current noises even in the absence of an optical signal because of stray light or thermal generation of electron-hole pairs. This residual current is referred to as the dark current. Since the dark current I_d also generates shot noise, its contribution is included in the following equation

$$\sigma_s^{\ 2} = 2q(I_p + I_d)\Delta f \tag{5-7}$$

The shot noise generated at the photodetector (i_s) will be amplified by the feedback resistor and gives the corresponding voltage noise (e_{nos}) given by

$$e_{nos} = i_s R_f = \sqrt{2q(I_p + I_d)\Delta f}\, R_f \ . \tag{5-8}$$

For photodetector F152 used in the system, R ~0.9A/W, and I_d ~10 nA. Δf is about 300KHz in our case, and R_f =100KΩ. In the case of no optical power, P_{in} = 0 W, e_{nos}~ 3 μV. For the typical case of P_{in} *~1-100* μW, I_p~ *1-90* μA, and e_{nos} ~ *0.03~0.3* mV.

2. Thermal noise of the feedback resistor

At a finite temperature, electrons in any conductor move randomly. Random thermal motion of electrons in a resistor manifests as a fluctuating current even in the absence of

an applied voltage. The load resistor in the front end of an optical receiver adds such fluctuations to the current generated by the photodiode. This additional noise component is referred to as thermal noise (also called Johnson noise or Nyquist noise). Thermal noise, defined as the current fluctuation $i_T(t)$, is modeled as a stationary Gaussian random process with a spectral density that is frequency independent up to 1Thz (nearly white noise) and is given by

$$S_T(f) = \frac{2k_B T}{R_L}, \tag{5-9}$$

where k_B is the Boltzmann constant (1.38×10^{-23}J/K), T is the absolute temperature, and R_L is the load resistor. $S_T(f)$ is also the two-sided spectral density, and it's autocorrelation function is given by

$$\langle i_T(t) i_T(t+\tau)\rangle = \int_{-\infty}^{\infty} S_T(f)\exp(2\pi i f\tau)df \tag{5-10}$$

The noise variance is obtained by setting $\tau=0$ and becomes

$$\sigma_s^{\,2} = \langle i_s^{\,2}(t)\rangle = \int_{-\infty}^{\infty} S_T(f)df = \frac{4k_B T}{R_L}\Delta f \tag{5-11}$$

where Δf is the effective noise bandwidth which is defined the same as before.

The thermal noise of the feedback resistor generates a voltage noise e_{noR} that can be expressed by

$$\mathrm{e_{noR}} = \sqrt{(4k_B T / R_f)\Delta f}\, R_f = \sqrt{4k_B T R_f \Delta f}\ . \tag{5-12}$$

At room temperature (T~300K), e_{noR} is in the range of 0.01 mV.

3. Amplifier's input current noise

e_{noi} is the output noise components produced by the amplifier's input current noise ($i_{ni} = \sqrt{2qI_{B-}\Delta f}$) which is a shot noise produced by the input bias current I_{B-}. This noise current flows directly through the feedback resistor, producing a noise voltage of

$$\mathrm{e_{noi}} = R_f\sqrt{2qI_{B-}\Delta f}\ . \tag{5-13}$$

Choosing a FET-input operational amplifier with an I_{B-} in the picoampere range generally makes this noise component negligible for practical levels of feedback resistance. For the OP-37 operational amplifier, the input current noise is $I_{B-} = 10nA$. So, $e_{noi} \sim 3$ μV.

4. Amplifier's input voltage noise

e_{noe} represents output noise components produced by the amplifier's input voltage noise. Within the response boundary of the op amp, this noise can be calculated by:

$$e_{noe} = \frac{1 + R_f C_i s}{1 + R_f C_f s} e_{ni} \tag{5-14}$$

This will be a high frequency noise when the capacitors dominate the noise gain. For the OP-37 amplifier, $e_{ni}=3nv/\sqrt{Hz}$. Then, $e_{noe} \sim 2\ \mu V$.

5.1.2 Power budget and electronic noise estimation of the sensor system

Assume that the maximum output power from the SLED source is 16 mW. The isolator typically has 3dB (50%) loss. The 1x3 coupler splits the light into three channels (33%). The 2x2 coupler in each channel introduces a loss of 75% because of the double passes. Assuming the reflection of the fiber endface is 20%. If counting for the two reflections at the sensor head, the total average reflected power will be 40% of the incident power. There are other losses associated with fiber bending and light coupling, which is wise to allow a loss margin of 3-6dB (50~75%) power loss. The loss items with their estimated values are listed in Table 5-1.

Table 5-1. Optical loss mechanisms in single-mode DOFIA system

Optical loss mechanisms	Value
Isolator (L_{iso})	50%
1x3 beam splitter (L_{13})	67%
2x2 coupler(L_{22})	75%
Average reflection of the fiber ends ($\boldsymbol{r_f}$)	30~40%
Loss margin for fiber deployment ($\boldsymbol{L_{fiber}}$)	6dB (75%)

Therefore the optical power seen by the photodetector at the signal channel can be estimated to be

$$P_{in} = P_s \times (1 - L_{iso}) \times r_f \times (1 - L_{13}) \times (1 - L_{22}) \times (1 - L_{fiber})$$
$$= 66\mu W$$

According to Equ. (5-3) and discussions above, the total electrical noise at the I-V converter stage, shown as in the Figure 4.6, is

$$e_{no} = \sqrt{e^2_{nos} + e^2_{noR} + e^2_{noi} + e^2_{noe}} = \sqrt{(0.03 \sim 0.3)^2 + (0.01)^2 + (0.003)^2 + (0.002)^2}$$
$$= 0.032 \sim 0.3 \quad mV$$

This noise would be further amplified by subsequent stages. As illustrated in Section 4.2, the gain-tunable amplifier and the band-pass filter provide extra gain from 35 to 50. Therefor, the total electrical noise of the whole system is within the range of 1-15mV, which matches the experiment results (~15mV) very well, shown in Figure 4.11.

5.2 Optical Noise in Diaphragm-Based Acoustic Sensor System

Besides the noise associated with the receiving electronics, the noise coming from the optical parts can also cause measurement errors. The optical power intensity and phase/frequency fluctuations of the source are categorized as the main optical noise sources in the sensor system. It is thus necessary to analyze and investigate the laser noise in the system. The same analysis would also be suitable for other fiber interferometric sensors as well. Furthermore, the impact of optical feedback on the sensor system performance will be addressed.

5.2.1 Noise analysis for light source

The output of a semiconductor laser exhibits fluctuations in its intensity, phase, and frequency even when the laser is biased at a constant current. Spontaneous emission is one of the fundamental noise mechanisms in semiconductor lasers [63,64,65]. It results in 1) emitted optical intensity fluctuation, which is characterized by the so-called relative

intensity noise (RIN), and 2) emitted frequency fluctuations, which are responsible for the finite spectral linewidth of laser diodes.

5.2.1.1 Relative intensity noise (RIN)

The emitted optical power P is assumed to exhibit noise, so that the time dependent power $P(t)$ is written as

$$P(t) = \langle P \rangle + \delta P(t) \tag{5-15}$$

with the mean power $\langle P \rangle$. The noise may be described in the time domain by the autocorrelation function:

$$\rho_P(\tau) = \langle \delta P(t) \delta P(t-\tau) \rangle \tag{5-16}$$

In the frequency domain, the noise can also be described with the spectral density $W_P(\omega_m)$ at the circular frequency ω_m

$$\begin{aligned} W_P(\omega_m) &= \left\langle \left| \Delta P(\omega_m) \right|^2 \right\rangle = \int_{-\infty}^{\infty} \rho_P(\tau) \exp(-j\omega_m \tau) d\tau \\ &= \lim_{t' \to \infty} \frac{1}{t'} \left| \int_0^{t'} \delta P(t) \exp(-j\omega_m t) dt \right|^2 \end{aligned} \tag{5-17}$$

The spectral density and the autocorrelation function represent a Fourier transform pairs (Wiener-Khintchine relations). The mean-square of the noise signal $\delta P(t)$ can be expressed in terms of the spectral density $W_P(\omega_m)$

$$\left\langle \delta P^2(t) \right\rangle = \rho_P(0) = \int_{-\infty}^{\infty} W_P(\omega_m) df = \int_{-\infty}^{\infty} \left\langle \left| \Delta P(\omega_m) \right|^2 \right\rangle df \qquad \text{with } f = \omega_m / 2\pi \tag{5-18}$$

If the noise is passing a filter with a center frequency ω_m and bandwidth Δf, the noise mean-square value would be:

$$\left\langle \delta P^2 \,|_{\Delta f} \right\rangle = 2\Delta f \left\langle \left| \Delta P(\omega_m) \right|^2 \right\rangle = 2\Delta f W_P(\omega_m) \tag{5-19}$$

Therefore, the relative intensity noise is defined as:

$$RIN = \frac{\left\langle \delta P^2 \right\rangle}{\langle P \rangle^2} = \frac{2\Delta f \left\langle \left| \Delta P(\omega_m) \right|^2 \right\rangle}{\langle P \rangle^2} = \frac{2\Delta f W_P(\omega_m)}{\langle P \rangle^2} \tag{5-20}$$

5.2.1.2 Requirement of RIN for the sensor system

Based on the definition of *RIN* above, let's consider the RIN requirement for ensuring the final performance of the sensor system, which is the first step to design and evaluate any lightwave system.

In the acoustic sensor system, the laser source works in a CW mode. The sensing signal is actually 'modulated' by the acoustic wave through the diaphragm. We may consider the sensor system as an analogue sinusoidally modulated system, which is similar to a subcarrier multiplexing-SCM system used commonly by CATV industry [63]. Hence, a signal-to-noise ratio (SNR) in this case would be introduced as:

$$SNR = \frac{m^2}{2}\frac{\langle P \rangle^2}{\langle \delta P^2 \rangle} = \frac{m^2}{2RIN} \tag{5-21}$$

m is the modulation index with upper limit 1. Assuming the final sensing signal with SNR=50dB (10^5), and *m*=1, it yields RIN = 5 x 10^{-6}. For the acoustic sensing bandwidth 300KHz in our diaphragm-based PDs system, this requires the laser have $RIN / \Delta f = 1 \times 10^{-11} / Hz$, which is the bottom line for the laser noise.

The actual RIN of most of laser light sources is lower than the required RIN. For example, the RIN of a common SLED source is about ~ 10^{-13} /*Hz* (-130dB/Hz), while a DFB laser has typical RIN ~ 10^{-15}/*Hz* (-150dB/Hz). However, the margin is not very large if the electric noise is added later. Especially, in the sensor system where the interference and optical feed-back exist, the laser RIN may increase, as discussed in the following sections.

5.2.1.3 Phase and frequency noise of the laser source in the interferometric system

The phase noise is contributed directly by the spontaneous emission, and leads to a finite spectral linewidth ($\Delta\nu = \Delta\omega/2\pi$) of laser emission [66,67]. If the laser light with spectral

linewidth $\Delta\nu$ is fed through an interferometer, as sketched in Figure 5.2, let's figure out how the frequency noise affects the output performance after the interferometric sensor.

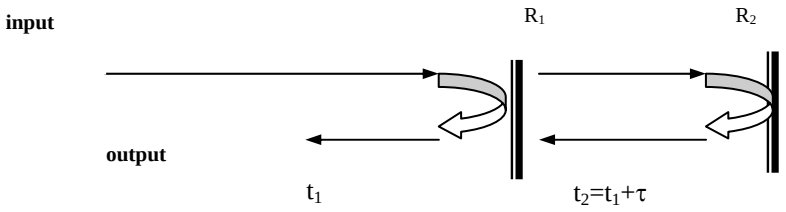

Figure 5.2 Schematic representation of an diaphragm interferometer

In the sensor scheme in Figure 5.2, the light of one reflecting surface is delayed by τ with respect to the other. If the laser field is represented by $E_L(t)$ and assumed that two light beams have similar intensity, the transmitted output power would be [68,69]

$$P_T(t) = |A|^2\{|E_L(t)|^2 + |E_L(t-\tau)|^2 + 2\,\mathrm{Re}(E_L(t)E_L^*(t-\tau))\} \tag{5-22}$$

We define the complex degree of coherence

$$\gamma_E(\tau) = \frac{\langle E_L(t)E_L^*(t-\tau)\rangle}{\langle |E_L(t)|^2\rangle} \tag{5-23}$$

then the mean output power $\langle P_T(t)\rangle$ would be

$$\langle P_T(t)\rangle = 2|A|^2\langle |E_L(t)|^2\rangle[1+\mathrm{Re}(\gamma_E(\tau))] \tag{5-24}$$

For the sake of discussion simplicity, a single-mode laser is considered with lasing field

$$E_L(t) = \sqrt{S}\exp(j\phi(t)\exp(j\omega_{th}t) \tag{5-25}$$

where ω_{th} is the resonance frequency in the laser diode, and $\phi(t)$ is the phase of the laser. To describe the statistics of phase noise, we introduce the instantaneous frequency $\dot{\phi} = d\phi/dt$ which corresponds to the instantaneous frequency deviation from ω_{th}. The difference between $\dot{\phi}$ and the mean value $\langle\dot{\phi}\rangle$ can be described as

$$\delta\dot{\phi} = \dot{\phi} - \langle\dot{\phi}\rangle \tag{5-26}$$

then the phase difference $\delta\phi$ is

$$\delta\phi = \phi - \langle\dot{\phi}\rangle t \tag{5-27}$$

So, the mean frequency of laser emission corresponds to $\langle\omega\rangle = \omega_{th} + \langle\dot{\phi}\rangle$. We have

$$E_L(t) = \sqrt{S}\exp(j\langle\omega\rangle t)\exp(j\delta\phi(t)) \tag{5-28}$$

Eq. (5-22) can be rewritten as

$$P_T(t) = P_{T0}[1+\cos(\langle\omega\rangle\tau + \Delta\phi(t,\tau))] = P_{T0}[1+\cos(\phi_0 + \Delta\phi(t,\tau))] \tag{5-29}$$

The noise of the phase change $\Delta\phi$ is thus transferred to an intensity noise of $P_T(t)$. The term of $\langle\omega\rangle\tau$ represents the mean phase difference between the two reflection beams, which is denoted as ϕ_0. Then, the mean power $\langle P_T(t)\rangle$ of Eq. (5-29) is given as

$$\langle P_T(t)\rangle = P_{T0}[1+\cos(\phi_0)\langle\cos(\Delta\phi(t,\tau))\rangle] \tag{5-30}$$

since $\langle\sin(\Delta\phi(t,\tau))\rangle = 0$. The fluctuation of the output power is expressed by

$$\delta P_T(t) = P_T(t) - \langle P_T(t)\rangle \tag{5-31}$$

The noise of the output power in the time domain would be derived from the autocorrelation function of δP_T, which is expressed as $\langle\delta P_T(t)\delta P_T(t-\tau)\rangle$. The spectral density of the phase-induced intensity noise at the interferometer output is obtained as the Fourier transform of $\langle\delta P_T(t)\delta P_T(t-\tau)\rangle$ as

$$\begin{aligned}\langle|\Delta P_T(\omega_m)|^2\rangle &= \int_{-\infty}^{\infty}\langle\delta P_T(t)\delta P_T(t-\delta\tau)\rangle d(\delta\tau) \\ &= t_c(P_{T0}^2/2)[f(|\tau|/t_c) - \cos(2\phi_0)h(|\tau|/t_c)]\end{aligned} \tag{5-32}$$

with $$f(|\tau|/t_c) = 1-(1+2|\tau|/t_c)\exp(-2|\tau|/t_c) \tag{5-33}$$

and $$h(|\tau|/t_c) = \exp(-4|\tau|/t_c) + \exp(-2|\tau|/t_c)(2|\tau|/t_c - 1) \tag{5-34}$$

For small delay difference $|\tau| << t_c$ in the coherent region one obtains $f \approx h \approx 2/(|\tau|/t_c)^2$ whereas for larger $|\tau| >> t_c$ in the incoherent regime *f~1* and *h~0.*

Figure 5.3 shows the normalized spectral noise density at the interferometer output as a function of the delay difference $|\tau|$ between the optical beams. As a general rule, the noise at the interferometer output increases with the increasing of $|\tau|$, if the coherence time t_c of the laser diode is held constant. Therefore, for an interferometer fiber sensor, the imbalance between the interferometer arms and thus $|\tau|$ should be as small as possible.

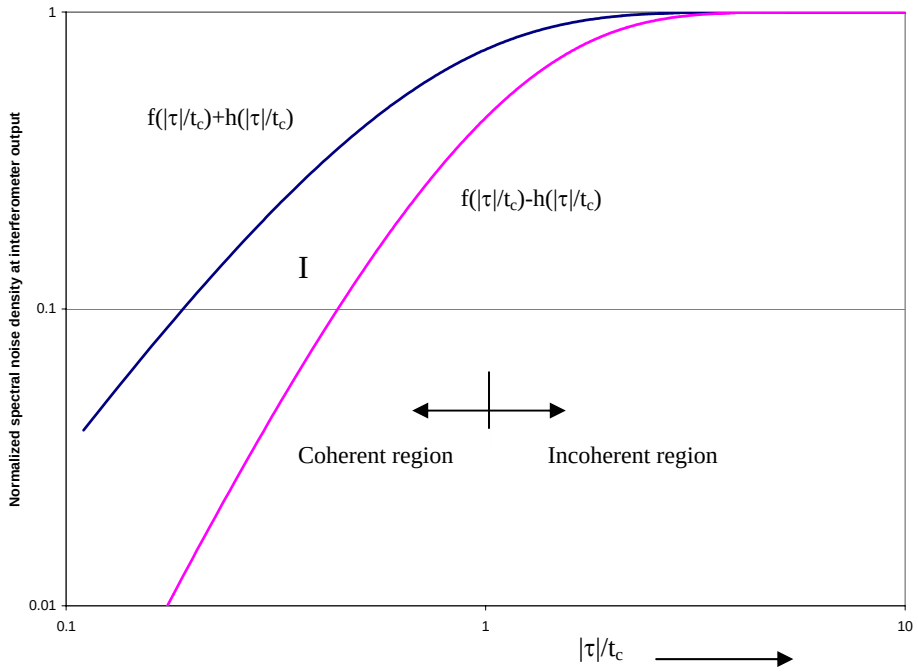

Figure 5.3. Normalized spectral noise density. The actual spectral noise density distributes in the region I.

For a given interferometer with a certain delay difference τ, the noise at the interferometer output depends strongly on the coherence time t_c of the laser source. In the region for $t_c >> |\tau|$ the noise decreases with increasing t_c (i.e. decreasing laser linewidth), since the *f* and *h* become very small. However, large noise appears if the coherence time is in the same order as the τ.

Based on the definition of RIN (Eq. (5.20)), the RIN induced by the phase noise in the interferometer output may be expressed as

$$RIN = \frac{\langle |\Delta P_T(\omega_m)|^2 \rangle 2\Delta f}{\langle P_T(t) \rangle^2} = \Delta f t_c [\, f(|\tau|/t_c) - \cos(2\phi_0) h(|\tau|/t_c)] \qquad (5\text{-}35)$$

Assuming that the diaphragm sensor is set at the Q point ($\phi_0=\pm\pi/2$) and the air gap is about 5 μm, which corresponds to τ=10 μm/c=3.4x10^{-5}ns, we will compare the intensity noise induced by a DFB laser and a SLED source.

For DFB laser (1310nm) with typical spectral linewidth $\Delta\nu$=1MHz (i.e. $t_c=1/\pi\Delta\nu$=318ns, and coherent length $L_c=ct_c=95m$), one obtains that

$$RIN\,|_{\Delta\nu=1MHz}=1.7\times10^{-30}\,\Delta f\ /\ Hz$$

For a SLED (1310nm) with spectral bandwidth (FWHM) $\Delta\lambda$~40nm, which corresponds $\Delta\nu=c\Delta\lambda/\lambda^2$=7.1THz, t_c~1.4x10^{-4}ns, and L_c~42 μm, we obtain

$$RIN\,|_{\Delta\nu=7.1THz}=5.3\times10^{-14}\,\Delta f\ /\ Hz$$

It turns out that the DFB laser has better performance in phase-induced RIN than the SLED in the interferometer with a small cavity (~10 μm). But, the RIN caused by the SLED is still much lower than the bottom line of the required noise figure (10^{-11}). So, the phase-noise of the source is not a dominant factor for the sensor system.

5.2.2 Impact of optical feedback on the sensor performance

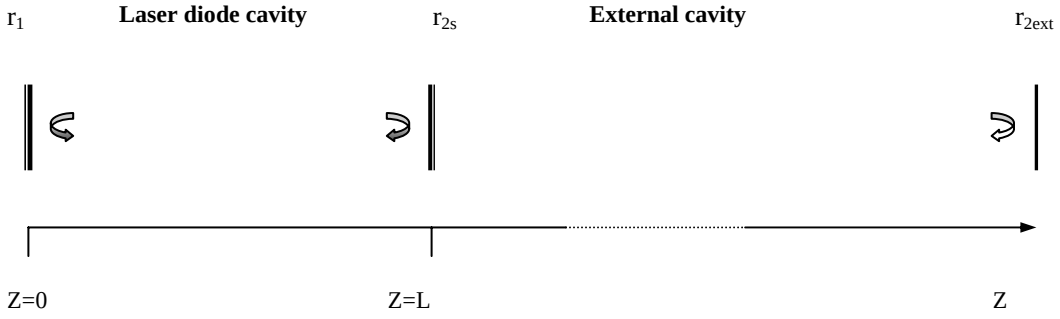

Figure 5.4. Schematic arrangement of a laser diode cavity with external optical feedback

An important issue that needs to be addressed in designing an optical interferometer sensor is related to the extreme sensitivity of semiconductor lasers to optical feedback [70,71,72]. In the diaphragm-based sensor system, the sensor head actually serves as a

distant reflection face, which can be simply schemed as in Figure 5. 4. A Fabry-Perot laser diode has the facet reflection coefficients r_1 and r_{2s}, and the external cavity has the reflection coefficient r_{2ext}. To take the effects from r_{2ext} to the laser diode into account, an effective reflection coefficient r_2 at $z=L$ is introduced as

$$r_2(\nu) = r_{2s} + (1-|r_{2s}|^2) r_{2ext} \exp(-j2\pi\nu\tau_{ext}) \tag{5-36}$$

τ_{ext} denotes the round trip delay (forth and back) through the external cavity of the length L_{ext}.

Due to the external optical feedback, the effective reflection coefficient of the laser diode is changed, which modifies the phase and amplitude relations in the diode. As a result, the emission frequency (ν), the threshold gain (g), the effective refractive index (μ_e), and finally the phase conditions (ϕ) may be off from their initial value (without feed back). It is reported that the phase change due to the feed-back can be expressed as [65]

$$\Delta\phi_L = 2\pi\tau_L(\nu-\nu_{th}) + \kappa_{ext}\sqrt{1+\alpha^2}\,\sin(2\pi\nu\tau_{ext} + \arctan\alpha) \tag{5-37}$$

where

$\Delta\phi_L$: the round trip phase change;

τ_L: the round trip delay in the laser diode, and $\tau_L = 2\mu_e L/c$;

ν_{th}: the emission frequency of laser without feed-back;

κ_{ext}: the coupling coefficient, $\kappa_{ext} = \frac{r_{2ext}}{r_{2s}}(1-|r_{2s}|^2)$; (5-38)

α: the parameter related to the change in the real part of refractive index and the change in its image part. This α-parameter is of the order of 3~7.

Based on Eq. (5-37), the feedback coefficient C is defined to characterize behaviors of the laser diode with the external optical feedback

$$C = X\sqrt{1+\alpha^2} \tag{5-39}$$

with $$X = \frac{\tau_{ext}}{\tau_L}\kappa_{ext} \tag{5-40}$$

Then, Eq. (5-37) becomes

$$\Delta\phi_L = 2\pi\tau_L(\nu - \nu_{th}) + C\frac{\tau_L}{\tau_{ext}}\sin(2\pi\nu\tau_{ext} + \arctan\alpha) \qquad (5\text{-}41)$$

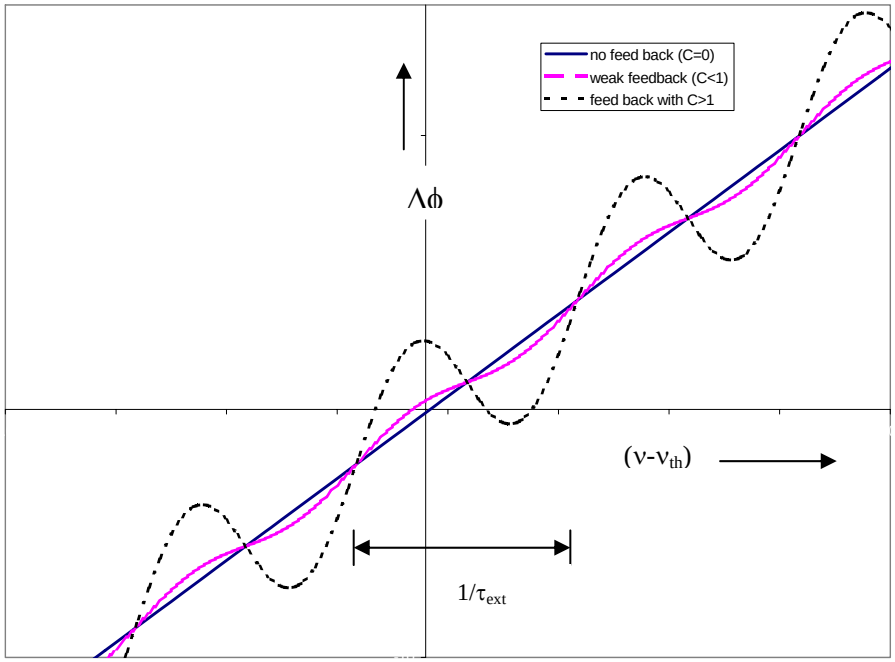

Figure 5.5 Round-trip phase change $\Delta\phi_L$ versus optical frequency ν with and w/o feedback

Figure 5.5 shows the round-trip phase change $\Delta\phi_L$ versus the frequency ν. Possible emission frequencies, where the phase condition satisfied, are characterized by $\Delta\phi_L = 0$. Without feedback, as represented by the solid curve, $\Delta\phi_L$ varies linearly with ν, yielding its zero at $\nu = \nu_{th}$. As long as C is very small, $\Delta\phi_L$ will monotonically increase with frequency yielding a single zero for $\Delta\phi_L$ and thus a single emission frequency. For larger C (dashed curve), the $\Delta\phi_L$ versus ν-characteristic may undergo strong oscillations yielding multiple zeros for $\Delta\phi_L$. In this case, several modes around emission frequency ν_{th} of the laser may eventually oscillate, which will make the mode-hoping and laser output unstable.

Many papers have been published to discussing the feedback impact on the laser diode [69,70,71]. Usually, it is very convenient to divide C into five feed back regimes according to the impact on the laser diode. For regime of $C<1$ (Regime I), the laser

emission is very stable since no additional cavity mode is allowed. However, in the regime (II) of *1<C<30*, multiple cavity modes are allowed theoretically. Depending on the phase of the reflected light, one or more external cavity modes start lasing, corresponding to a mode-hopping between different external cavity modes. When *C* increases and enters the regime III (*30<C<60*), one obtains a stronger variation of the threshold gain g_c for the different external cavity modes, yielding a stabilization for the external cavity mode with the largest linewidth reduction. A further increase of feedback into regime IV (*C>60*) yields strong instabilities, the so-called 'coherence-collapse', with multiple external cavity modes, spectral linewidths of several 10GHz and a tremendous intensity noise [23].

Let's consider a laser source connecting a real diaphragm-based sensor with a 3-dB fiber coupler, as shown in Figure 5.6.

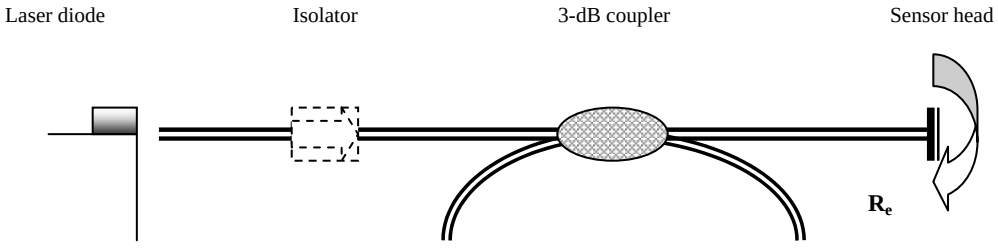

Figure 5.6 Laser diode with a fiber pigtail and a sensor head

In this system, the reflective output from the sensor head is denoted as R_e. The isolator has isolation *H*. The coupling efficiency from the laser diode into the single-mode fiber is denoted as β (typically value 20%). Then, Eq. (5-39) and (5-40) would be modified as

$$X = \frac{\tau_{ext}}{\tau_L}\sqrt{\frac{R_{2ext}}{R_{2s}}}(1-R_{2s}) \tag{5-42}$$

and $$R_{2ext} = \beta^2 H R_e / 4 \tag{5-43}$$

$$C = \frac{\tau_{ext}}{\tau_L}\sqrt{\frac{R_{2ext}(1+\alpha^2)}{R_{2s}}}(1-R_{2s}) \tag{5-44}$$

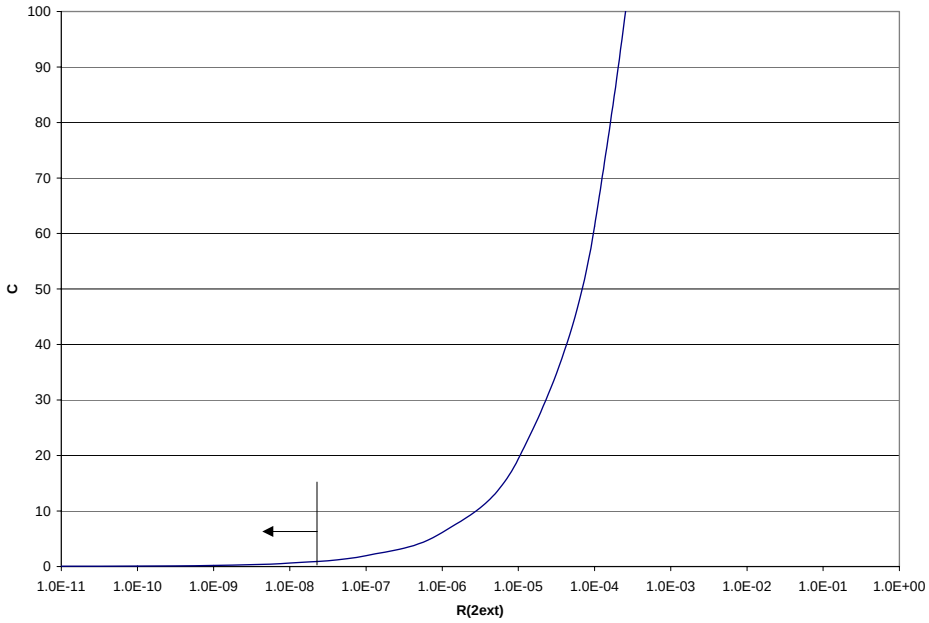

Figure 5.7 C curves as function of R_{2ext} for a laser diode.

Assume the pigtailed fiber is 2 *m* in length, which corresponds to $\tau_{ext} \approx 10ns$, and the laser diode has $\tau_L = 10\,ps$ (the laser length is about 300~400um) with facet reflectivity $R_{2s} = 0.32$. For a glass-air interface in the sensor head, R_e=4%. In the case that there is not any isolator connected in the fiber, one obtains $R_{2ext} = 4 \times 10^{-4}$, and *C*=122>>1. The laser works in the Region IV and is expected to perform extremely unstable, according to Figure 5.5 and Eq. (5-41). While in the case that an isolator with $H=10^{-3}$ (30dB), we get $R_{2ext} = 4 \times 10^{-7}$, and *C=3.87>1.* one or more external cavity modes may be exited, and results in mode-hopping between different external cavity modes. If increasing the isolation to 50dB (dual-stage isolator), we will get R_{2ext} = 4x10^{-9}, and *C=0.387*. The laser system will be stabilized.

Figure 5.7 shows the C curves as function of R_{2ext} for this laser diode. Obviously, in order to get a stable output in this laser-sensor system, it is required to keep the R_{2ext} less than 10^{-7} and ensure C<1. The higher the isolation, the more stable the laser. On the other hand, Eq.(5-43) and (5-44) indicate that higher isolation is needed to keep the laser stable if the reflectance of the sensor surface is increased. This means that the reflectance of

interferometer can not be too high. The medium-fineness interferometric sensor not only provides good pressure sensitivity, but also keeps the reflection-induced noise at a acceptable level. For example, in the case we discussed above, if $R_e=20\%$, and the isolation stays 50dB, we will get R_{2ext} = 20x10^{-9}, and $C=0.865<1$. So, the laser still has stable performance.

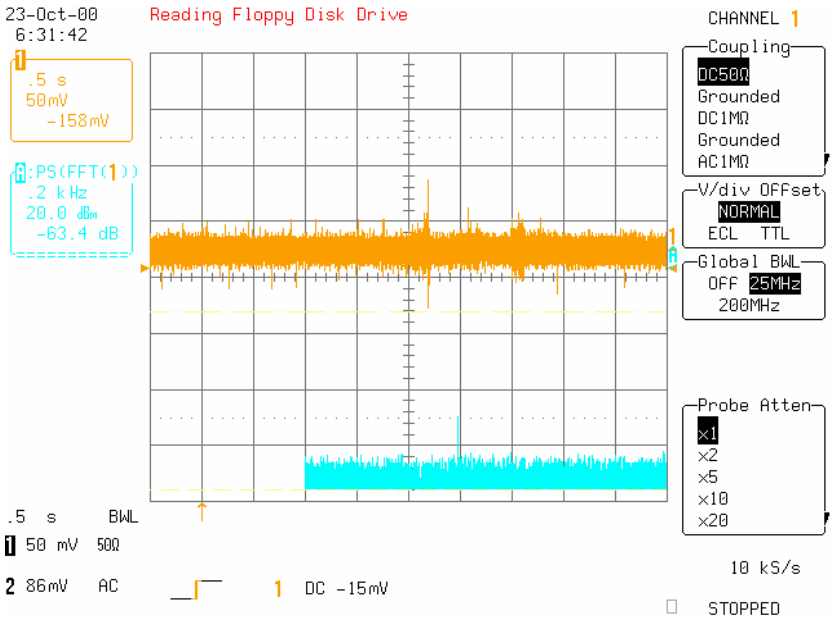

(a)

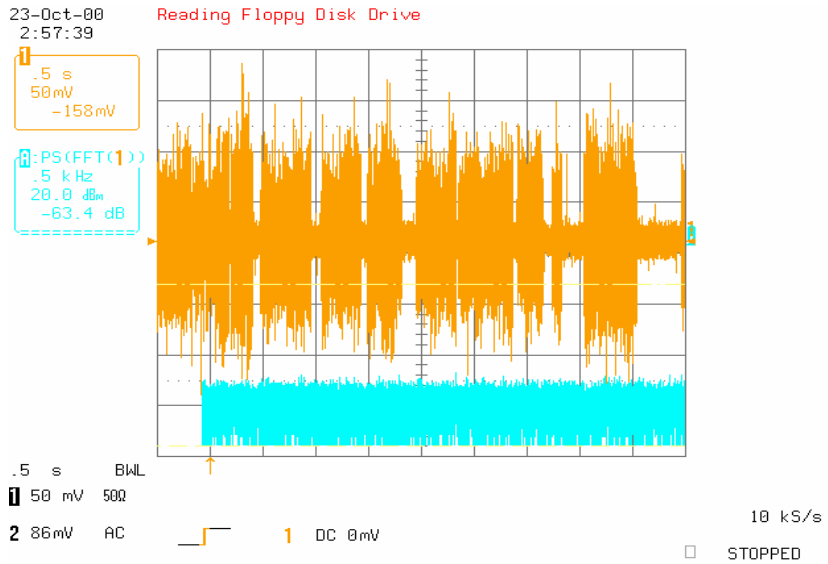

(b)

Figure 5.8 Noise performance in the DFB-sensor system (a) with isolation H=45dB, noise~40mv, and (b) without isolator, noise level >200mv

Figure 5.8 illustrates a DFB-sensor system with 20% reflectance at the sensor head. In the case that an isolator (H=45dB) is connected after the DFB laser, the noise level is about 40mV (peak-to-peak), as shown in Figure 5.8(a). If the isolator is removed from the sensor, the noise jumps up to unacceptable level (>200mv, Figure 5.8 (b)), and the sensor output becomes extremely unstable.

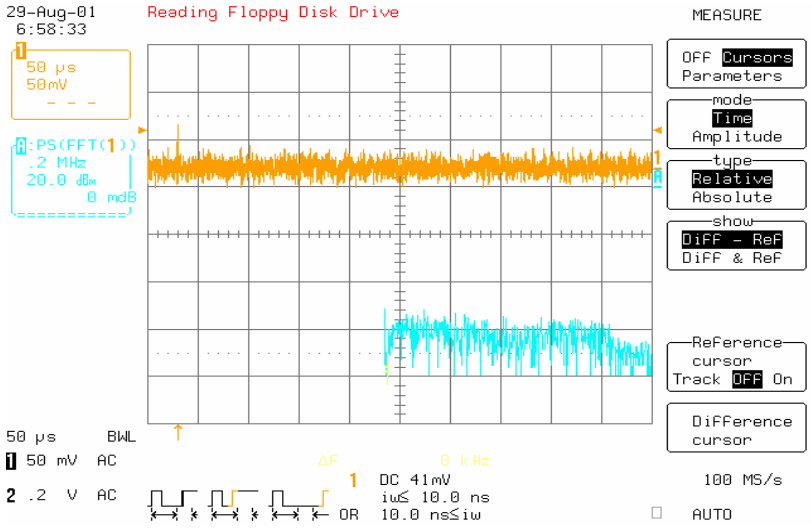

(a)

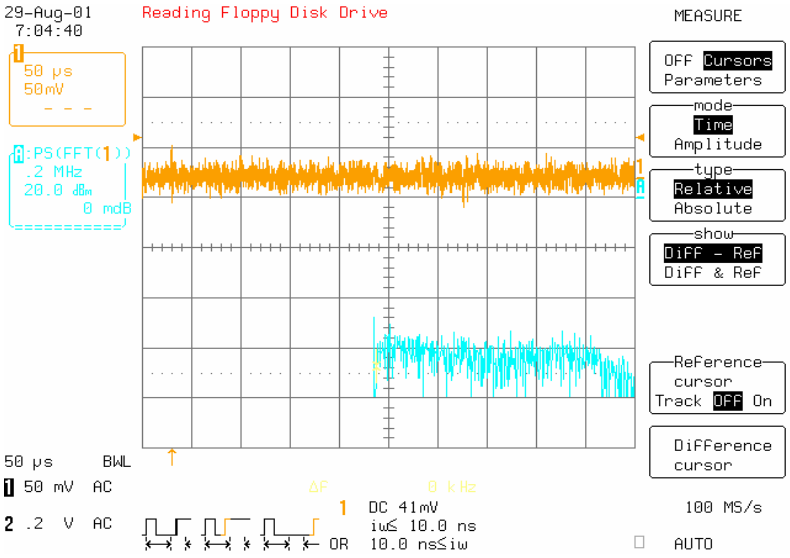

(b)

Figure 5.9 (a) 1310nm SLED source without reflectivity end-face at the fiber end, noise ~25mv; (b)1310nm SLED source with reflectivity end-face at the fiber end, noise ~30mv

According to Eq. (5-38, 39, 40), the feedback sensitivity of laser diodes is governed essentially by the feedback parameters C, X and κ_{ext}. For a given laser diode characterized by its round trip delay τ_L, and its facet reflectivity R_{2s}, which is operated at a certain optical power, the feedback is characterized by its effective external reflectivity R_{2ext} and the external round trip delay τ_{ext}. On the other hand, for a given external cavity with given reflectivity, the laser with larger round trip delay τ_L (i.e. long laser diode) and larger reflectivity $R_{2s} = r_{2s}^2$ should have low feedback sensitivity. Therefore DFB lasers are often more sensitive to feedback than Fabry-Perot-type lasers because DFB lasers have relatively small reflectivity and small cavity length.

Figure 5.9 shows the noise performance of a SLED source with and without optical feedback. The SLED source is pig-tailed with a 45dB isolator and a 3 dB coupler. The fiber end-face has ~4% reflectivity after cleaved. If the end-face is inserted into the index matching gel, the reflection would be eliminated. From Figure 5.9, the noise intensity of the source doesn't show a significant increase in the stronger reflection case.

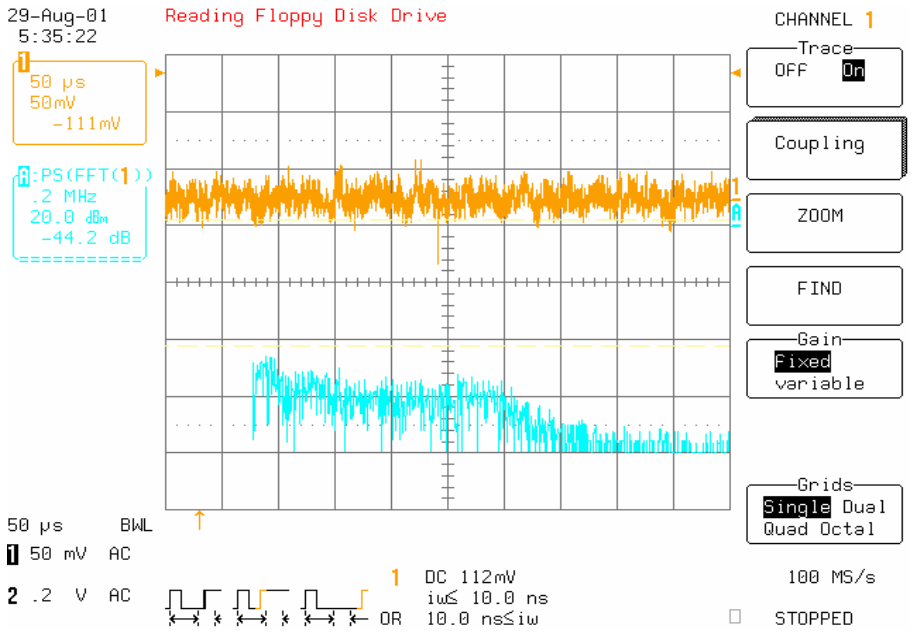

(a)

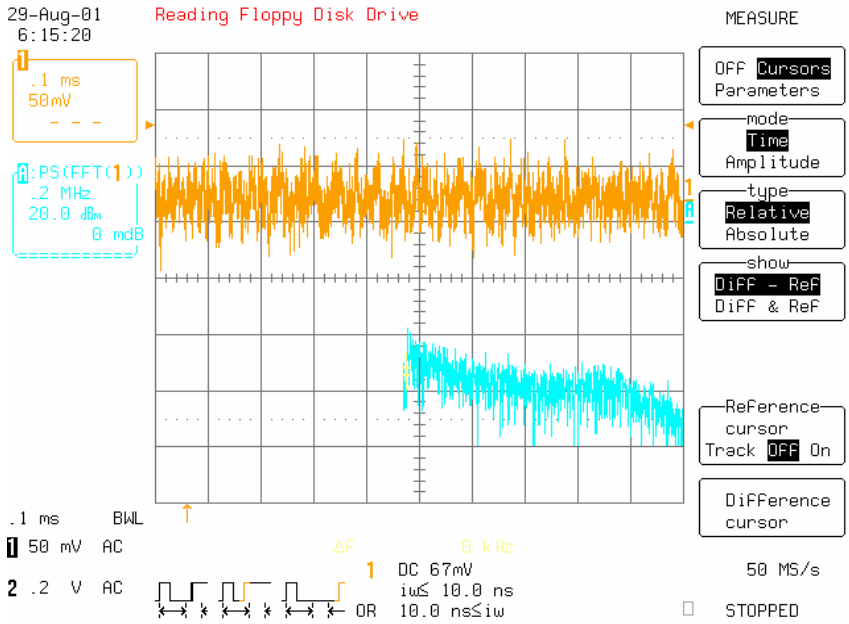

(b)

Figure 5.10. (a) 1310nm DFB laser without reflectivity end-face at the fiber end, noise ~40mv; (b) 1310nm DFB laser with reflectivity end-face (4%) at the fiber end, noise ~75mv

However, when the source is switched to a DFB laser with the same isolator and coupler, it is observed that the noise intensity is almost doubled when the reflection exists, as shown in Figure 5.10. This indicates that the DFB laser is much more sensitive to back reflections than the SLED source even with an isolator used to further reducing the reflection.

Chapter 6. Temperature Cross-Sensitivity in DOFIA Sensor

6.1 Mechanisms of Temperature Cross-sensitivity

In the PD detection, we hope the sensor could maintain its high sensitivity at all time. However, like regular interferometers, the measurement would suffer from the disadvantages of sensitivity reduction and fringe direction ambiguity when the sensor reaches peaks or valleys of the fringes. Even though the initial air gap can be set at the central point of an interference fringe, some environmental changes, such as temperature variations, could cause the initial air gap shifting away from the operating point.

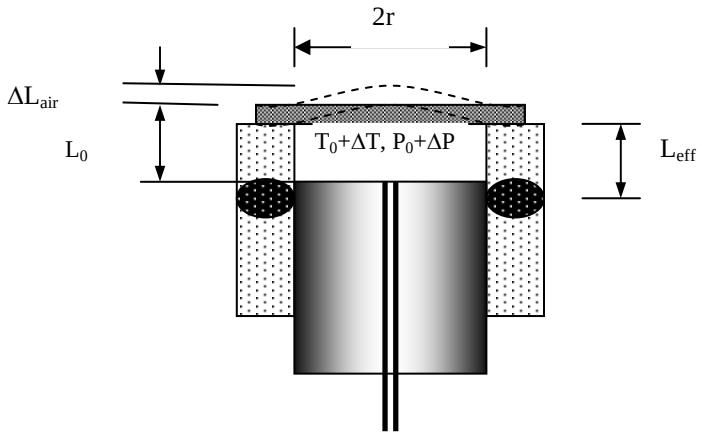

Figure 6.1 Thermal expansion model of sensor head

The temperature cross-sensitivity of the sensor results from the thermal expansion of each component of the sensor head, such as the outside tubing, the bonding material, the sealed cavity air and the diaphragm, as shown in Figure 6.1.

The sealed air in the cavity would be expanded (or shrunk) while temperature changes (ΔT). For the sake of discussion simplicity, we consider the sealed air as an ideal gas column with initial volume $V_0 = \pi r^2 L_0$ and initial pressure P_0 in Pa. According to the ideal gas law, we have:

$$PV = nRT \tag{6-1}$$

where R is the molar gas constant (R=8.314 J·mol^{-1}·K^{-1}), and n is the gas molar amount, which may be estimated from the molar volume of ideal gas (22.4 m^3·mol^{-1} @T=0°C and P=1 atm). We may obtain the differential format of Eq. (6-1).

$$-P\Delta V + V\Delta P = nR\Delta T \tag{6-2}$$

Since $V = \pi r^2 L_0$, Eq.(6-2) becomes:

$$-P\Delta L_{air} + L_0\Delta P = 0.3712\times 10^3 L_0\Delta T \tag{6-3}$$

The diaphragm would be deformed due to the expansion of the air. According to Eq. (2-14), we obtain:

$$\frac{\Delta L_{air}}{\Delta T} = \frac{L_0 0.3712\times 10^3}{-P_0 + 4.0493\times 10^{11}\dfrac{L_0 h^3}{r^4}} \tag{6-4}$$

Besides, another contribution of the air gap change comes from the thermal expansion of the glass tubing and the bonding material, which can be expressed as:

$$\frac{\Delta l_{\exp}}{\Delta T} = l_{eff}\alpha \tag{6-5}$$

where α is the coefficient of thermal expansion (CTE) of the tubing material (~5.5x 10^{-7}/K), l_{eff} is the effective length between the bonded diaphragm and the bonding point on the tubing.

Therefore, the total air gap length shift (ΔL_{tot}) due to the temperature fluctuation (ΔT) can be expressed as:

$$\beta = \frac{\Delta L_{tot}}{\Delta T} = \frac{\Delta L_{air}}{\Delta T} + \frac{\Delta L_{\exp}}{\Delta T} = \frac{L_0 0.3712\ \times 10^3}{-P_0 + 4.0493\ \times 10^{11}\dfrac{L_0 h^3}{r^4}} + l_{eff}\alpha \tag{6-6}$$

where β is defined as the sensor temperature coefficient.

6.2 Experiment Results and Discussion [51,52]

According to Eq. (6-6), the temperature dependence of the sensor head can be decreased by: 1) reducing the sensor effective bounding length (L_{eff}); 2) choosing sensor materials (tubing and bonding agent) with small CTEs; 3) reducing the size of the sensor (r). Obviously, thermal bonding techniques, especially the CO_2 laser direct bonding method, provide the best technical platform for fabricating low temperature-dependence sensors.

Figure 6.2 (a) shows the signal changes with temperature on a typical diaphragm-based sensor that was bonded with the thermal inter-medium layer bonding method. In this sensor, r=1.26mm, l_0=26.3μm, h=100μm, l_{eff} ~ 2.0mm, and P_0 =1.02x10^5(Pa). The sensor temperature coefficient β is about 4.06x10^{-3}(μm/°C). This result matches the theoretical result 3.47x10^{-3}(μm/°C) well. Owing to the thermal bonding techniques, the temperature effect is reduced significantly, comparing with that of the epoxy bonded sensor. (β~5x10^{-2} (μm/°C)), as shown in Figure 6.2 (b).

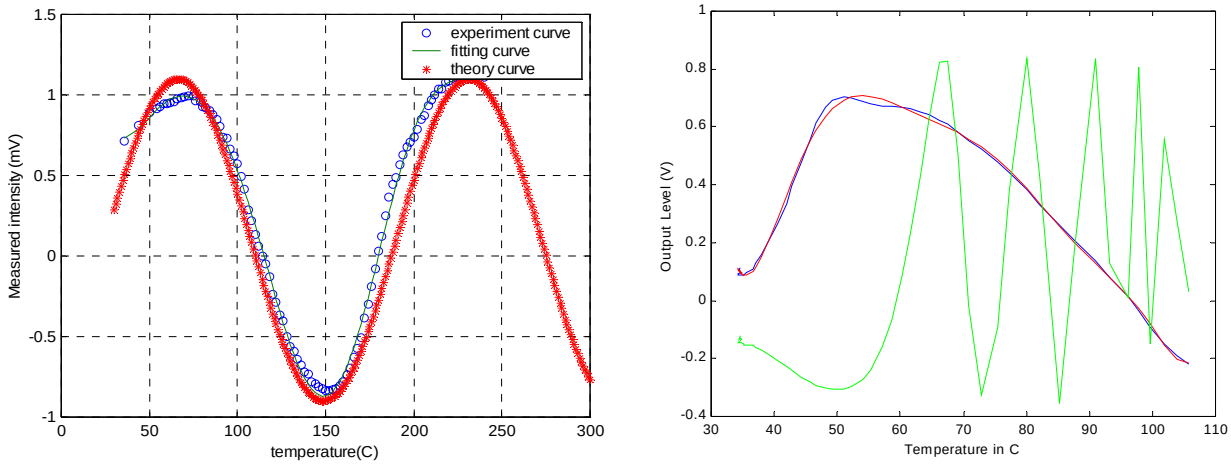

(a) (b)

Figure 6.2. Temperature dependence of various sensors. (a) thermally bonded sensor (b) Epoxy bonded sensor (green line) and thermally bonded sensor

6.3 Improvement of Sensor's Temperature Cross-Sensitivity

To further reduce the temperature dependence of the sensor, two methods are proposed and investigated.

1. Open air gap sensor structure

Because the temperature dependence of the sensors partially results from the air thermal expansion, an idea is, if we can somehow make the air gap open to the atmosphere, the air pressure changes due to temperature variations would be eliminated. Thus, the temperature coefficient would be reduced. A promising approach is to use a hollow fiber inserted into the air cavity during the sensor fabrication. Figure 6.3 shows the structure of a sensor based on this method, in which a tubing, with inside diameter (ID) 310um and outside (OD) 380 um, is thermally bonded with the lead-in fiber in a fused silica ferrule. In this sensor, r=1.26mm, l_0=15.3 μm, h=100 μm, and l_{eff} ~ 2.0mm. Figure 6.4 illustrates the temperature effect of the sensor. The temperature coefficient is β ~1.6×10^{-3}(μm/°C). Comparing with the previous result, the temperature effect is reduced further due to the elimination of the air thermal expansion.

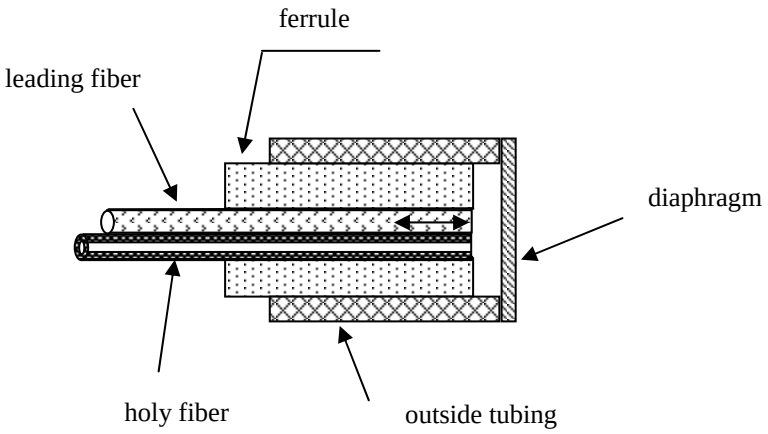

Figure 6.3 Structure of the open-air sensor head

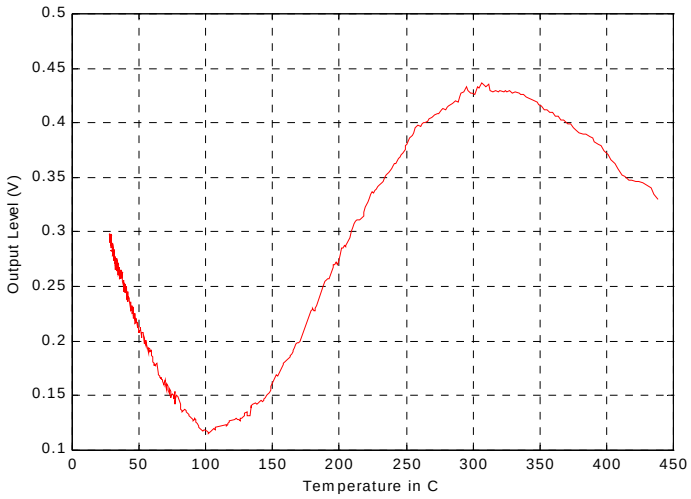

Figure 6.4 Temperature effect of the open-air sensor (β ~1.6x10^{-3}(μm/°C)).

2. External dynamic compensation method

Another promising approach is to compensate the temperature drifting by externally tuning the light wavelength. The concept is, when the cavity length drifts as temperature changes, the operating point of the sensor will leave the Q-point. If the wavelength can be automatically tuned, it is possible to 'draw' the operating point back to the Q-point.

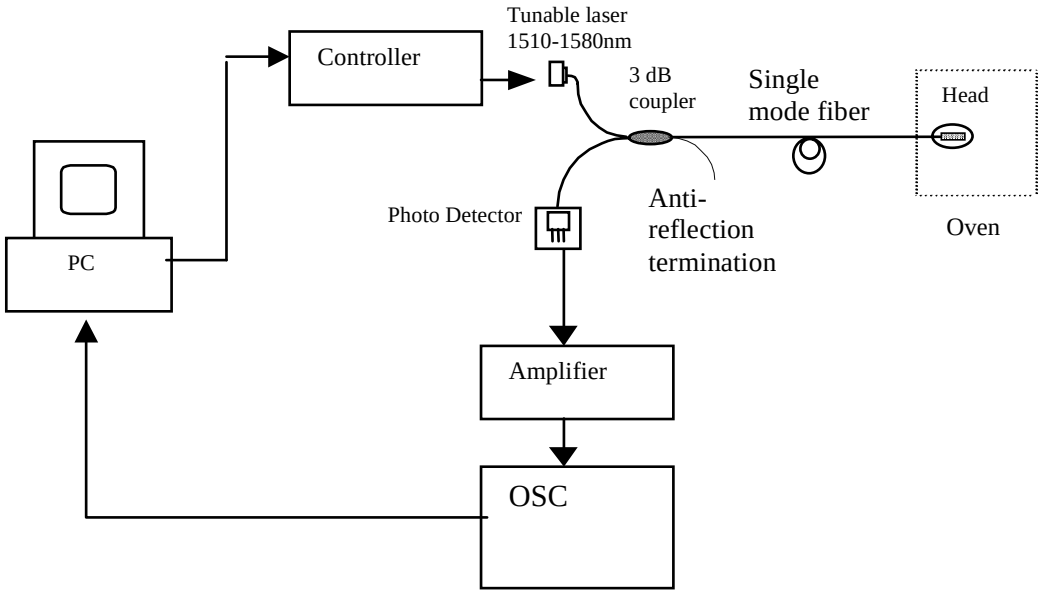

Figure 6.5. Experiment set-up for dynamically compensating the temperature effect

To prove the concept, an experiment is set up as shown in Figure 6.5. Instead of a SLED, a tunable laser (New Focus, Model 6328, tunable range 1510nm~1580nm) is used as the light source. The wavelength is tuned to maintain the sensor output at a constant level, during temperature changes. The experiment results, illustrated in Figure 6.6, indicate that the sensor has low response to the temperature changes, comparing to the sensor without compensation.

The drawback of this method is that only one channel of sensors can be controlled, which is not suitable for the PDs application where at least three channels of sensors are required at the same time. However, this drawback can be overcome by using a tunable filter at each channel to tune the wavelength back to the Q-point [72]. In this case, a SLED is still used as the light source.

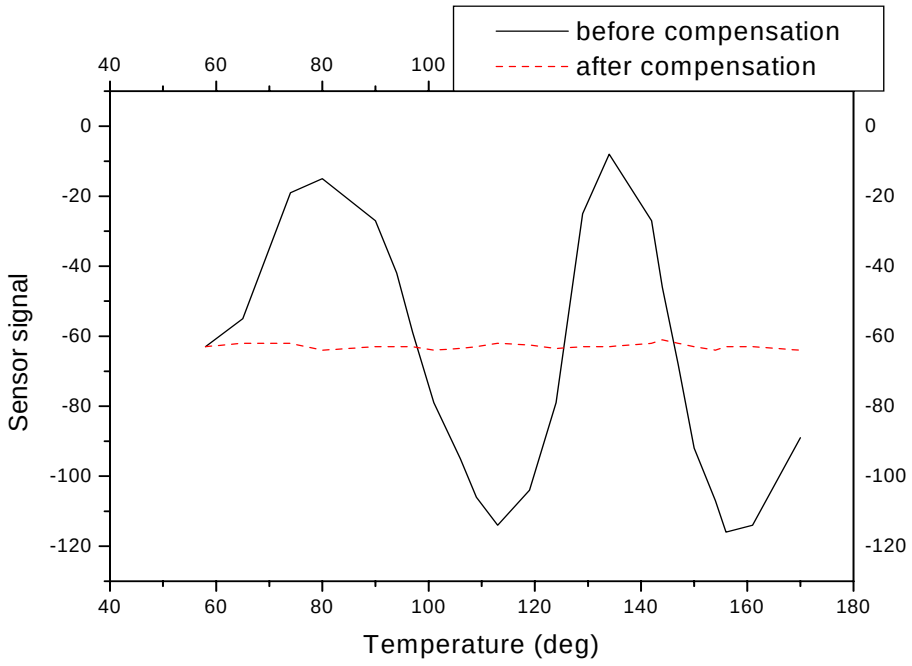

Figure 6.6 Sensor response results under external dynamic compensation

Chapter 7. DOFIA Sensor System Performance Evaluation and Calibration

Before a real application, it is necessary to calibrate a sensor to determine its performance. Broadly speaking, the performance characteristics of a sensor system include many, such as sensitivity, accuracy, repeatability, frequency response, zero offset, hysteresis, and reliability. Among them, the pressure sensitivity, frequency response, and the temperature cross-sensitivity are more important for an acoustic sensor system, especially for the PD application. This chapter will summarize the experiments and results associated with the performance and capability of the developed diaphragm-based fiber acoustic sensor system. The complete evaluation includes hydrostatic pressure sensitivity, capability to the aerodynamic pressure test, hydro-dynamic calibration and performance evaluation [51-54].

7.1 Hydrostatic Pressure Test

To validate the feasibility of applying the designed sensor to PD detection, we tested the pressure sensitivity of the sensor by applying known hydrostatic pressures generated by water columns. Figure 7.1 shows the experiment set-up for measuring sensor's hydrostatic pressure sensitivity. The sensor is mounted at the bottom of a tube filled with water. The water height beyond the sensor *h* can be adjusted with the pump. Therefore the pressure on the sensor surface $p = \rho gh$, where ρ is the water density, and g is the gravitational constant. By this approach, not only the sensor sensitivity, but also the water resistance of the sensor head, can be verified. Also, by increasing and decreasing the water height, the hysteresis of the sensor can be evaluated as well.

Figure 7.2 shows the curve of the sensor output as a function of the hydrostatic pressure. The curve marked with the squares (□) indicates the sensor output change in voltage with pressure increase (water column length), while the curve with the diamond marks (♦) shows the reverse procedure. These two curves match very well, which means that the

pressure hysteresis of the sensor is very small, owing to the fused silica's low hystersis nature. The measured sensitivity is estimated < 0.05 μm/psi, which is close to the theoretical result 0.035 μm/psi as defined by the diaphragm sensitivity.

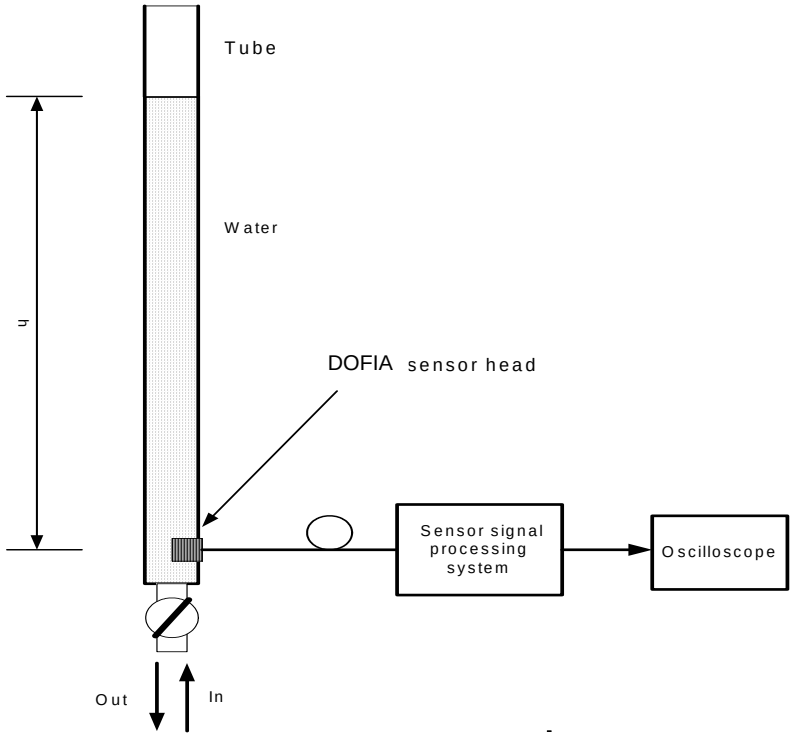

Figure 7.1 Experiment set-up for hydrostatic pressure test

(Sensor probe, a=1.25mm, h=100μm)

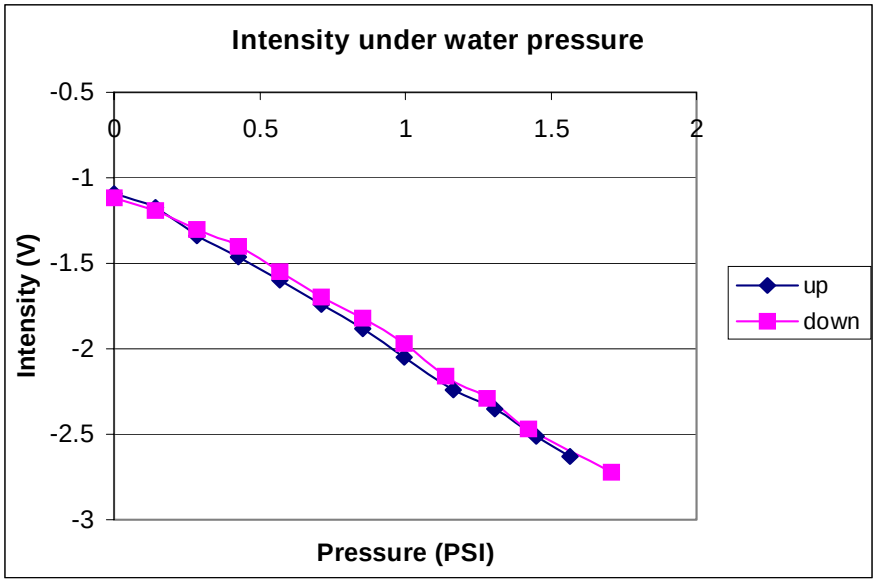

Figure7.2 Sensitivity test by applying a known hydrostatic pressure

7.2 Sensor Capability for Aerodynamic Pressure

In order to test the sensor response to dynamic pressure, the air shock method is used. A semiconductor pressure transducer (XCQ-080 Miniature IS ®, Kulite Semiconductor Products, Inc.), which is commonly used in gas turbine engine testing, was used for reference. Meanwhile, our sensor signal system was modified with a band-pass filter for low frequency measurement.

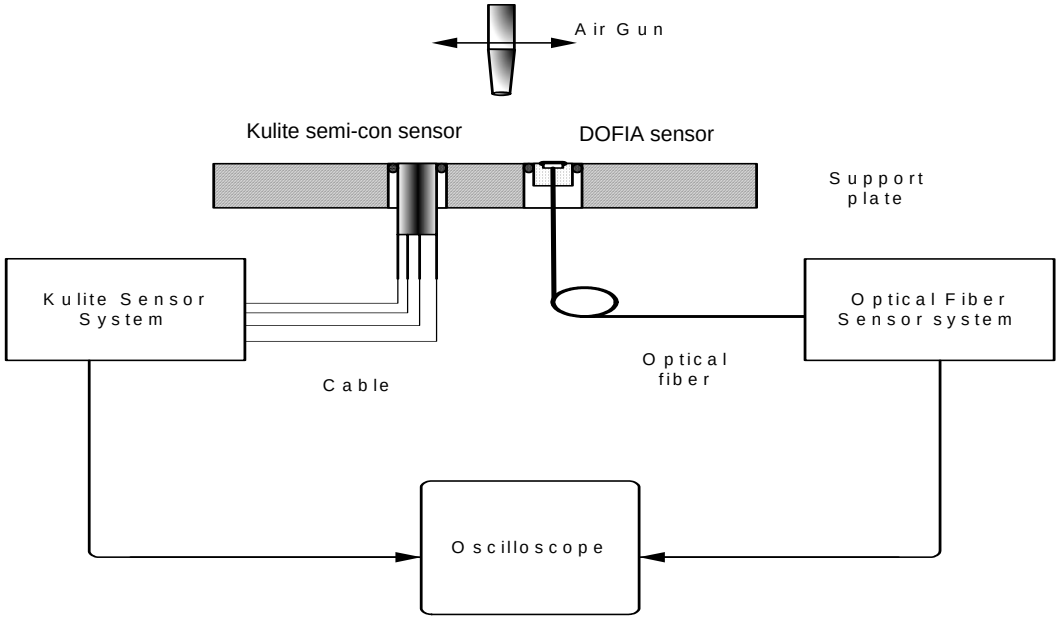

Figure 7.3. Experiment set-up for testing of DOFIA sensor response to the scanning air blows

In the first experiment, the fiber-optic pressure sensor was mounted with the Kulite transducer side by side in a fixture and subject to different unsteady flow-fields [53], as shown in Figure 7.3. An air jet with a steady stream of air was oscillated back and forth above the two sensors. Results were presented in Figure 7.4. The periodicity of the oscillation was about 5 Hz and the amplitude of the disturbance was about 4 psi. Figure 7.4 shows that the signal from the fiber optic sensor is very similar to that measured by the Kulite sensor. For most cases the amplitudes of the signals from the two sensors match well. In some cases there is difference between the two sensors' amplitudes. This may be due to the spatial variations in the pressure field generated by the air jet. Note

that the phase lag shown in Figure 7.4 is expected since the oscillating air jet would pass over one of the sensors first and then the other sensor. The reverse phase lag occurs as the air jet travels in the opposite direction.

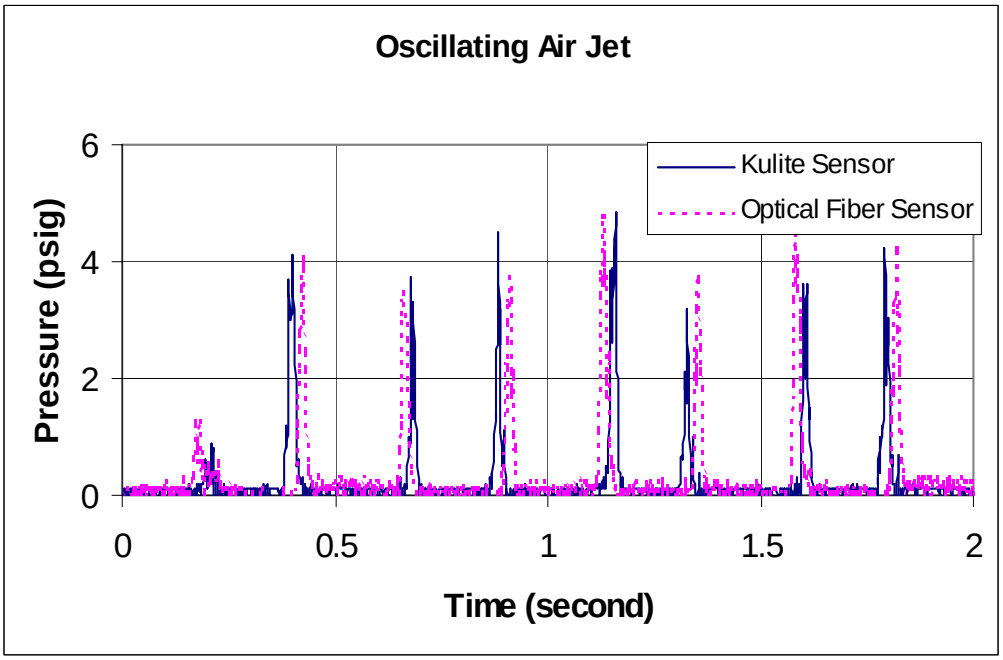

Figure 7.4. Comparison of the Kulite sensor and fiber optic acoustic sensor responses to the scanning air blows.

In the second test, the two sensors were again mounted side by side. A traveling air shock wave, generated from an air shock tube, was applied to test the response of the sensors. Figure 7.5 shows the experiment scheme for the shock-wave test. The results obtained are presented in Figure 7.6. The arrival of the shock wave at approximately 10 ms can be seen clearly. The pressure jump from the step change of the shock wave is about 12 psi. Figure 7.6 reveals that the response of the fiber optic sensor is similar to that of the Kulite transducer in terms of SNR(~40dB). There is some difference in the decay rate between the two sensors after the shock arrival (at about 10.5 ms). However, the difference in the signal may again be due to spatial variations in the pressure field applied. The event after the shock impingement, between 11 and 20 ms, also reveals that the trends of the signals from the sensors are quite similar. Figure 7.7 shows the FFT

spectrum of the shock wave signal taken by the fiber optics and Kulite sensors, where it shows that the frequency responses of both the sensors to the shock wave are similar.

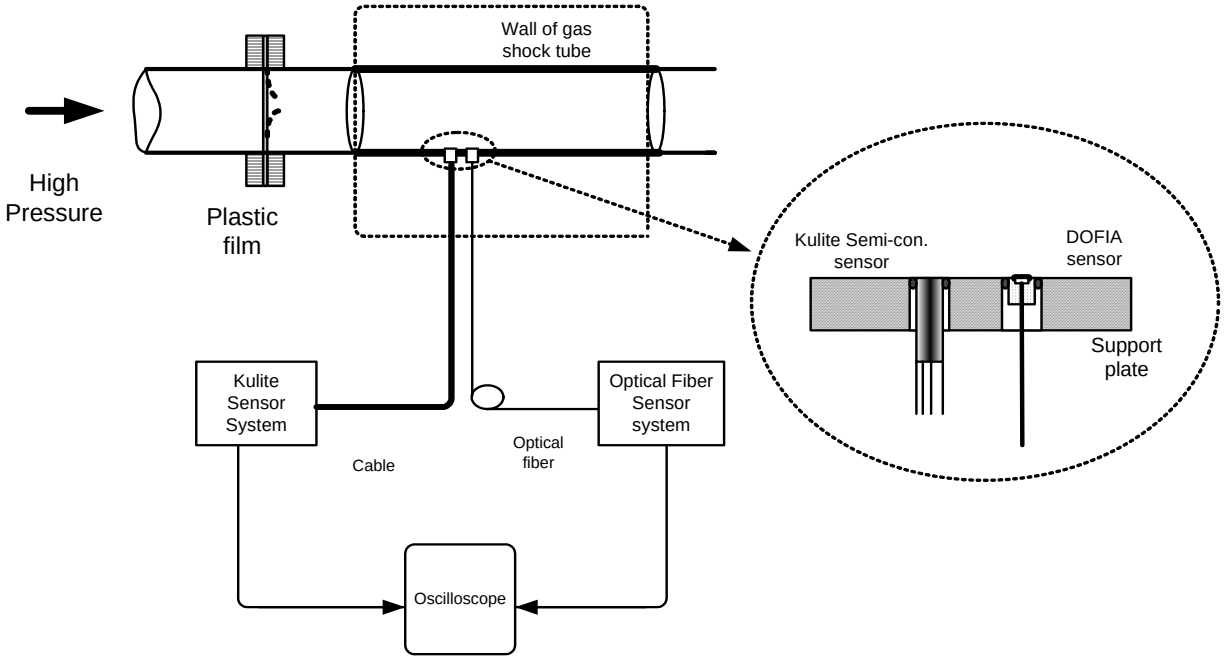

Figure 7.5. Experiment set-up for the shock wave testing using the DOFIA sensor

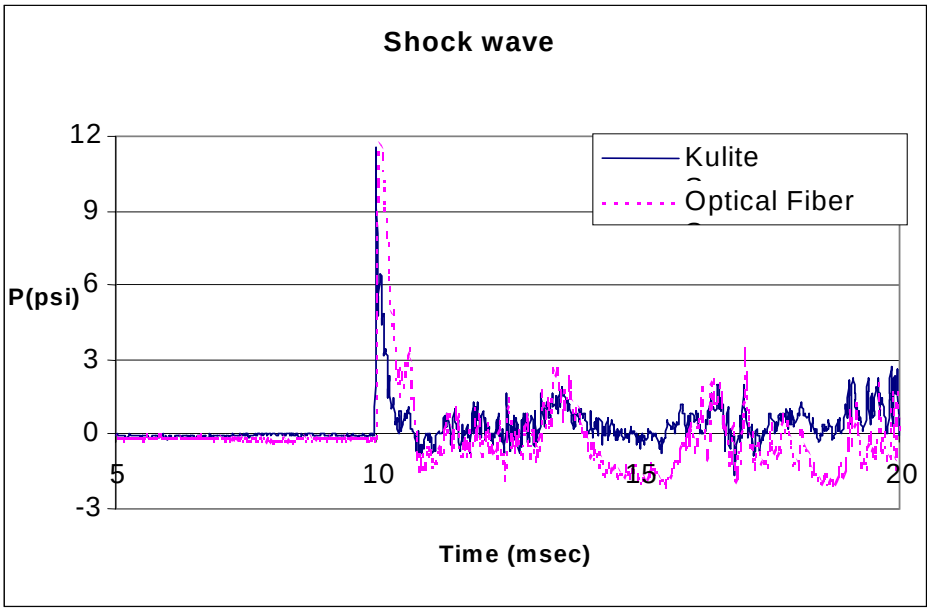

Figure 7.6. Comparison of the Kulite sensor and fiber optic acoustic sensor responses to a passing air shock wave

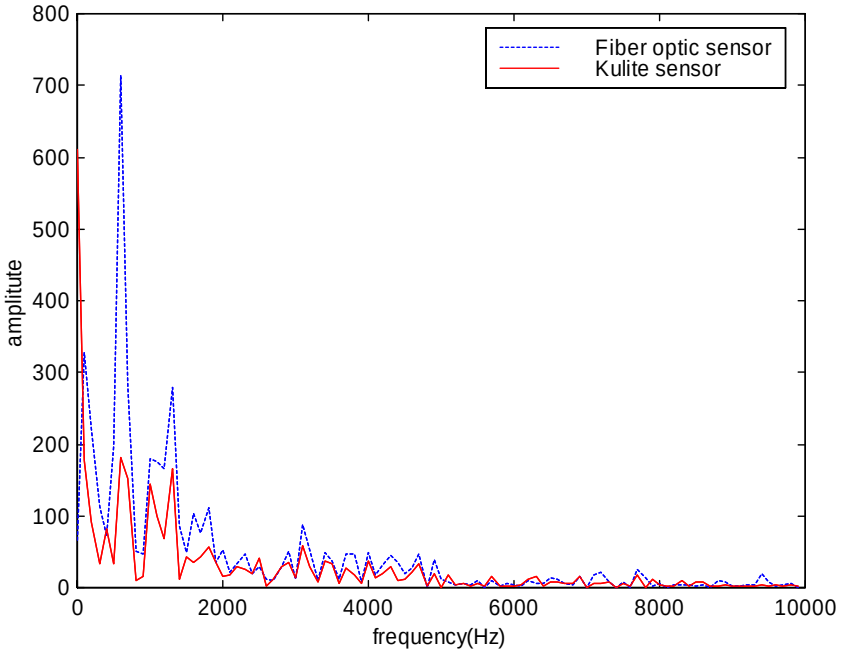

Figure7.7 Spectrum of the shock-wave

These experiment results show that the fiber-optic sensor has similar capability on the aerodynamic pressure testing to the conventional semiconductor pressure transducer.

7.3 Hydrodynamic Pressure Calibration and Test

7.3.1 Sensor calibration system for hydrodynamic test

In the previous work, the hydrostatic method was used for preliminary testing of the sensor's static sensitivity, and the air-shock method was used to test the aerodynamic response of the sensor. However, these methods cannot tell us the quantitative response of the sensor system for various frequencies in the hydro environment, especially in the PD range of 30kHz-300kHz. It is necessary and important to set up a calibration system with a whole range frequency capability. This system, shown in Figure 7.8, consists of four main parts: an ultrasonic source, an oil (or water) tank, a standard ultrasonic sensor and a signal processing unit. The ultrasonic source is driven by a pulser (C101-HV-2014, PAS Inc., NJ) and transducer (WDU, PAS Inc., NJ) to generate ultrasonic signals between 40 kHz~400kHz. A commercial piezo-electrical sensor (WDU sensor, PAS Inc.,

NJ) is mounted side by side with our calibrated fiber sensor. The signal from the piezo-electrical sensors is amplified by a pre-amplifier (1221A, PAS Inc. NJ). Figure 7.9 shows the photograph of the calibration system. Figure 7.10 depicts the frequency response of the calibrating sensor. In this way, it is possible for us to calibrate the pressure and frequency response of our sensor in the detecting frequency range.

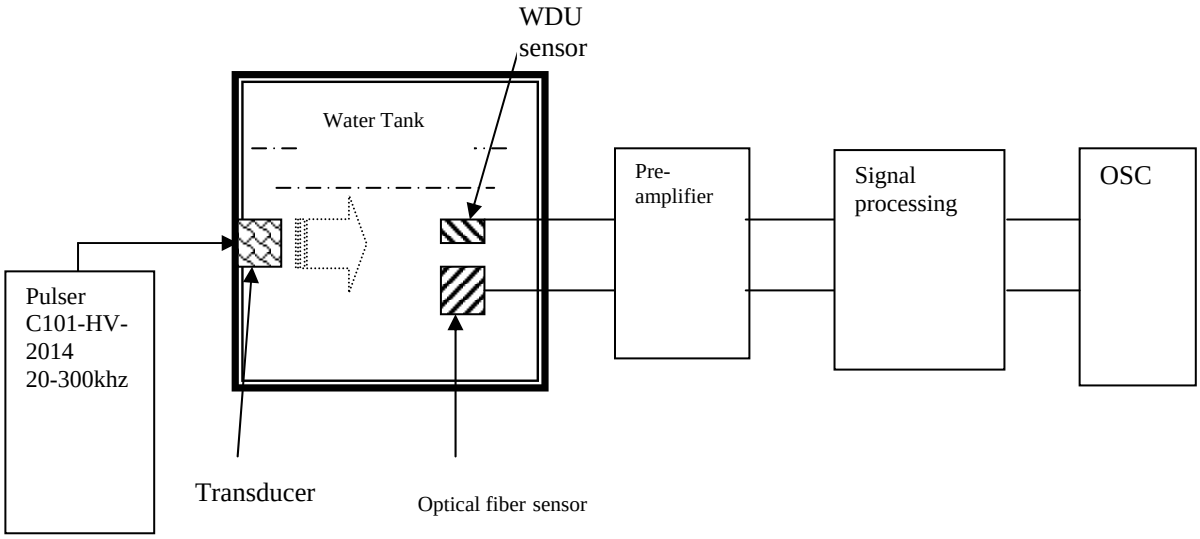

Figure 7.8 Schematics of Sensor calibration system

Figure 7.9 Photograph of the sensor calibration system

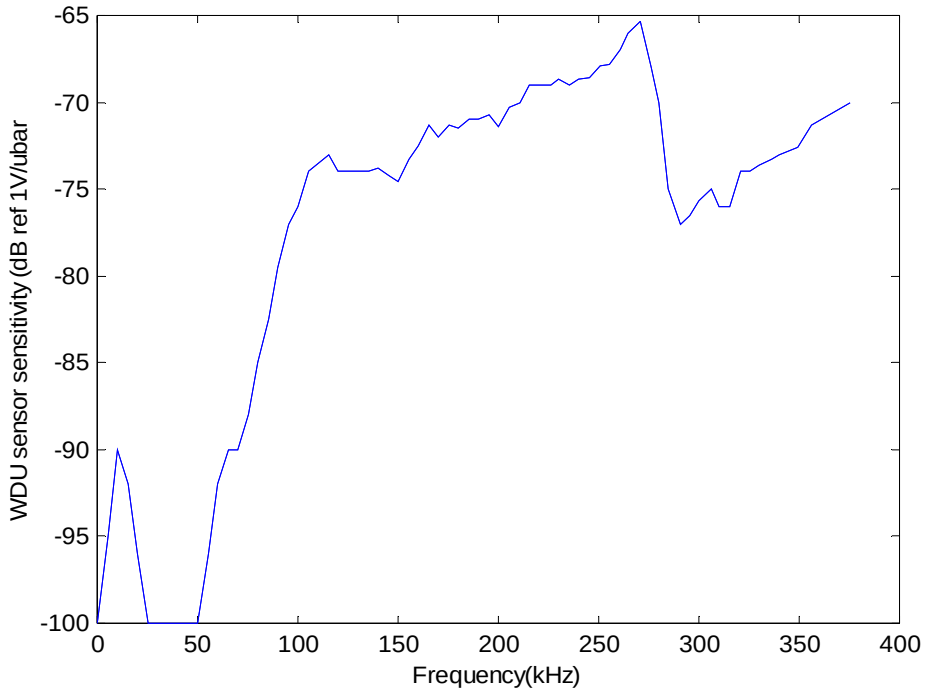

Figure 7.10. Frequency responsivity of the calibrating sensor (WDU-PAS Inc.)

7.3.2 System pressure resolution (P_{sys})

Figure 7.11 shows the response comparison between a fiber optic sensor (Curve 1) and the WDU piezo-electric sensor (Curve 2). In the fiber sensor system, r=1000 μm, h=100μm, λ_c=1.325μm, $\Re$ =0.9 (A/W), G = 6x10^6, R=R_0= 4% (Λ=1), I_0 = 0.002 W, and $\alpha \sim 0.1$. Curve A in the figure is the FFT spectrum of the signal by the calibration sensor. The frequency peak of the signal is about 248 kHz. According to the sensitivity spectrum of the WDU sensor shown in Figure 7.5 and assuming the pressures on the WDU and fiber optic sensors are the same, the acoustic signal pressure on the diaphragm surface of the sensor is about 0.9 psi, which causes 10V (peak-peak) output. Therefore, the measured responsivity is 11.1 V/psi, which is close to the theoretical result (14.0V/psi).

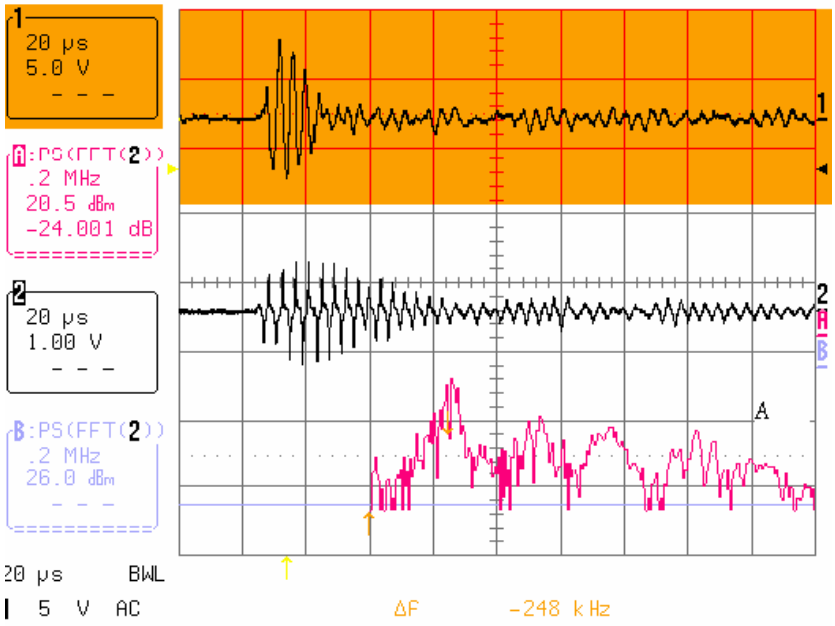

Figure 7.11 Sensor response and FFT spectrum, (curve 1, DOFIA sensor with $R=R_0=0.04$, and curve 2, WDU calibrating sensor.

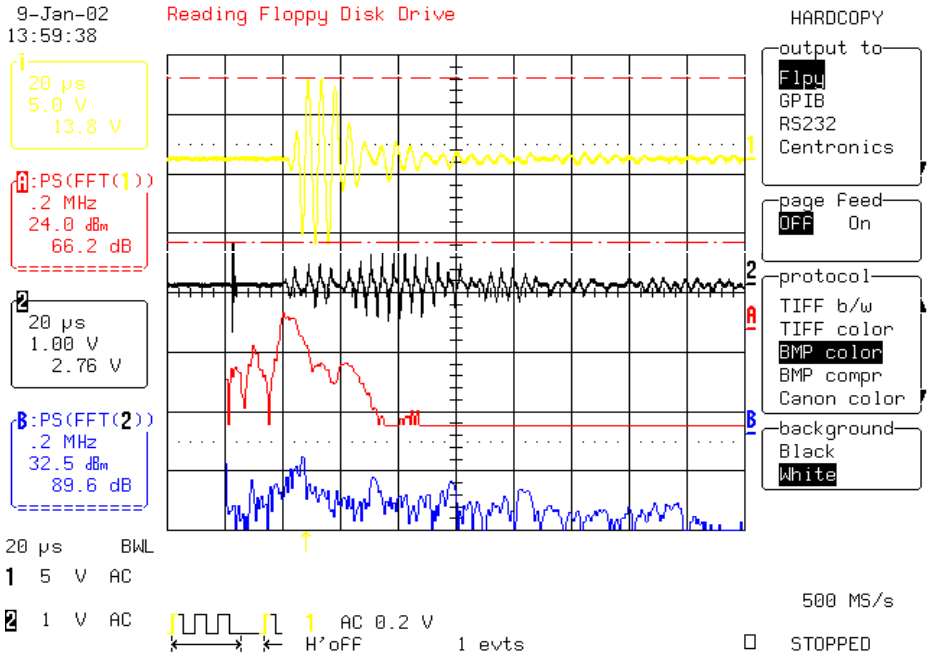

Figure7.12 Sensor response and FFT spectrum. (Ch.1 and A, DOFIA sensor with R=0.2, and Ch.2 and B, WDU calibrating sensor).

Figure 7.12 shows the sensor response of another DOFIA sensor with R=0.2. In this case, the acoustic signal pressure on the diaphragm surface of the sensor is about 0.709 psi, which gives 13.8V (peak to peak) output in the fiber sensor. Therefore, the measured responsivity is 19.46 V/psi, which is higher than the first sensor with no coating (R=0.04), but lower than the theoretical estimation (~60V/psi). The possible reason is that the cavity length is off the O-point or the Fabry-Perot cavity two surfaces are not parallel to cause additional optical loss.

Because our system's total noise is less than 30 mV (peak-to-peak value) as shown in Figure 4.11, the resolution of the first sensor system is about 2.7×10^{-3} psi, while the second sensor (with higher reflectance) has pressure a resolution about 1.5×10^{-3} psi.

7.3.3 System frequency response test and acoustic wave detection

The frequency response of the sensor system is another important issue for acoustic detection. In the frequency range of PDs (30kHz~300kHz), the system's frequency response mainly depends on the sensor head design, because the electric circuit has very flat response (~3 dB) over the frequency range of interest as shown in Chapter 5.

Using the piezo-electrical transducer, an acoustic wave is generated under water with first order frequency f=130kHz plus its harmonic components. Figure 7.13 presents the signal response received by the fiber optic sensor and the WDU sensor. The FFT results for each response show that the DOFIA sensor follows each frequency component very well. The amplitude difference on each frequency indicates that the fiber sensor has different frequency response from that of the WDU sensor.

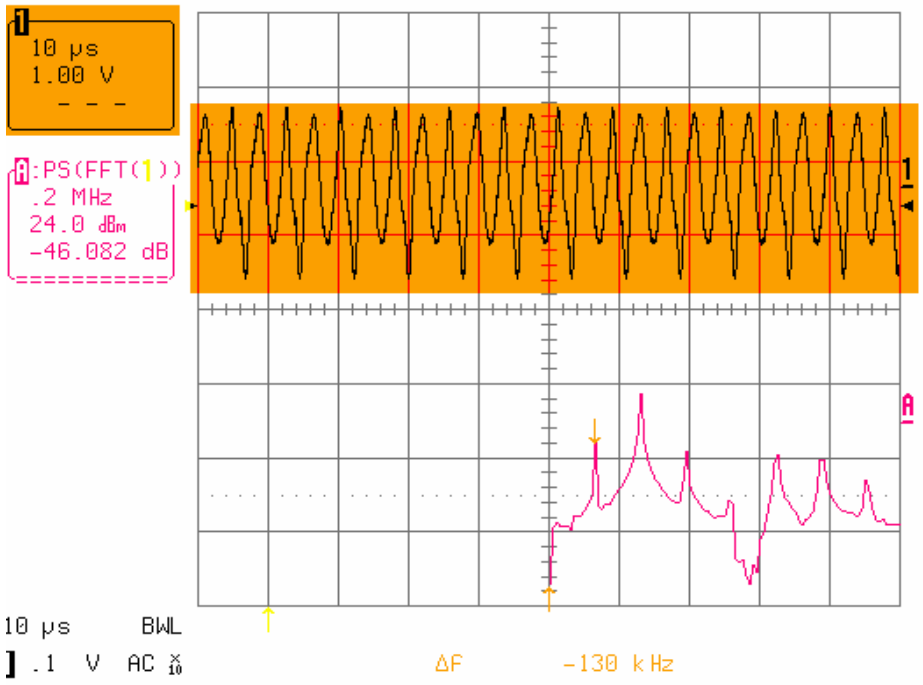

(a)

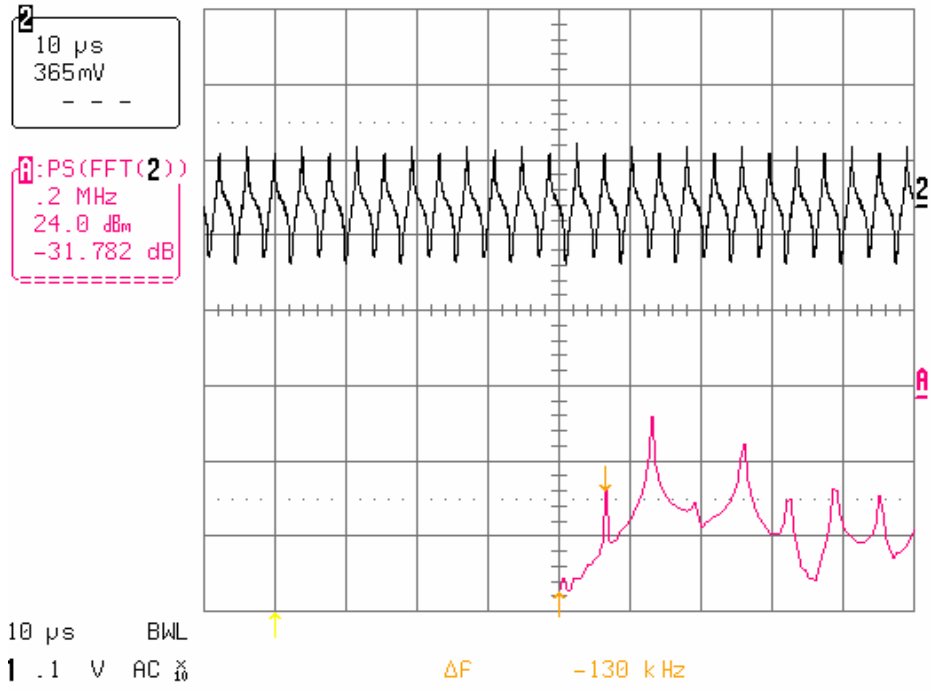

(b)

Figure 7.13 Response comparison between the DOFIA (a) and WDU (b) sensors to an acoustic emission

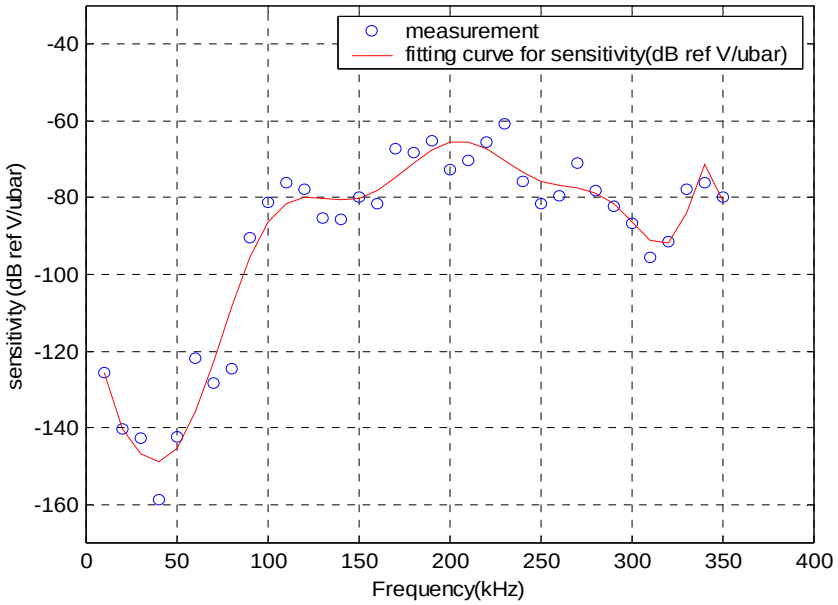

Figure 7.14 DOFIA sensor's frequency response

(r:1200μm, h:100μm, I_0 ~2mW, f_{00}=91 kHz in water)

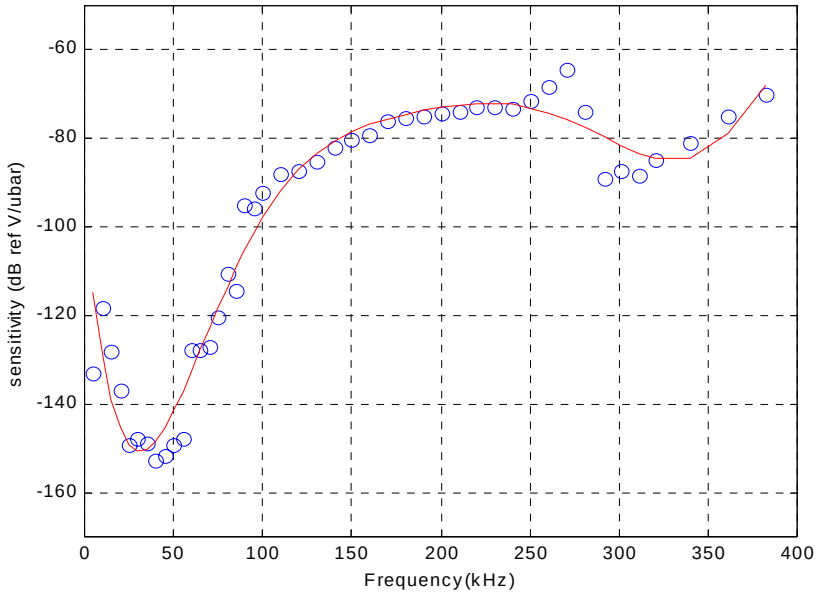

Figure 7.15 Frequency response of a broad-band sensor

(r:1200μm, h:254μm, I_0 ~2mW, f_{00}=91 kHz in water)

Figure 7.14 shows the typical frequency response of a sensor (r:1200μm, h:100μm, I_0 ~2mW, f_{00}=91 kHz in water). In the range of 50kHz~ 300kHz, it is noticeable that the sensor sensitivity is not flat, and the fluctuation is about 15dB. The frequency with the highest response is at ~ 210 kHz (~ -65dB ref V/ubar), and the second peak happens at 110kHz (~-75 dB ref V/ubar). As we already discussed in Chapter 2, these two peaks correspond to the first and second vibration modes of the diaphragm.

For comparison, Figure 7.15 shows the frequency response of another sensor with a diaphragm thickness of 254μm. The response is much flatter than that of the 100 μm-thick sensor over the frequency band, but with lower sensitivity. Sometimes we call the sensor with wider and flatter frequency response in the concerned band range as a 'broad-band' sensor, while the sensor with thinner diaphragm and higher pressure sensitivity in a certain frequency band as a 'narrow-band' sensor.

7.4 Sensor Capability for Detecting Propagating Acoustic Waves

Acoustic discharge detection is based on the detection of the mechanical signals emitted from the discharge. So far, the capabilities of the DOFIA sensor have been presented in terms of its sensitivity and frequency response to hydro-static, aerodynamic and hydrodynamic pressure. However, those results are not enough to show the sensor's capabilities for characterizing a propagating wave, like the acoustic emission generated by PDs. In this section, DOFIA sensors will be further evaluated in terms of the directional sensitivity, attenuation test, and location capability for the acoustic source.

7.4.1 Basic concepts of acoustics

Acoustic wave is a kind of elastic wave that propagates through a medium by means of wave motion, i.e., the propagation of a local disturbance through the medium. For a liquid, the disturbance produces compression and rarefaction in the medium. These local changes in pressure (p) result in local changes in density (ρ) and displacement of

molecules within the medium. The formal description of acoustic wave motion can be given by a general differential equation[73-74]:

$$\nabla^2 p = \frac{1}{v^2}\frac{\partial^2 p}{\partial t^2}$$

where v is the velocity of acoustic wave, and ∇ is the Laplacian operator. The elastic wave equation has a tensor form with three orthogonally polarized wave solutions for any direction of the propagation, with general form as:

$$p(r,t) = Ae^{(\omega t \pm \omega r / v)}$$

This equation shows how a pressure wave with a frequency $\omega = 2\pi f$ varies with time and location. At any given time, the pressure repeats itself with a space interval given by $\lambda = v / f$.

When a wave propagates through a structure, the intensity of the wave decreases as a function of distance from the source. This results from several mechanisms including geometrical spreading of the acoustic wave, acoustic absorption (conversion of acoustic energy to heat), and scattering of the wavefront.

Usually partial discharges in transformer can be considered as a point source, the acoustic emission generated by a PD has spherical wavefronts as a result. Thus the intensity would attenuate in proportion to the increasing surface area,

$$I_0 \propto \frac{1}{r^2}$$

where r is the distance to the source. Losses in a homogeneous medium can be divided into three basic types: viscous losses, heat conduction losses, and losses associated with molecular exchanges of energy. The losses in the medium can be expressed as

$$I(r) \propto e^{-\alpha r}$$

where 2α is the intensity absorption coefficient.

Obviously, by tracing the loss of an acoustics wave in the medium (α) and the wave frequency (*f*), it is possible for us to study the property changes of the medium, which is the purpose of PD detection in the power industry.

7.4.2 Acoustic wave attenuation test

Figure 7.16 shows the experiment results of the sensor intensity as a function of the sensor distance to the acoustic source. The solid curve in the figure indicates the theoretical effects of increasing spherical wavefront area, which can not fit with the real curve. The reason of the mis-match may be that, the acoustic source is not an ideal point source in such short distance, so the wavefront is actually close to a plane wave, instead of a spherical wave. The dash line in Figure 7.16 is the exponential fitting curve of the measurement data, which gives the absorption coefficient $\alpha \sim 0.0626 / cm$.

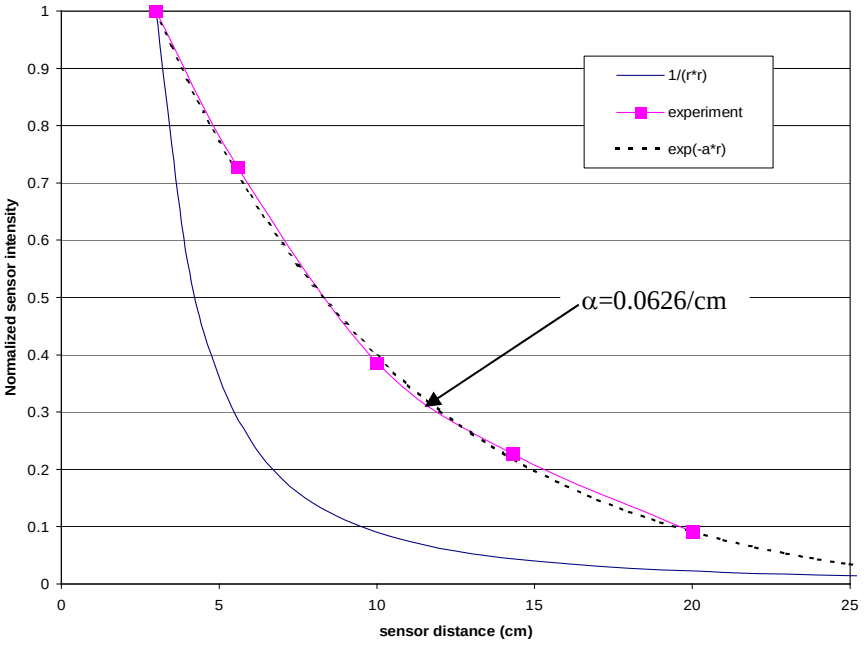

Figure7.16. Signal attenuated with increasing distance to the acoustic source *(f=230kHz)*

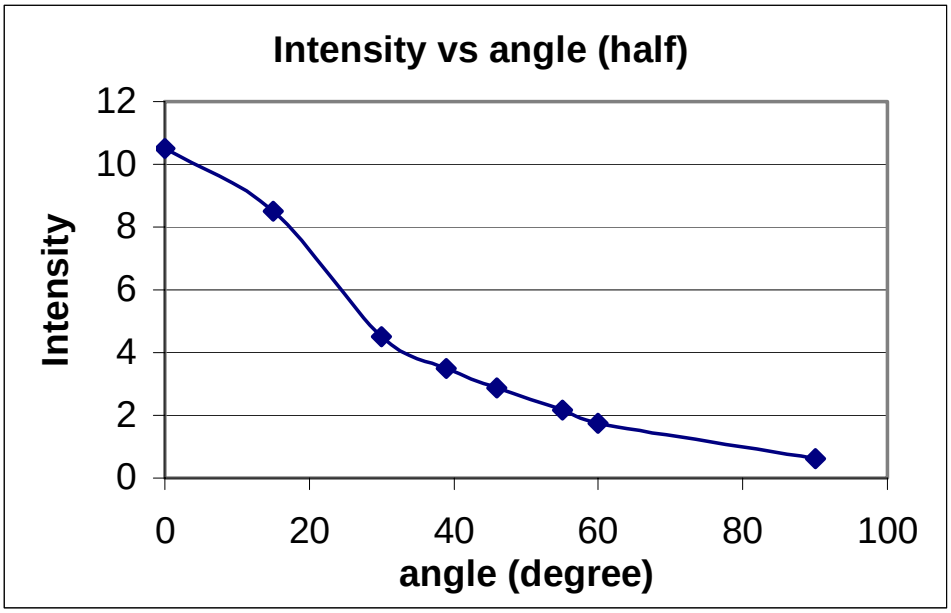

Figure 7.17. Directional sensitivity of the DOFIA sensor (*f=230kHz*)

7.4.3 Sensor directional sensitivity test

For the purpose of locating a PD source, the sensor should be able to respond to the acoustic wave at a wide range of incidence angles. The directional sensitivity of the sensor head depends on the sound frequency and wavelength, and on the geometric structure of the sensor. If the sound wavelength is less than the diameter of the sensor head, the directional sensitivity would not be isotropic. The higher the frequency, the greater the effects of the incidence angle on the response. For example, the velocity of acoustic waves in transformer oil is about 1400m/s. For a 100 kHz acoustic wave, the wavelength is therefore 14mm, while for 300 kHz the wavelength is only 5mm. It is obvious that the sensor head should be designed as small as possible in order to decrease the directional sensitivity (larger receiving angle range). Figure 7.17 shows the directional sensitivity of our sensor, which shows that this sensor has ±~30 degree sensitivity (6 dB).

7.4.4 Acoustic source location experiment

Figure 7.18 shows the experiment set-up for the acoustic source location, in which three DOFIA fiber sensors and a WDU sensor are mounted in a water tank with different distances to the common source. In Figure 7.19, the fact that all sensors responding to the source illustrates the difference of arriving time of acoustic waves to the sensors from the source, labeled by the arrows. The distances to the source from sensor OS-1 and OS-2 are given (L1=14cm, L2=15cm). The other two sensors (OS-3 and WDU) are put in the tank arbitrarily.

According to Figure 7.19, the arriving time differences ($\Delta t_{ij}= t_j - t_i$) of acoustic waves to the sensors are: $\Delta t_{12}= t_2 - t_1$=8us, $\Delta t_{13}= t_3 - t_1$=16us, $\Delta t_{1\text{-}wdu}= t_{wdu} - t_1$=14us. Assuming the acoustic wave propagates at the same speed at different angles in the water, the acoustic wave speed is about 1250m/s, which is in the range of the reference results (1000-1500m/s). The distances of OS-3 and WDU sensor are calculated as 16cm and 15.75cm, which is similar with the measurement results of 16cm and 15.6cm. The location resolution is less than 2mm. This experiment also indicates that: with multiple sensors given exact positions in the space, it may be possible to locate a PD source in a transformer.

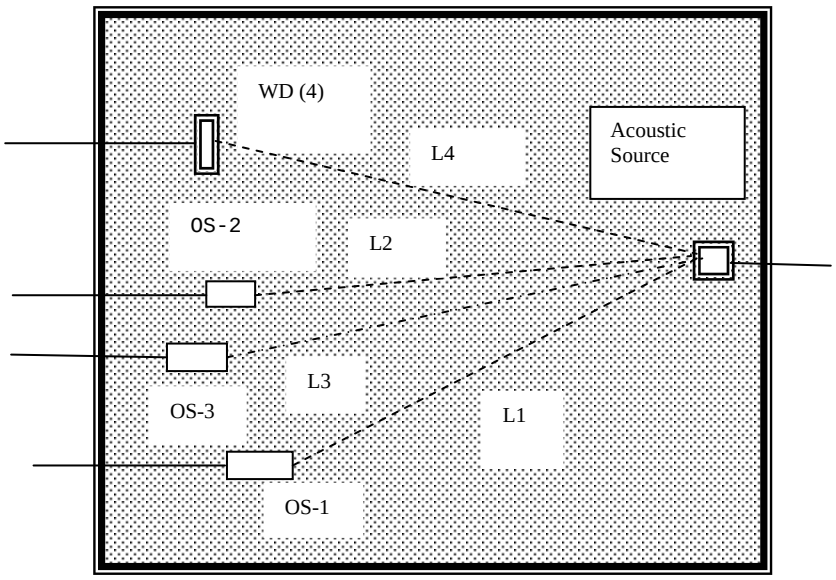

Figure 7.18 Acoustic source location experiment using optical fiber sensors

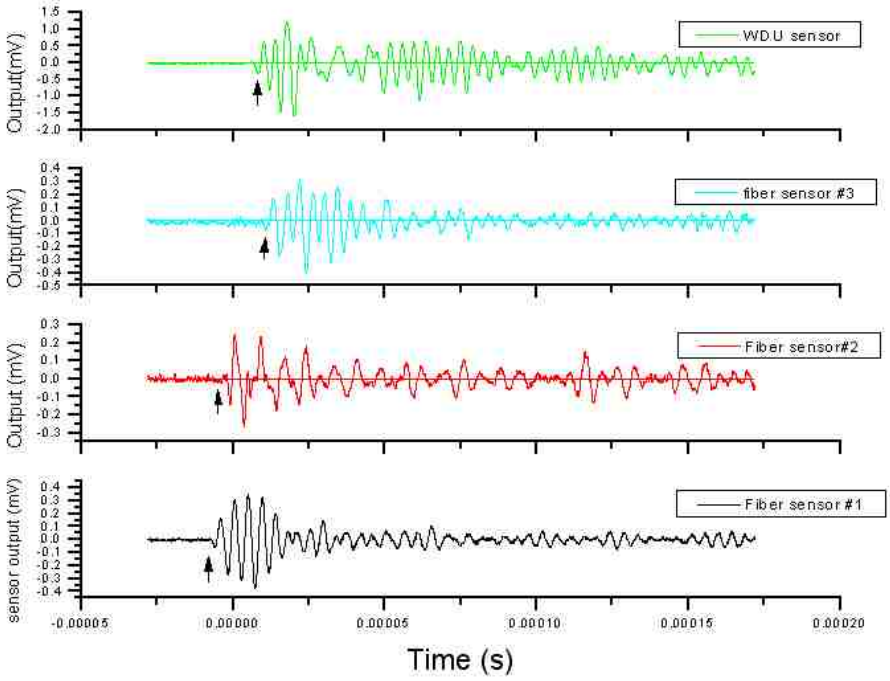

Figure 7.19 Sensors response to the same source in the water tank

Chapter 8 Sensor Application for Partial Discharge Detection

8.1 Laboratory Setup for the Simulation of PD Acoustic Waves

In order to investigate the feasibility of real PD detection with a DOFIA sensor, a simulation PD detection system was set up in laboratory, using a car starter to generate PD emission.

The PD device shown in Figure 8.1 uses a spark plug connected with an ignition coil and a 12V battery. Both are connected to the control switch. The voltage applied to the ignition coil will be built up to about 10KV. Partial discharges will occur between the electrode tips in the spark plug randomly, and generate acoustic waves. Figure 8.2 illustrates the components of the whole system, including the PD devices, the fiber sensor system and the PZT sensor system.

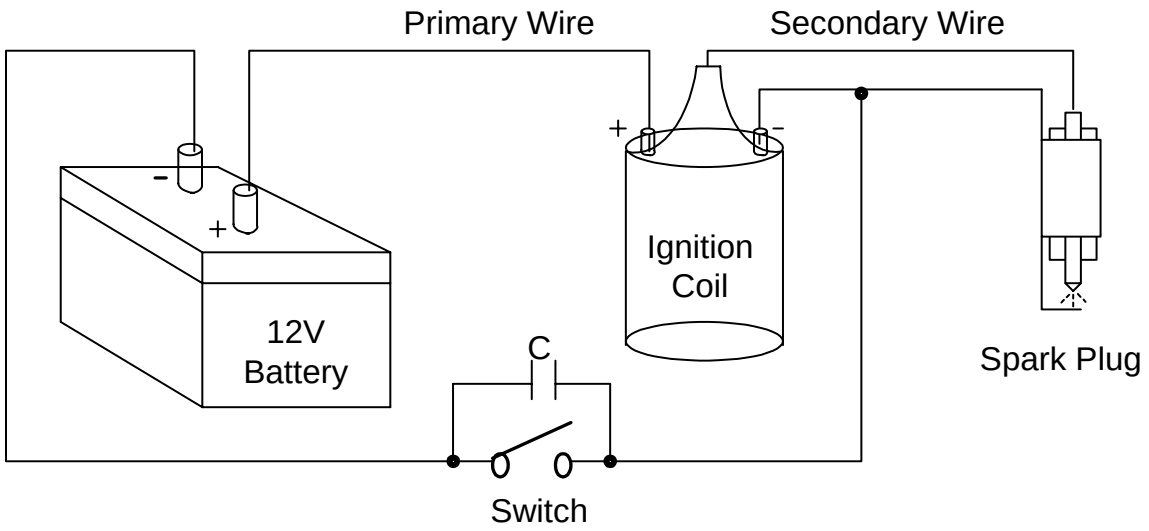

Figure 8.1 Partial discharges device set-up

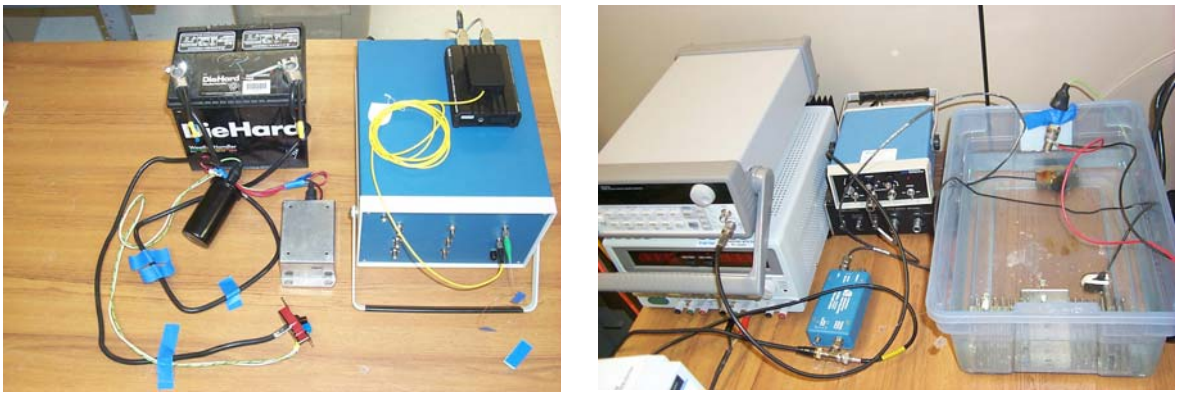

Figure 8.2 Photograph of the PDs simulation systems

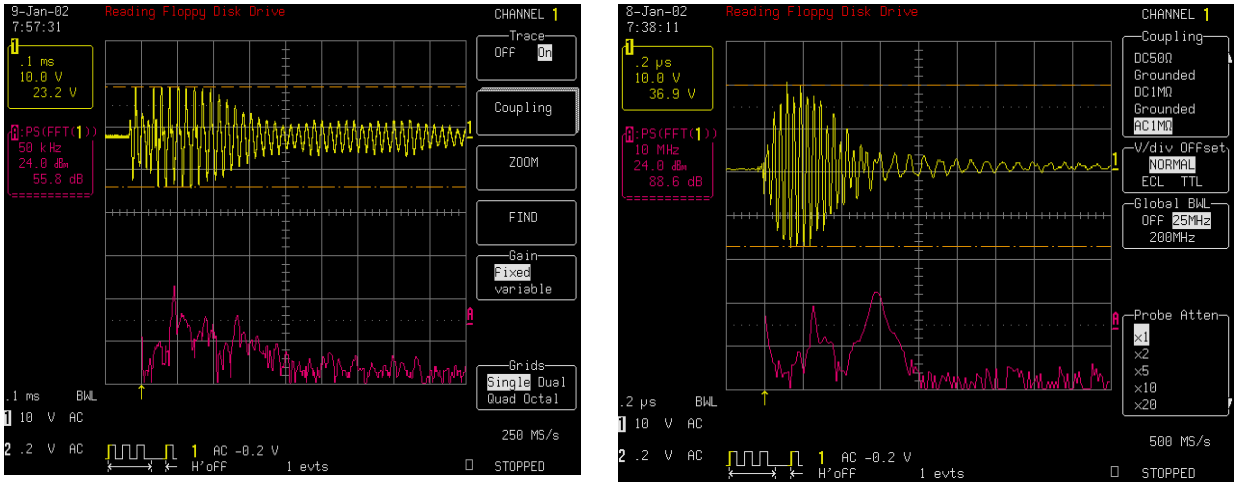

(a) (b)

Figure 8.3 (a) Partial discharge detected by the fiber sensor. Conditions: Optical power is 1.5mW, and the sensor is 0.5cm from the spark plug. (b) Measured with the PZT sensor. The PZT sensor is 2cm from the PD source box.

Figure 8.3 (a) shows a DOFIA sensor response to a pulse caused by partial discharges. The signal has a peak frequency at 47kHz and SNR 61dB. However, the partial discharges signal detected by the PZT sensor shows a totally different shape, as shown in Figure 8.3(b). From the results of the FFT, besides the 47kHz frequency, the PZT sensor also receives two tones strongly at 12MHz and 29MHz.

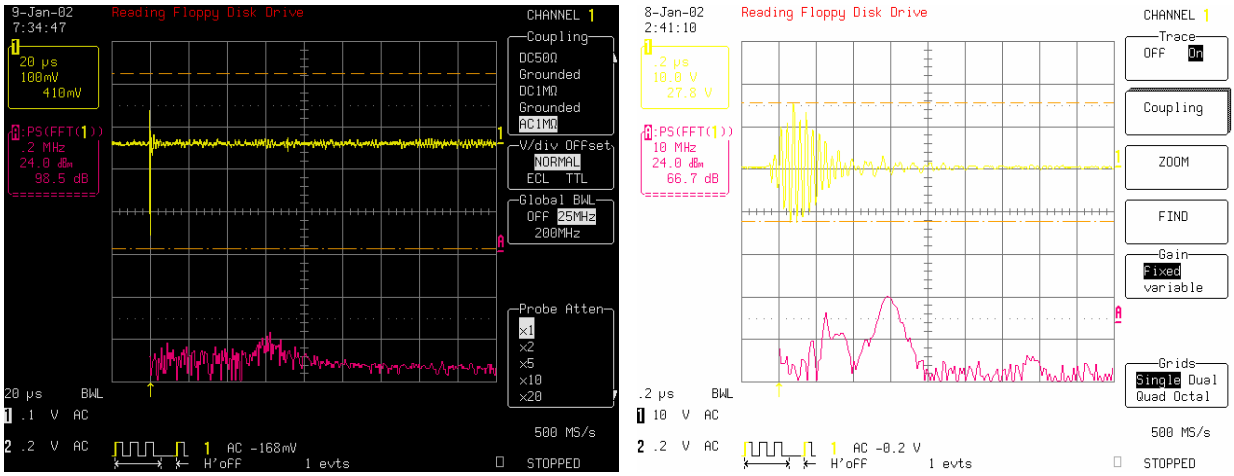

Figure 8.4 The fiber sensor and PZT sensors are far away from the enclosed PDs source (a) Partial discharge detected by the fiber sensor. Conditions: the same as those in Figure1, except that the light source is turned off. (b) Measured with the PZT sensor. The power supply to the preamplifier is off and the PZT sensor is about 30cm from the PD source box.

To figure out the cause of this difference, the DOFIA sensor and the PZT sensor are put far away from the aluminum tank (with spark plug inside). After partial discharges generated, the fiber sensor gets a very weak pulse (~200mv) shown in Figure 8.4 (a), which does not have any vibration. FFT results indicate what the fiber sensor gets is just broadband noise. However, the response of the PZT sensor as shown in Figure 8.4(b), is almost the same as that received in the enclosure, shown in Figure 8.3. When a partial discharge happens, it generates both acoustic waves and electromagnetic waves propagating through the medium. The acoustic waves will be absorbed and attenuated in the air quickly, while the electromagnetic waves will induce interference to cables, circuits, and even the PZT sensor. Therefore, what the sensor outside the tank gets is actually EMI caused signal. In other words, the signal obtained by the fiber sensor in Figure 8.3 (a) is the real acoustic signal generated by the PD, while the PZT sensor can not distinguish the acoustic signal from EMI. This proves that the optical fiber sensor has its unique advantage over the PZT sensor on PD detection.

8.2 Field Test Results and Discussions

To further validate the feasibility of applying DOFIA sensors to detect and locate partial discharges inside power transformers, a field test was performed at J.W. Harley Inc., Twinsburg, Ohio, where a specially designed testing facility was available to study the partial discharge phenomena inside a power transformer.

As shown in Fig 8.5, a DOFIA sensor head was immersed in the transformer oil with its diaphragm toward the needle-plate partial discharge generator. The sensor probe was connected to the signal demodulation unit through a single mode fiber cable and a FC connector. After the photo-detection and the signal processing, the output data was digitized and recorded through a digital oscilloscope.

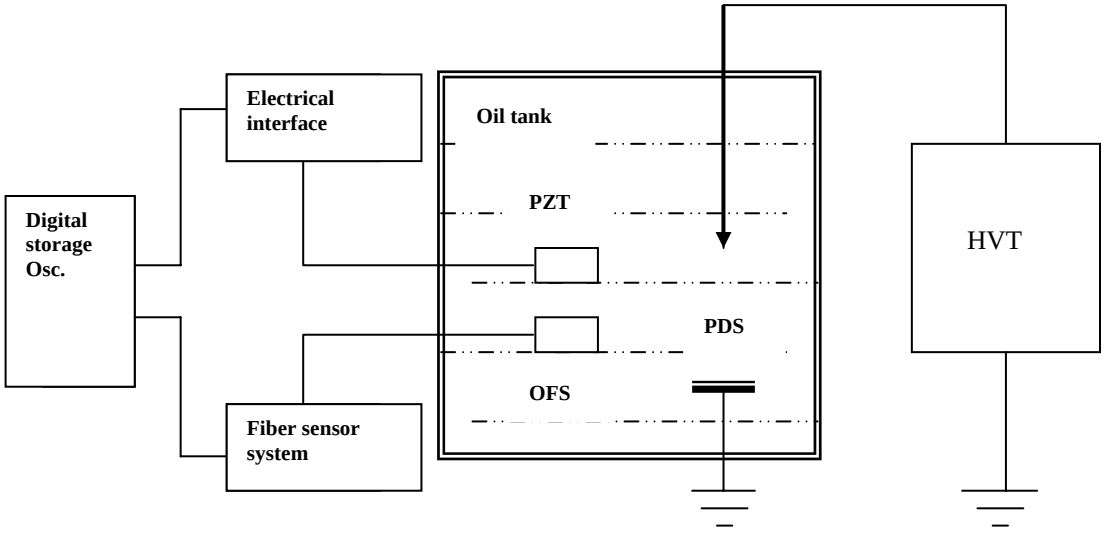

OFS: Optical fiber sensor, PZT: physical acoustic sensor,
PDS: partial discharges sources, HVT: high voltage transformer

Figure 8.5 Partial discharge test setup at J.W. Harley Inc. at Twinsburg, Ohio, U.S.A.

Figure 8.6 (a) shows the facilities of the power transformer for the PD detection. Figure 8.6 (b) illustrates the prototype fiber optic sensor system setup beside the partial discharge simulator, and Figure 8.6 (c) shows the fiber sensor probe immersed in the transformer oil and pointed to the needle-plate partial discharge generator.

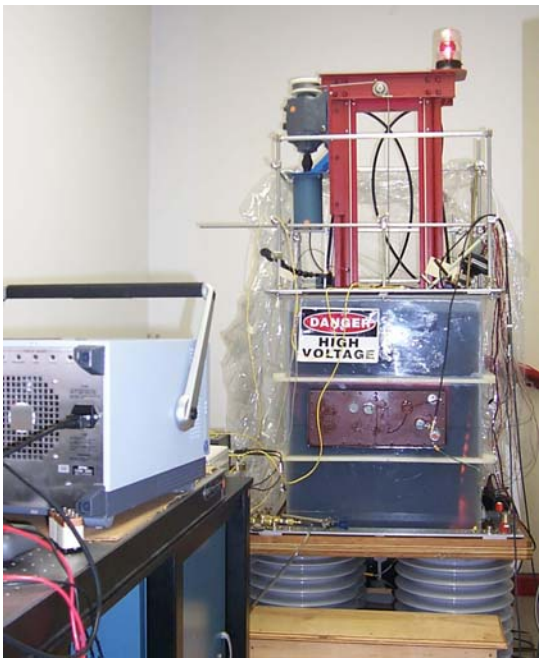

(a)

(b)

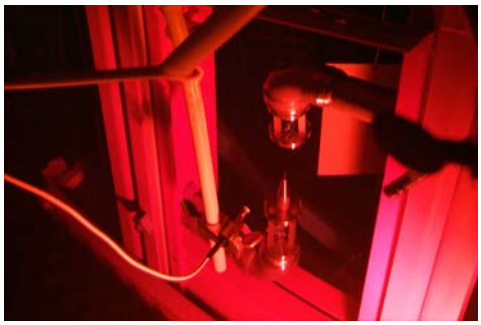

(c)

Figure 8.6. Test setup for the field-testing performed at J.W. Harley Inc. at Twinsburg, Ohio a). Partial discharge simulator, b). Prototype fiber optic sensor system, c). Fiber optic acoustic sensor probe immersed within transformer oil close to the needle-plate discharge generator.

The test was performed in comparison to the PZT acoustic sensor located side by side to the DOFIA sensor probe. Their typical output signal upon partial discharges are given in Figure 8.7, where, (a) is the output from the physical acoustic sensor and (b) is the output from the fiber optic sensor. As we can see immediately, the two sensors' outputs resemble each other in detail. Both outputs indicate that the acoustic signal generated by a partial discharge is comprised of sinusoids with gradually decreasing amplitudes. The two acoustic signal pulses detected by the two sensors have the same time duration of about 8μs. This means that both the sensors detected the partial discharge acoustic signal at the frequency of about 120 kHz, which is the typical frequency of the partial discharge acoustic signal.

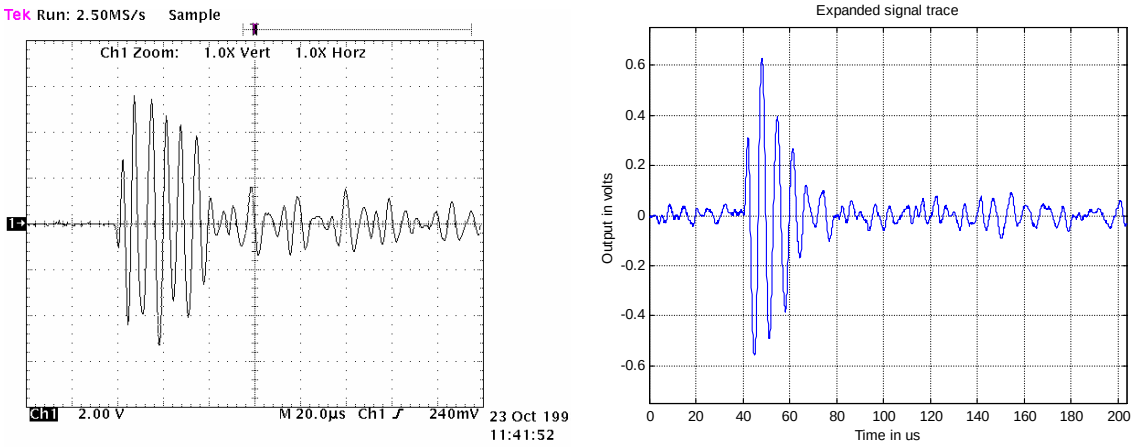

(a) (b)

Figure 8.7 Typical partial discharge acoustic signals detected by the fiber optic sensor and the Physical Acoustic PZT sensor. (a), Physical Acoustic PZT sensor output; (b), Fiber optic sensor output at 10cm away from the partial discharge source.

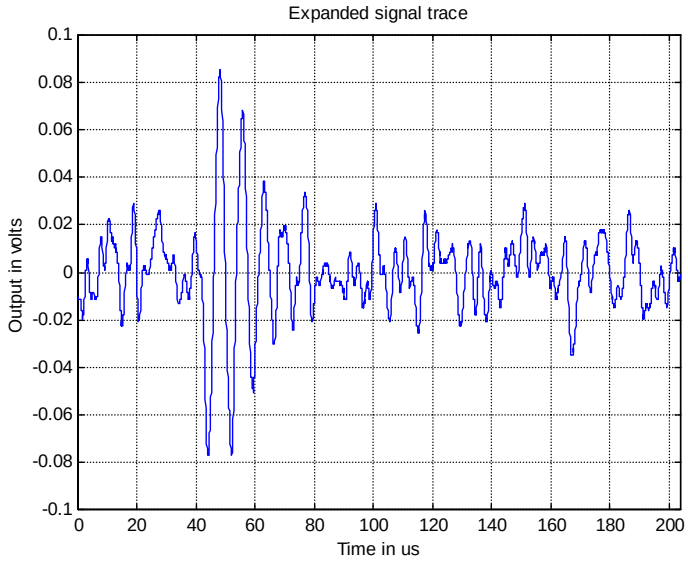

Figure 8.8. Fiber optic sensor output at 50cm away from the partial discharge source

To test the sensitivity of the fiber optic sensor, we located the sensor probe at different distances with respect to the needle-plate partial discharge generator. The fiber optic sensor was able to pick up the partial discharge acoustic signal even when it was located far away from the partial discharge source. Figure 8.8 shows the fiber sensor output when located at half meters away from the partial discharge source. Compared with the signal

shown at Figure 8.7 (b), the acoustic signal remained the same properties except that its amplitude decreased as the distance became larger.

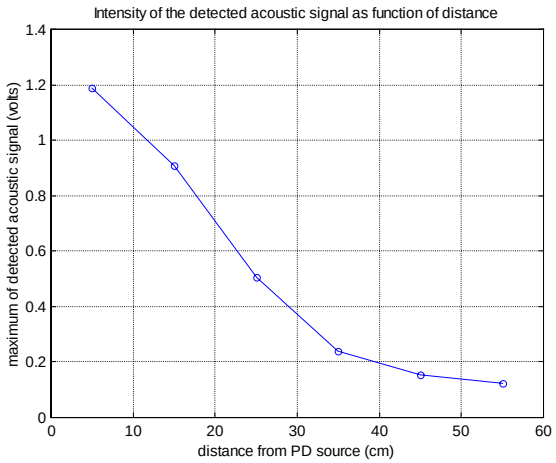

Figure 8.9 Amplitude dependence on the distance between sensor location and the PD source

When an acoustic wave generated by a partial discharge travels in the insulation medium of a transformer, its amplitude will attenuate over distance. Therefore, one of the possible methods to locate the site of the partial discharge source is to monitor the amplitude attenuation of the received acoustic signals. We measured the amplitudes of the acoustic signals detected by the fiber sensor at different distances away from the needle-plate partial discharge generator. The results are shown in Figure 8.9, which indicate that the amplitude of the acoustic signal has a strong dependence on the physical distance between the sensor and the PD source. The largest distance tested was 55cm that was limited by the size of the oil tank of the testing facility.

Chapter 9. Summary and Conclusions

For the purpose of developing a new highly-sensitive and reliable fiber optical acoustic sensor capable of real-time on-line detection of acoustic emissions in power transformers, this dissertation presents the comprehensive research work on theory, modeling, design, fabrication, instrumentation, noise analysis, and performance evaluation of a diaphragm-based optical fiber acoustic (DOFIA) sensor system. This chapter summarizes the major achievements and conclusions obtained during the research.

1. Theoretical fundamentals of the DOFIA sensor

First, based on the principle of multi-beam interference, the theory of fiber optical interferometric fringes is built up, which is applicable for any kind of Febry-Perot interferometric sensor with arbitrary surface reflectance. The analysis shows that, a) raising the surface reflectance will increase the interferometer sensitivity, but will reduce the fringe visibility due to the signal bias. b) the cavity length should be kept as small as possible and within the operating range, in order to maintain higher sensor visibility, and lower coupling loss.

Moreover, based on the model of a circular plate clamped at boundary, the diaphragm dynamic vibration theory is introduced. The discussion on the solution of motion equations of the diaphragm leads to the expression of the frequency response and pressure sensitivity of the diaphragm-based sensor. The analysis also points out that two types of sensors (narrow-band and broad-band) can be designed and applied for different practice areas.

The optical interference theory and the diaphragm vibration dynamics govern the operation of the DOFIA sensor. Combining these two principles, the pressure sensitivity and resolution of the acoustic sensor system are analyzed quantitatively, which provides a clear guidance for the practical design of the DOFIA sensor system. Based on the

developed theory, the medium-fineness interferometric sensor is introduced since it has higher sensitivity (10^{-3}psi) as well as the broad and flat frequency response.

2. Sensor probe fabrication and system instrumentation

One of the major accomplishments reported in this dissertation is the design and fabrication of an DOFIA sensor probe that can meet the requirements for acoustic wave detection. For the first time, standard semiconductor processing technologies, such as photolithography, dry-etching, and film-deposition, are used to fabricate the micro-caved diaphragm (MCD), which is the key sensing element in the DOFIA sensor probe. This technique provides the technical platform for the diaphragm-based sensor fabrication and clearly shows advantages in terms of the cavity control, and higher yield.

In addition, three major sensor probe assembly techniques are developed and investigated, including the epoxy bonding, inter-medium layer thermal bonding and CO_2 laser thermal bonding methods. The basic fabrication system and procedures are developed to allow the sensor to be fabricated in a controlled fashion. Sensors fabricated by the thermal fusion method, especially the CO_2 direct bonding method, show better performance in the aspects of temperature cross sensitivity, mechanical properties, and reliability.

The signal processing unit for the DOFIA sensor system is designed and improved. Due to the optimization on the light source, the circuit structure and the elements performance, the unit provides high gain ($>4x10^6$), wide and flat band response (flatness 2 dB in 20KHz - 300kHz), and ultra low noise (<30mV).

3. System noise analysis and performance optimization

To provide a better understanding of the performance limitations of the DOFIA sensor system, the detailed analysis of electronic and optical noises is presented. The noise analysis shows that the photodetector shot noise and the thermal noise of the feedback

resistor are two dominant noise sources in the electronic circuit. The measured noise agrees with the theoretical results very well.

On the optical noise side, based on the spontaneous emission theory of semiconductor laser diodes, the laser noise in an interferometric system is investigated. The discussion on the relative intensity noise (RIN) of light source points out that the SNR of a sensor system is limited by the laser noise, which provides the fundamental requirement for the laser source used in a sensor system. It is also shown that the phase-noise of the source is not a dominant factor in the interferometric sensor system.

More importantly, the impact of optical feedback into the light source on the sensor noise is simulated and discussed in this dissertation. The feedback coefficient is introduced to describe the characteristics of the laser system with external optical feedback. The theoretical results indicate that the optical feedback will cause mode-hoping and even 'coherence-collapse', which results in unstable laser output. Therefore, it is important to reduce the optical feedback as much as possible. Modeling on the feedback in the sensor system provides a theoretical guidance for improving the noise performance of a sensor system. Based on this analysis, an isolator and a SLED source are used in our sensor system, which significantly reduce the source noise.

The thermodynamic model of the diaphragm-based sensor in response to temperature variation is studied to reduce the temperature-cross sensitivity of the sensor head. The model reveals that the temperature effect can be brought down by decreasing the sensor size or reducing the CTE difference of the sensor materials. Experiment results show that the temperature coefficient of the sensors fabricated by the controlled thermal bonding technique is much smaller than that made by the Epoxy method. To further reduce the temperature coefficient, several methods have also been investigated. The open-air structure sensor has very low temperature coefficient $\beta \sim 1.6 \times 10^{-3} (\mu m/°C)$. Using the external dynamic compensation method, based on dynamic wavelength tuning, it is possible to totally eliminate the temperature effects in the sensor system.

4. DOFIA sensor system performance evaluation and application in PD detection

Comprehensive experiments are performed to systematically evaluate the performance of the DOFIA sensor system, including hydrostatic pressure test, capability for aerodynamic pressure test, hydro-dynamic pressure response, and performance in real partial discharge detection. The hydrostatic pressure test results show that the developed DOFIA sensor has small hysteresis. In the air shock-wave experiment, it is proven that the DOFIA sensor has similar SNR and response to the aerodynamic pressure with the conventional semiconductor pressure transducer, which indicates its great potential in different aerodynamic applications.

A calibration system has been set up to quantitatively test the sensor sensitivity and frequency response of DOFIA sensor in the hydro-environment. The sensor's pressure resolution can reach ~1.5×10^{-3} psi. Two types of band-width sensors, narrow and broad-band, are also demonstrated.

Using the developed DOFIA sensors, the attenuation properties of acoustic wave in the water is studied. The experiment results show that the acoustic wave attenuation coefficient is about 0.0626/cm, and the DOFIA sensor has ~30 degree detection range. For the first time, multiple fiber sensors have been successfully used to analyze the location of an acoustic source. The location resolution is less than 2mm. Those results show the possibility of applying the fiber sensors to locate a PD source in a power transformer.

A simple PD simulation system is set up in the laboratory. Our fiber acoustic system successfully received the acoustic waves generated by partial discharges in air, without any EMI noise. The results also show that the commercial PZT sensor cannot distinguish the real acoustic signal and EMI noise. This shows the optical sensor has unique advantage over the piezoelectrical–type sensor in the PD application.

Finally, the field test was performed in a power transformer by applying the DOFIA sensor to detect and locate partial discharges. The DOFIA sensor system successfully caught the acoustic signal generated by a partial discharge. The results indicate that the PD-induced acoustic emission is comprised of sinusoids with frequency ~120kHz and gradually decreasing amplitudes. These results clearly demonstrated the feasibility of the developed fiber sensor for the detection of partial discharges inside electrical power transformers. Compared with the conventional acoustic sensors, the DOFIA sensor has the advantages of non-electrically conducting, high frequency response, immunity to electro-magnetic interference (EMI), chemical inertness**,** and small size, and the capability of multiplexing more than one sensor in a single system.

References

[1] G.V. Frisk, Ocean and Seabed Acoustic -a Theory of Wave Propagation, PTR Prentice-Hall Prentice-Hall, Inc. 1994

[2] L.C. Lynnorth, Ultrasonic Measurements for Process Control, Boston: Academic Press, 1989

[3] A. Alippi, Acoustic Sensing and Probing, Word Scientific, 1992

[4] W.A Pledger, S.C. Pyke, "Gas Monitor Update: Review of Progress in the Development of an Automated Transformer Oil Monitor (ATOM)", 3rd EPRI Substation Equipment Diagnostics Conference, Nov 1-3, 1994, New Orleans, Louisiana.

[5] H. Xiao, J. Deng, W. Huo, M. Luo, Z. Wang, R. G. May, A. Wang, "Thin silica diaphragm-based SCIIB fiber optic acoustic sensors", *Proceedings of SPIE Vol. 3852, Harsh Environment Sensors II, [ES02-09], Sept. 1999*

[6] Jiangdong. Deng, Hai Xiao, Wei Huo, Ming Luo, Russell G. May, Anbo Wang and Yilu Liu, "Optical Fiber Sensor-based detection of Partial Discharges in Power Transformers ", *Optics and Laser Technology, Vol 33, no 5, pp. 305-311,July 2001*.

[7] Bing Yu, Dae Woong Kim, Jiangdong Deng, Hai Xiao, and Anbo Wang, 'Fiber Fabry-Perot sensors for dection of partial discharges in power transformers', *Applied Optics, Vol. 42, No.16, p3241-3250, June 2003.*

[8] C.-S. Lu, J. Vac. Sci. Technol., 12, 578 (1975)

[9] G.Z. Sauerbrey, Physics, 155,206(1959)

[10] J.A. Bucaro, H.D. Dardy, and E. Carome, "Fiber Optic Hydrophone", *Journal of Acoustic Society of America*. Vol. 62, 1977, pp. 1302.

[11] A. Dandridge, "Acoustic Sensor Development at NRL". *Acoustic Society of America Annual Meeting*, Miami, Florida, Nov. 1987.

[12] A. Dandridge and A.D. Kersey, "Overview of Mach-Zehnder Sensor Technology and Applications", *SPIE Proc. 985, Fiber Optic and Laser Sensor VI*, Boston, Sept. 1988.

[13] M. F. Gunther, A. Wang, B. R. Fogg, K. A. Murphy, and R. O. Claus, "Fiber optic impact detection and location system embedded in a composite material," *Proc. SPIE OE/FIBERS'92, Fiber Optic Smart Structures and Skins V,* Boston, Sept., 1992 (vol. 1798) pp262-269.

[14] J. A. Greene, T. A. Tran, V. Bhatia, M. F. Gunther, A. Wang, K. A. Wang, and R. O. Claus, "Optical fiber sensing technique for impact detection and location in composites and metal specimens," *J. of Smart Materials and Structures,* 4, 93-99 (1995).

[15] B. Jost et al., "Impulse response of a fiber optic probe hydrophone determined with shock waves in water", J. of Appl. Phys. Vol. 85, No. 5, p 2514 (1999)

[16] G. Zhou et al., 'Fiber-optic acoustic fourier transducer for audio sound processing', Applied Optics, Vol. 31, No. 11, 1741 (1992)

[17] J. R. Hull, 'Proposed frustrated-total-reflection acoustic method', Applied Optics, Vol. 20, No. 20, 3594, (1981)

[18] A. Arie, B. Lissak, M. Tur, "Static fiber-Bragg grating strain sensing using frequency-locked lasers", *Journal of Lightwave Technology, Vol. 17, no. 10, pp. 1849-1855. Oct. 1999.*

[19] P.M. Cavaleiro, F.M. Araujo, L.A. Ferreira, J.L. Santos, F. Farahi, "Simultaneous measurement of strain and temperature using Bragg gratings written in germanosilicate and boron-codoped germanosilicate fibers", *IEEE Photonics Technology Letters, Vol. 11, no. 12, pp. 1635 –1637, Dec. 1999.*

[20] D.J. Hill, G.A. Cranch, "Gain in hydrostatic pressure sensitivity of coated fiber Bragg grating", *Electronics Letters, vol. 35, no. 15, pp. 1268 –1269, July 1999.*

[21] M.G. Xu, H. Geiger, J.P. Dakin, "Fiber grating pressure sensor with enhanced sensitivity using a glass-bubble housing", *Electronics Letters, vol. 32, no. 2, pp. 128–129, Jan. 1996.*

[22] N. Takahashi et al., 'Underwater acoustic sensor using optical fiber Bragg grating as detection element', Jpn. J. Appl. Phys., Vol. 38, 3233(1999)

[23] H. E. Engan., 'Acoustic field sensing with optical fibers', acoustic sensing and probing, edited by A. Alippi, (World Scientific Inc. NY0, (1992)

[24] A. Dandridge, "Acoustic sensor development at NRL", *Acoustic Society of America Annual Meeting, Miami, Fl. U.S.A. Nov. 1987.*

[25] A. Dandridge and A. D. Kersey, "Overview of mach-Zehnder sensor technology and applications", *Proceedings of SPIE 985, Fiber Optic and Laser Sensors VI, Boston, Sept. 1988.*

[26] T. K. Lim, et al., ‘fiber optic acoustic hydrophone with double Mach-Zehnder interferometers for optical path length compensation’, optics communications, 159, 301(1999)

[27] S. Knudsen, et al., ‘An ultrasonic fiber optic hydrophone incorporating a push-pull transducer in a Sagnac Interferometer’, J. of lightwave Technology, Vol. 12, No. 8 1696(1994)

[28] B. J. Vakoc, et al., ‘A novel Fiber-opitc Sensor Array Based on the Sagnac Interferometer’, J. of Lightwave Technology, Vol. 17, No. 11, 2317 (1999)

[29] J. F. Dorighi et al, ‘Stabilization of an Embedded fiber Optic Fabry-Perot Sensor for Ultrasound Detection’, IEEE Trans. Ultrson. Ferroelectron., Freq. Contr., Vol. 42, No. 5, 820 (1995)

[30] J. J. Alcoz, et al., ‘ Embedded Fiber optic Fabry-Perot Ultrasonic sensors’, IEEE Trans. Ultrson. Ferroelectron., Freq. Contr., Vol. 37, No. 4, 302 (1990)

[31] C. E. Lee, et al., ‘ Metal-embedded fiber optic Fabry-Perot sensors’, Opt. Lett., vol. 16, no. 24., 1990 (1991)

[32] N. Furstenau et al., ‘Extrinsic Fabry-Perot Interferometer Fiber-Optic Microphone’, IEEE Trans. Intrum. Measurement, Vol. 47. No. 1 138(1998)

[33] P. Masson et al., ‘ Experiment on the use of fiber optic strain sensor in active structure acoustic control’, J. Intelligent Material System and structure, vol. 10, 71(1999)

[34] W. N. MacPherson, et al., ‘Miniature fiber optic pressure sensor for turbomachinery applications’, Review of Scientific Instruments, vol. 70, no. 3, 1868 (1999)

[35] V.I Kogan et al., ‘ Failure analysis of EHV transformers’ IEEE Transactions on Power Delivery, vol. 3, no. 2, 672(1988)

[36] J. W. Abbott, et al., ‘Development of an automated transformer oil monitor (ATOM)’ 3rd EPRI substation Equipment Diagnostics Conference, Nov. 1-3, 1994, New Orleans, Louisiana

[37] A. Zargari et al., ‘application of optical fiber sensor for partial discharge detection in High-Voltage power generators’, proceeding of the america power conference, vol. 59-II, Chicago, 1234(1997)

[38] P Grad, 'Acoustic Emission Betray insulation faults', J. the Institute of Engineers, Australia, vol. 58, no. 24, 26(1986)

[39] D. Zhu et al., 'the study of acoustic emission method for detection of partial discharge in power transformer',Proceeding of the 2nd international conference on properties and applications of dielectric materials, vol.2, 614(1988)

[40] L. E. Lundgaard, ' Partial discharge- Part XIV: Acoustic Partial Discharge Detection- Practical Application', IEEE Electrical Insulation Magazine, vol. 8, no. 4, 25 (1992)

[41] Z. Zhao, et al., 'the directionality of an Optical Fiber hight-frequency acoustic sensor for partial discharge detection and location', J. Lightwave Tech. Vol. 18, no. 6, 795 (2000)

[42] M. Born and E. Wolf, *Principles of Optics* (Pergamon, Elmsford, NY, 1975)

[43] Y.N. Ning, K.T.V. Grattan and A.W.Palmer, " Fiber-optic interferometric systems using low-coherence light sources", Sensor and Actuators A, 30, 180-192(1992).

[44] Calvin M. Miller, Stephen C. Mettler, Ian A. White, "Optical Fiber Splices and Connectors," (Marcel Dekker, Inc, New York and Basel, 1986), pp. 144-150.

[45] P. Hariharan, *optical Interferometry,* (Academic Press Australia, 1985)

[46] W. Soedel, *Vibrations of Shells and Plates,* Marcel Dekker, Inc, NY, 1993

[47] S. Temoshenko, *Vibration Problems in Engineering,* 4th Edition, (John Wiley & Son, N.Y, 1974)

[48] D. A. Jackson and J.D.C. Jones, *Optical Fiber Sensors: Systems amd Applications,* edited by B. Culshaw and J. Dakin (Artech House, Boston, 1988), Vol. 2

[49] Aicha Elshabini-Riad et al., *Thin Film Technology Handbook* (McGraw-Hill,1998)

[50] Stanley Wolf, *Silicon Processing for the VLSI Era* (Lattice Press, 1986).

[51] Anbo Wang, Jiangdong Deng, Yilu Liu, "Further Investigation of Partial Discharge Detection Using Fiber Optic SCIIB Acoustic Sensors", 2000 annual report to EPRI

[52] Anbo Wang, Jiangdong Deng, Yilu Liu, "Further Development and Field Demonstration of the SCIIB Fiber Sensors For Partial Discharge Detection", 2001 annual report to EPRI

[53] J. D. Deng, S. M Li, H. Xiao, W. Huo, P. G. Duncan, M. MCLauch, A. Wang, and W. Ng., " Miniature high-frequency temperature-insensitive fiber optic pressure sensor for gas turbine engine applications ", Proc. SPIE Vol. 3538, pp. 111-114, Jan, 1999.

[54] H. Xiao, P.G. Duncan, J. Deng, W. Huo, M. Luo, Z. Wang, R. G. May, A. Wang, Zh. Wang, and Y. Liu, " Thin silica diaphragm-based SCIIB fiber optic acoustic sensors ", Proceedings of SPIE Vol. 3852, pp. 36-45, Harsh Environment Sensors II, Dec. 1999.

[55] R. G. May, A. Wang, H. Xiao, J. Deng, W. Huo, and Z. Wang," SCIIB pressure sensors for oil extraction applications " (Invited Paper), Proceedings of SPIE Vol. 3852, pp. 29-35, Harsh Environment Sensors II, Dec. 1999.

[56] A. Wang, H. Xiao, R.G. May, J. Wang, J. Deng, P. Zhang, G. Pickrell, " Optical fiber sensors for harsh environments", Proceedings of SPIE, Vol. 4077, pp. 2-6, May, 2000.

[57] Hai Xiao, 'Self-Calibrated Intensity/Interferometric Based Fiber Optic Pressure Sensor', Ph.D dissertation, Electrical and Computer Engineering Department, Virginia Tech., 2000

[58] H. Xiao, J. Deng, W. Huo, M. Luo, Z. Wang, R. G. May, and A. Wang, " Fiber optic whitelight interferometric sensors for absolute measurements ", Proceedings of SPIE Vol. 3852, pp. 74-80, Harsh Environment Sensors II, Sept. 1999.

[59] Hai Xiao, Jiangdong Deng, Gary R. Pickrell, Russell G. May, and Anbo Wang, " Single crystal sapphire fiber-based strain sensor for high temperature applications ", Journal of Lightwave Technologies, Vol. 21, No. 10, pp. 2276-2283, Oct. 2003

[60] Jiangdong. Deng, Hai Xiao, Wei Huo, Ming Luo, Russell G. May, Anbo Wang and Yilu Liu, " Optical Fiber Sensor-based detection of Partial Discharges in Power Transformers ", *Optics and Laser Technology, Vol 33, no 5, pp. 305-311,July 2001*.

[61] J.G. Graeme, Photodiode Amplifiers, (McGraw-Hill,1996)

[62] E.L. Dereniak, Infrared Detectors and Systems, Wiley, New York, 1996

[63] G. P. Agrawal, *Fiber-Optic Communication System*, (John Wiley & Sons, Inc.) 1997

[64] M. Sargent, M.O.Scully, and W.E. Lamb, *Laser Physics*, Addison-Wesley, 1974

[65] G.P. Agrawal and N.K.Dutta, *Semiconductor Lasers*, 2nd ed., Van Nostrand Reinhold, New York, 1993

[66] M. W. Fleming et al., ‘ Fundamental line broadening of single-mode (GaAl)As diode lasers’, Appl. Phys. Lett., Vol. 38,pp.511-513, 1981

[67] B. Daino et al., ‘Phase noise and spectral line shape in semiconductor lasers’, IEEE J. Quant. Electron., Vol. QE-19, pp. 266-270, 1983

[68] K. Petermann and E. Weidel, ‘Semiconductor laser noise in an interferometer system’; IEEE J. Quant. Electron., Vol. 17, pp327-329, 1981

[69] B.Moslehi, ‘Analysis of optical phase noise in fiber-optic systems employing a laser source with arbitrary coherence time’, J. lightwave Techn., Vol. LT-4,pp.1334-1351, 1986.

[70] P. Spano, S.Piazolla ‘Theory of noise in semiconductor lasers in the presence of optical feedback’ IEEE J. Quant. Electron., Vol. QE-20, pp.350-357,1984

[71] R.W. Tkach and A. R. Chraplyvy, ‘ Regimes of feedback effects in 1.5 um distributed feedback lasers’, J. Lightwave Techn., Vol. LT-4,pp.1655-1661, 1986

[72] I. Ikushima and M. Maeda, ‘Laser spectra od semiconductor lasers coupled to an optical fiber’, IEEE J. Quant. Electron., Vol. QE-15,pp.844-845, 1979

[73] D. Lenstra, et al., ‘Coherence collapse in single-mode semiconductor lasers due to optical feedback’, IEEE J. Quant Electron., Vol. QE-21,pp674-679, 1985

[74] Bing Yu, Jiangdong Deng, et al., " Fiber Fabry-Perot Sensors for Detection of Partial Discharges in Power Transformers ", *Applied Optics-OT, Vol. 42 Issue 16, pp. 3241-3250, Jun, 2003.*

[75] L.E. Kiensler, et al., Fundamentals of Acoustic. John Wiley & Sons, New York, 1982

[76] V.A. Shutiliov, et al., Fundamental physics of Ultrasound. Gordon and Breach Science Publishers, New York, 1988.

VITA

Jiangdong Deng was born in China, 1969. He received the B.S., M.S. and Ph.D degrees in condensed matter physic from Nankai University, China, in 1991, 1994 and 1997, respectively.

From 1997 to 2001, he joined in the Center for Photonics Technologies (CPT), Virginia Polytechnic Institute and State University (Virginia Tech), Blacksburg, as a Sesior Research Assistant. At the same time, he pursued his second Ph.D. degree in electrical engineering. From 2001 to 2004, he worked in NanoOpto Corporation, Somerset, NJ, as a Senior Engineer. He is currently a Principal Technologist in the Center for Imaging and Mesoscale Structure (CIMS) of Harvard University. His research interests includes nano-physics, nanostructure-based devices, nanofrabrication technologies, optical fiber sensors, optical fiber communication devices, nondestructive optical detection for microdefects, and crystal growth.